AN ABSTRACT OF THE THESIS OF

Koonlaya Kanokjaruvijit for the degree of Master of Science in Mechanical Engineering presented on February 16, 2000. Title: Effects of Orifice Geometry and Surface Boundary Condition on Heat Transfer of Impinging Jet Array

Abstract approved: Redacted for privacy

James A. Liburdy

The effects of the orifice geometry and the surface boundary condition on the heat transfer distribution to a flat surface of an impinging jet array were investigated. The jet array impinged normally onto the surface which was either isothermal or had a uniform heat flux. The experiments were performed for the flow rate range from 0.0039 to 0.0070 m^3/s corresponding to jet Reynolds numbers of 5000 to 11000. The jet-to-surface spacings varied from 1 to 4 jet diameters. After impinging, the air jet was constrained to exit in one direction creating a "crossflow" condition. The isothermal surface results are presented in terms of the average heat transfer coefficient. For the uniform heat flux surface, both average and local values are presented. The average and local heat transfer distributions were mapped using thermochromic liquid crystals. Results are presented for two jet geometries: circular and cusped ellipse. The cusped ellipse jets show better heat transfer performance compared to the circular jets for both surface boundary conditions. This is thought to be a result of increased turbulence and the axis-switching phenomenon. Results for the uniform heat flux surface boundary

higher than for the isothermal surface boundary condition. This result can be explained by the difference between the surface temperature and the jet temperature for both surface boundary conditions. Correlations of Nusselt versus Reynolds numbers are presented for both jet geometries and surface boundary conditions.

Effects of Orifice Geometry and Surface Boundary Condition on Heat Transfer of Impinging Jet Array

by

Koonlaya Kanokjaruvijit

A THESIS

submitted to

Oregon State University

in partial fulfillment of

the requirement for the

degree of

Master of Science

Presented February 16, 2000

Commencement June 2000

Master of Science thesis of Koonlaya Kanokjaruvijit presented on

February 16, 2000

APPROVED:

Redacted for privacy

Major Professor, representing Mechanical Engineering

Redacted for privacy

Head of Department of Mechanical Engineering

Redacted for privacy

Dean of Graduate School

I understand that my thesis will become part of the permanent collection of Oregon State University libraries. My signature below authorizes release of my thesis to any reader upon request.

Redacted for privacy

Koonlaya Kanokjaruvijit, Author

ACKNOWLEDGEMENT

The master's degree thesis taught me not only to bring the knowledge I have learned from classes to use, but also a superb pilot scale of the working process in the outside world. There are some people I would like to thank.

First of all, I would like to thank Dr. Liburdy for knowledge I have learned from his class, and his direction on my thesis.

I would like to thank my parents, Saikaew and Sunantha Kanokjaruvijit, my sister and my brother-in-law, Karuna and Kitchai Pitiwiwat, and my brother, Karoon Kanokjaruvijit, for supporting me in every way of life, and their love.

The experiment for this thesis would not be finished without Bertrand Dano, who has been my colleague, classmate, and friend. I would like to thank him, and wish him the best on his thesis and future study.

The experimental setup would not have been done without Steve Adams, my OSU dad. I would like to thank him for all of his supports.

For emotional support, I would like to thank all of my friends.

TABLE OF CONTENTS

TABLE OF CONTENTS (Continued)

Page

LIST OF FIGURES

LIST OF FIGURES (Continued)

LIST OF FIGURES (Continued)

LIST OF APPENDIX TABLES

LIST OF APPENDIX TABLES (Continued)

NOMENCLATURE

A_j	Jet exit area, m^2
A_s	Heating surface area, m^2
D_h	Hydraulic orifice diameter, m
H	Height of jet array above surface, m
$\bar{h}$	Heat transfer coefficient, W/m^2K
h	Local heat transfer coefficient, W/m^2K
I	Heater input current, Ampere
k_{plex}	Thermal conductivity of plexiglas, W/m-K
k_{air}	Thermal conductivity of air, W/m-K
$\dot{m}$	Mass flow rate, kg/s
N_j	Number of jets
Nu	Local Nusselt number based on hydraulic diameter, hD_h/k_{air}
$\overline{Nu}$	Average Nusselt number based on hydraulic diameter,
P_p	Pressure in Plenum Chamber
Pr	Prandtl number
q"	Heat flux from the heater, W/m^2
q	Total power input, W
$\dot{Q}$	Volume Flow Rate, m^3/s
R	Resistance, Ω
Re	Reynolds number, $\dot{m} D_h/A_j\mu$

S	Spacing from jet center to center, m
T_{gt}	Temperature read from glass thermometer, °C
T_j	Jet air temperature, °C
T_s	Surface temperature, °C
T_{DL}	Temperature read from data logger, °C
T_{TC}	Temperature read from thermocouple, °C
V	Heater Input Voltage, Volts
Z_n	Height of jet array above impingement surface, m
μ	Viscosity,
ρ	Density, kg/m^2

Effects of Orifice Geometry and Surface Boundary Condition on Heat Transfer of Impinging Jet Array

CHAPTER I

INTRODUCTION

Jet impingement cooling has been used extensively to cool high heat flux surfaces. One such example is gas turbine. Gas turbines are used worldwide to extract energy from a flowing gas. The high temperature and high speed flow from nozzles provide the necessary energy to strike the rotating blades. The higher turbine inlet temperatures provide a higher energy content per pound of gas. The turbine blades, therefore, are one of the important hot components of gas turbines.

The heat transfer from the hot gas environment to the outer-surface of the blades, and from the inner-surface of the blades to the coolant, which is usually air, is not uniform. This can reduce the strength of the material of the blades, and cause thermal stress. An effective cooling scheme is, therefore, very significant in designing gas turbines. The effective cooling scheme also increases the level of the tolerable turbine inlet temperature, and improves the performance and durability of the gas turbines.

The purpose of cooling is to lower both overall component temperature levels and local temperature gradients. Metzger (1) showed the service life dependencies of gas turbines seen in Figure 1.1. He also noted that the reduction in fuel consumption per unit thrust as the turbine inlet temperature was increased

when the coolant performance was improved as shown in Figure 1.2. He stated that an optimization procedure could specify the arrangement of coolant passage elements such as multiple jet array orifice, pins, and ribs, if the information of local heat transfer and pressure loss were sufficiently available.

One method of cooling turbine blades is to use jet impingement with air extracted from the compressor as the coolant. The greatest advantage for this method is the provision of high cooling rate at the required locations. However, the plausible disadvantage is that overcooling may cause locally large temperature gradients, which can also produce high stress.

There are many studies on jet impingement heat transfer to provide information such as the jet size, jet geometry, jet spacing, and impingement distance between the jets and the surface to be cooled, including the heat transfer coefficients and the correlations with those parameters. These studies have been aimed at gas turbine applications, but also apply to high heat flux electronic cooling. The literature review will provide some studies on jet impingement and techniques of various researchers.

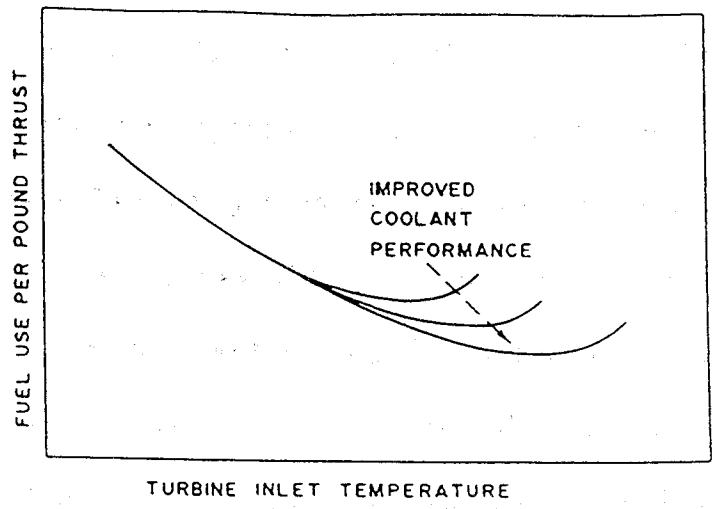

Figure 1.1. Service Life Dependencies, from Metzger (1)

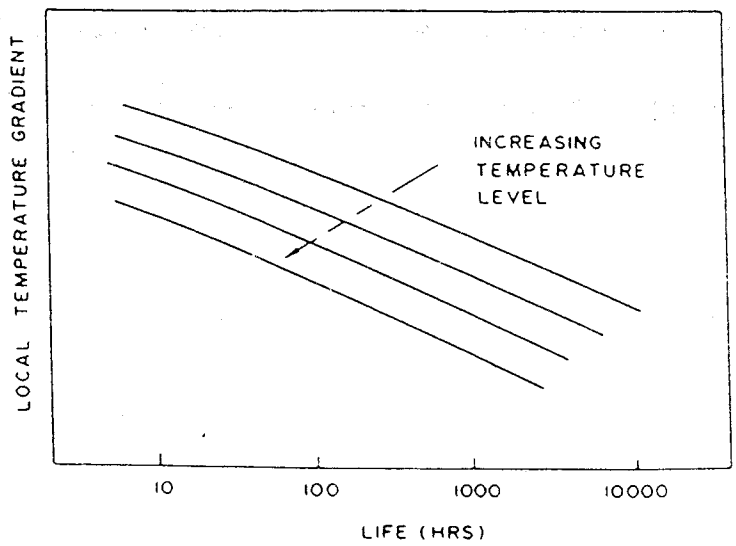

Figure 1.2. Effect of Turbine Inlet Temperature, from Metzger (1)

The present study is to obtain detailed information on jet array impingement. It is divided into two parts related to the surface boundary conditions: an isothermal impingement surface and a uniform heat flux impingement surface. Two configurations of the jet arrays are used: a circular jet array and a cusped ellipse jet array. The objective for the isothermal impingement surface is to measure and correlate the average heat transfer distribution. Then, the results from both geometries are compared. For the uniform heat flux impingement surface, the local distribution of the heat transfer coefficient for both jet geometries were obtained using a liquid crystal technique, and compared. Then, the average heat transfer coefficients and the average Nusselt numbers were calculated, correlated, and compared for both jet geometries. Finally, the average heat transfer distribution from the isothermal jet impingement surface and that from the uniform heat flux jet impingement surface are compared. In this study, the varied parameters are the height between the jet array and the impinging surface, and the flow rate of the air.

CHAPTER II

LITERATURE REVIEW

The literature review covers three main topics. The first area is isothermal surface heat transfer by jet impingement with crossflow. The second area deals with uniform heat flux surface by jet impingement. The last area is about liquid crystals and the methods of using them.

Isothermal Jet Impingement Surface

Behbahani et al. (2) investigated the average heat transfer coefficients with the effect of spent air using a square array of impinging jets on an isothermal heated surface. The air was forced to leave from only one side. The three other sides were closed by walls. Two perforated plates with the jet diameters of 5 and 10 mm were used. The jet-to-jet spacings of 4 and 8 diameters were used with each jet-to-plate spacings of 2, 3, 4 and 5 diameters for jet Reynolds number of 5000, 10000 and 15000. The maximum heat transfer coefficient has found at jet-to-plate spacing of 4. However, the heat transfer changed very little between jet-to-plate spacings of 2 and 4. For the small jet diameter, the higher heat transfer coefficients were obtained with the higher jet velocities. Finally, they found the correlation of Nusselt number with Reynolds number and the ratio of the center-to-center jet spacing, S, and diameter, D, as:

$$Nu_{ave} = a\,\mathrm{Re}_j^{0.78}(S/D)^{-n}$$

where n depends on the jet-to-plate spacing, and a is an experimental constant.

Kercher and Tabakoff (3) investigated the average heat transfer coefficients under a perforated plate of square array, circular impinging air jets. The experiments covered a range of Reynolds number from 300 to 30000, jet spaces from 3.1 to 12.5 jet diameter, and plate-to-surface distances of 1.0 to 4.8 jet diameters, with and without crossflow. They observed that heat transfer coefficients increased with increasing open-air area, which is the ratio of total jet area to heat transfer area. The heat transfer was dominated by the hole-diameter Reynolds number and jet-to-surface ratio. The correlation, therefore, was developed in the form

$$Nu_{D,x} = \Phi_1 \Phi_2 \, \mathrm{Re}_D^m (Z_n / D)^{-0.091} \, \mathrm{Pr}^{1/3}$$

where Φ_1 and m are functions of the jet-spacing parameter and Reynolds number,

Φ_2 is the heat transfer coefficient degradation factor due to "spent air", and

Z_n is the distance between the impingement plate and heat transfer surface

Within the range tested, increasing Z_n/D increased the heat transfer without crossflow, but decreased heat transfer with crossflow. They also found that when the crossflow relative to jet velocity was increased, the heat performance was decreased. Furthermore, decreasing hole diameter with increasing number of holes, everything else being equal, improved heat transfer performance.

Hrycak (4) investigated heat transfer from round jets, impinging perpendicularly to 3 different flat plates. Two were made of 304 SS and supported by a brass base plate. One was equipped with 14 304 SS embedded 5.08-mm diameter calorimeters. The other one consisted of 6-concentric segments separated

from each other by a 1.6-mm gap. The gap was sealed on top with a layer of silicone rubber. The third plate was made of Invar and was otherwise geometrically identical with the second plate. Two types of nozzles were used: a straight-bore tube nozzle and a tube-type nozzle with an inner lip at the exit, which provided a flat velocity profile. The author varied nozzle-to-target plate distance, with Reynolds numbers ranging from 14,000 to 67,000, and nozzle diameters from 3.18 to 12.7 mm. The data at the stagnation point was correlated with the average heat transfer using dimensional analysis. He found that at the stagnation point, the Nusselt number had a tendency to peak at about 7 diameters away from the target plate for the tube-type nozzles. At the stagnation point, the Nusselt number depended on the Reynolds number to the one half power indicating laminar boundary-layer flow. The author found the correlations on the results of the stagnation point as:

$$Nu_0 = 1.41\,\mathrm{Re}_D^{1/2}\,\mathrm{Pr}^{0.4}(Z_n/D)^{0.16}(D/D_c)^{0.28} \quad \text{for } Z_n/D < 7$$

and

$$Nu_0 = 3.92\,\mathrm{Re}_D^{1/2}\,\mathrm{Pr}^{0.4}(Z_n/D)^{-0.4}(D/D_c)^{0.39} \quad \text{for } Z_n/D > 7$$

where Nu_0 is the Nusselt number at the stagnation point

Re_D is the Reynolds number with nozzle diameter as significant length

Pr is the Prandtl number

D is nozzle diameter (tube type)

Z_n is the distance from nozzle to the target plate

D_c is the calorimeter diameter

Hamahah (5) investigated the effect of spacing conditions on the heat transfer from the impinging surface using a square array of round air jets. The experiment was carried out for constant surface temperature. The jet diameter and the plate thickness were equal to 1/10 inch. The jet-to-jet spacing was varied between 2 and 8 jet diameters. The distance between the orifice plate and the heated copper block was also varied from 1 to 24 jet diameters. The Reynolds number was varied between 140 and 4700. The average heat transfer coefficient was calculated. It was found that there were heat losses of 0.7% by conduction and 14% by radiation. The maximum heat transfer coefficient occurred between a jet spacing of 2 and 4 jet diameters when jet spacing was varied between 3 and 8 jet diameters, with a constant Reynolds number. The author obtained a correlation for the average Nusselt number as:

$$Nu_{ave} = 0.143(S/D)^{-0.698}(Z/D)^{-0.132}\,\mathrm{Re}^{0.734}$$

where D is a jet diameter

S is a center-to-center spacing between jets

Z is a distance between a jet plate and impingement surface

The correlation is valid for $2 \le Z/D \le 8$, $3 \le S/D \le 8$, and $300 \le \mathrm{Re} \le 4700$.

Florschnetz and Su (6) considered two-dimensional arrays of circular jets impinging on an isothermal heated surface parallel to the jet orifice plate. They varied the initial crossflow temperature, and found that the mixed-mean cross flow temperature for each spanwise jet row n ($T_{m,n}$) varied independently of the jet temperature (T_j), which was held constant. However, there was an effect of $T_{m,n}$

relative to T_j on the heat flux for each row. The results were formulated in terms of a crossflow-to-jet temperature difference influence factor (η_r) reflecting the strength of the influence on the heat flux when $T_{m,n}$ differs from T_j and Nusselt number (Nu), which are functions of jet Reynolds number, crossflow-to-jet mass flux ratio, and geometric parameters. They also considered the effect of row position. They found that η_r and Nu_r are nominally independent of row position after the first two rows.

Obot and Trabold (7) studied the effects of three jet-induced crossflow schemes. Those schemes were the minimum, intermediate, and maximum crossflows. The minimum crossflow scheme was the unrestricted flow of the spent air away from the target surface. The intermediate crossflow was the restriction of the flow to leave through two opposite sides. The maximum crossflow was defined for the flow through one side of a rectangular impingement surface. The experiment for each scheme was done over the Reynolds number range of 1000 to 21000, the jet-to-plate spacings of 2 through 16, jet arrays with 48, 90 and 180 jets, and orifice plate of thickness-to-diameter ratio of 3.02. Air at room temperature from the blower was used as the working fluid. The impingement surface comprised of the plexiglas plate assembled with the aluminum heat transfer surface. This aluminum heat transfer surface was formed by cementing together six aluminum plates. Six thermocouples were installed in each segment in order to determine the average surface temperature.

They found that for the local mean Nusselt number, the segment furthest from the exhaust in the maximum crossflow scheme was not significantly affected by the crossflow originated from that region. They expected the intermediate crossflow scheme would give the symmetric flow, and found that the Nusselt number values were higher over the central part of the impingement surface than near the two exhausting openings. They found that the minimum crossflow scheme gave the highest Nusselt number. The average Nusselt number increased with the increasing number of the jet holes. At large Reynolds number with the maximum number of jet holes, the high turbulence levels at the nozzle exit and at downstream locations combining with the jet interference prior to the impingement, which is the interference in all directions with the neighboring jets, brought about a maximum in heat transfer.

Metzger et al. (8) investigated the flow of the two-dimensional array of the circular jets of air impinging on a heating surface, and the crossflow. They used the maximum crossflow scheme. The region between the jet plate and the heating surface was enclosed on three sides. This constrained the exhaust air from the jets to exit in a direction along the channel. The experiment was held over the Reynolds number between 2500 and 70000, the ratio of the channel crossflow mass velocity based on the channel cross-sectional area and the jet mass velocity based on jet hole area 0 to 0.8. The streamwise jet hole spacing of 4 to 8 jet diameters was used for the inline pattern, and that of 5 to 10 was used for the staggered pattern. The spanwise jet hole spacing of 4 to 8 jet diameters was employed. The jet-to-plate

spacing was varied from 1 to 3. They found that for the large hole spacings and small channel heights, the crossflow provided an increased heat transfer distribution, and did not cause a large degradation in heat transfer distribution. For the smaller hole spacings, and larger channel heights, the jets were diffused more by the crossflow, and the cooling effectiveness was reduced. They explained the reason for this was that the crossflow became channelized between adjacent streamwise jet rows, and caused the spanwise jet distribution to be nonuniform. Another reason was from the results of the potential core length. Finally, they found the correlation as follows

$$Nu = A\,\mathrm{Re}_j^m\{1 - B[(z/D)(G_c/G_j)]^n\}\,\mathrm{Pr}^{1/3}$$

where $A, m, B, n = C(x_n/D)^{n_x}(y_n/D)^{n_y}(z/D)^{n_z}$

C, n_x, n_y, n_z are constants

x_n is streamwise jet hole spacing

y_n is spanwise jet hole spacing

z is channel height

G_c is crossflow mass velocity based on channel cross-sectional area

G_j is jet mass velocity based on jet hole area

Uniform Heat Flux Jet Impingement Surface

Baughn and Shimizu (9) studied a single circular turbulent air jet at ambient air temperature impinging on a flat stationary surface. They provided experimental results for a fully developed jet impingement on a uniform heat flux surface. A blower was used to originate the development of the flow in a long pipe. The upstream development provided nearly fully developed flow at the exit. For the test section, the uniform heat flux surface was made by electrically heating a very thin gold coating on a plastic surface. The surface temperature distribution was measured using 1°C-ranged liquid crystal. An isotherm on the surface represented a contour of a constant heat transfer coefficient and was a line of a particular color. They reported in the data reduction that the radiation was less than 5% and the heat conduction losses was less than 1%, due to the low thermal conductivity of plastic substrate. They observed that the color band was very close to a perfect circle due to the symmetry of the round jet. The maximum heat transfer was found at the stagnation point.

San et al. (10) investigated the local Nusselt number of a confined circular air jet vertically impinging on a flat plate, and the effect of recirculation and mixing. In the experiment, the jet exited in two opposite directions. A part of the impingement surface was maintained at a constant heat flux condition, and the rest was adiabatic. For the constant heat flux surface, DC electric power was conducted through a very thin stainless foil with uniform heat generation rates of 500, 1000, 1500 and 2000 W/m^2. Four diameters of confined jet holes were used: 3, 4, 6 and 9

mm. Reynolds number ranged from 30,000 to 67,000, and the ratio of the distance from jet exit to impingement surface over the jet hole diameter was held constant at 2. They found that the jet diameter affected the Nusselt number. The smaller the diameter, the lower Nusselt number, but for the diameter greater than 6 mm, the influence of the jet hole diameter on the Nusselt number tended to decrease. For the higher Reynolds number, the recirculation and mixing was stronger. They explained that since the downstream heated air recirculated upstream, the fluid temperature near the impinging plate was higher. Therefore, the jet cooling effect was degraded, and the Nusselt number decreased. The surface heating width was also found as an important factor, which dominated the Nusselt number. For a specific jet hole diameter, the greater the surface heating width, the lower the Nusselt number due to the recirculation and mixing effect. However, when the surface heating width was 40 times the jet hole diameter, the Nusselt number at the stagnation point tended to be independent of the surface heating width.

El-Genk et al. (11) investigated a single circular jet impinging on a constant heat flux plate. The constant heat flux surface was made of 312A SS with the thickness of 0.0508 mm placed on a 2.54-cm thick piece of Bakelite. The power for the constant heat flux surface was from a DC power supply with high current, and low voltage. In this experiment, the heat loss due to conduction was calculated to be less than 2%. The jet-to-plate spacing was an independent variable, which was ranged from 1 to 12 diameters. Reynolds numbers ranged from 6,000 to 60,000.

They found that the maximum stagnation Nusselt number was obtained at 1.8 to 2 jet diameters from the jet center.

Lee et al. (12) investigated local heat transfer distribution for a turbulent submerged air jet from an elliptical jet impinging on a constant heat flux flat surface using thermochromic liquid crystals. Reynolds numbers of 5000, 10000, and 20000 were used. The dimensionless jet-to-plate distances, H/D_e were 2, 4, 6, and 10. The thermochromic liquid crystals were used as sensors to measure temperature changes. They found that the isothermal contour on the uniformly heated surface changed in shape from elliptic to near circle to elliptic again with an increasing jet-to-plate distance as the elliptical cross-section switched its orientation. For $H/D_e = 2$ at Re = 10,000 and 20,000, they reported that there were three maximum in Nusselt number. The first one was at the stagnation point. The second and the third ones resulted from toroidal vortices on the impingement surface between the stagnation region and the wall jet region. However, at the same Reynolds numbers for other jet-to-plate distances, decreasing values of Nusselt number were monotonic.

For Re = 5000 and 10000, the heat transfer coefficient at $H/D_e = 6$ was smaller than that at $H/D_e = 2$ and 4. They compared this result to that of Baughn and Shimizu (9), who found that for the round jet at the same Reynolds number, the maximum heat transfer coefficient was found maximum at $H/D_e = 6$. They explained that this was due to the fact that the elliptical jet had a shorter potential core length and higher spreading rate than the round jet. Furthermore, the Nusselt

number distribution for an elliptical jet was compared with that for a round jet studied by Goldstein and Franchett (13) at $H/D_e = 10$ for Re = 20,000. They found that the heat transfer coefficients for an elliptical jet at the stagnation point was 10% higher. It was explained that the self-induction of large-scale asymmetric coherent structures of the elliptical jet caused azimuthal distortion of the elliptical vortex ring, and therefore, there was the large entrainment of the surrounding fluid into jet.

Schroeder et al. (14) investigated the local heat transfer distribution from a foil discrete heat source, which produced a constant heat flux, to multiple, perpendicular impinging, confined air jets. Reynolds number ranged from 5,000 to 20,000 and the jet-to-plate spacings (H/D_h) ranged from 0.5 to 4. A 20x20 mm-stainless steel foil heater was used. The results from 4x4 and 9x9 jet arrays were investigated, and compared to the results of a single jet. The local heat transfer coefficient was found from the following:

$$h_{local} = q''/(T_s-T_j)$$

where T_s is the local surface temperature, which depends on the location of heat source. They found that the local heat transfer distribution depended on the jet-to-plate spacing, Reynolds number, and the interjet spacing. For the 9x9 array, the peaks of the local heat transfer coefficients were found near the centers of the impinging jets, and the average heat transfer coefficient was nearly twice that of a single jet. For the 4x4 array, the minimum of the local heat transfer coefficients was found at the center of the heater due to the absence of the central jet. The heat

transfer coefficient, however, increased near stagnation points. The average heat transfer coefficient for this array was 20% higher than the result of the single jet. Nevertheless, for the 4x4 jet array, when Reynolds number was higher, a decrease in H/D_h caused a shift in the maxima in the local heat transfer coefficients towards the center of the heater and flattening of the distributions in the stagnation regions. It was found in both cases that when H/D_h was decreased, the heat transfer coefficient was increased, and this effect was stronger at higher Reynolds number. At fixed H/D_h, as Reynolds number was increased, the local heat transfer coefficient was increased. Also, the array heat transfer increased faster with increasing Reynolds number than that in the case of the single jet at smaller H/D_h. For both arrays, the correlation was found as

$$\overline{Nu} = 0.127\,\mathrm{Re}^{0.693}\,\mathrm{Pr}^{0.4}(H/D_h)^{-0.105}$$

which is valid for $5000 \le \mathrm{Re} \le 20000$, $0.5 \le H/D_h \le 4$, and the ratio of the orifice plate thickness to the hole diameter is unity.

Huber and Viskanta (15) studied the effects of the jet-jet spacing, nozzle-plate spacing, and spent air exits located between the jet orifices, on the magnitude and uniformity of the heat transfer coefficient distribution. The 3x3 square arrays of axisymmetric orifices were used in the experiment. The Reynolds number ranged from 3500 to 20400. The very thin stainless steel foil was used to generate the uniform heat flux. Liquid crystal was used as the temperature measurement to provide information on the local heat transfer coefficient distribution over an impingement surface. The experiment was done at the nozzle-plate spacing of 0.25,

1.0 and 6.0, and the jet-jet spacings of 4, 6 and 8. All were done with and without spent air exits.

They found that the maximum Nusselt number did not occur at the stagnation point, but at the secondary rings around the stagnation point. These secondary rings increased the average heat transfer coefficient. As Reynolds number was decreased, and the nozzle-plate distance was increased, they observed that the inner secondary peak was decreased. However, the outer secondary peak caused by the transition to turbulent flow was more pronounced. The jet-jet spacing of 4 gave the highest average Nusselt number for any nozzle-plate spacing, and the most uniform distribution due to the large fraction of impingement surface, which was covered by the stagnation region. However, on a mass flux basis, the jet-jet spacing of 8 gave a more uniform Nusselt number distribution, since a unit mass of fluid had more contact with the surface to remove heat.

Spent air exits were placed between the jet orifices in the jet orifice plate in order to minimized the adjacent jet interference and the crossflow degradation of the heat transfer coefficient. With spent air exits, the heat transfer was enhanced, and each jet in the array had the same jet-jet spacing and similar performance. They investigated that at the jet-jet spacing of 4, the effect of spent air exits on the Nusselt number distribution was the highest because the fluid had less impingement surface area before contacting the adjacent jets to spread out and slow down than other arrays with higher jet-jet spacings.

For the higher nozzle-plate spacing, the difference between the Nusselt number distributions with and without spent air exits was unremarkable, but the difference was significant when the gap was narrower. They explained that the larger gap between the impingement surface and the jet orifice plate channeled the flow outward without a significant pressure drop. But, the narrower gap caused resistance to the flow with no spent air exits, hence the fluid exited radially outward and boundary layer transition was generated, which delayed the outer secondary peak. They reported that the spent air exits were important especially to a small nozzle-plate distance. The spent air exits minimized the crossflow heat transfer coefficient degradation, and improved the uniformity of the heat transfer coefficient across the array as each individual jet had nearly identical flow conditions and Nusselt distribution.

The average Nusselt number correlation for their results was found to be

$$\overline{Nu} = 0.285\,\mathrm{Re}^{0.710}\,\mathrm{Pr}^{0.33}(H/D)^{-0.123}(X_n/D)^{-0.725}$$

where $\overline{Nu}$ is the average Nusselt number

Re is the Reynolds number

Pr is the Prandtl number

H is the distance between the orifice plate and the impingement surface

X_n is the distance between jets in a square array

D is the jet diameter

Application of Liquid Crystals

Friedrich Reinitzer discovered liquid crystals. The name, liquid crystal, arose from the property that it has in common with liquid and crystal; its molecules have no specific arrangement and can be moved by the external forces like a liquid, and have three dimensional arrangement as do crystals. In other words, liquid crystals have viscosity ranging from glue to that of glass, and also have optical properties like crystals.

Fergason (16) divided liquid crystals into three categories: smectic, nematic, and cholesteric. Molecules of a smectic liquid crystal are cylindrical lining up parallel to each other to form layers of molecules. Molecules of a nematic liquid crystal are also cylindrical, but less ordered than that of smectic liquid crystal. The molecules line up parallel to each other, but do not form layers. A cholesteric liquid crystal has properties similar to both smectic and nematic liquid crystal. It forms layers like smectic, but each layer is like the nematic liquid crystal. He found that these liquid crystals could be applied to display color changes at various temperatures.

Parsley (17) employed the thermochromic liquid crystals in the research of heat transfer and flow visualization because of the properties of indicating temperature fields and thermal mapping of them. The thermochromic liquid crytals can be categorized into two groups: cholesteric and chiral nematic. The formulations of the cholesteric liquid crystal comprise of cholesterol and other

sterol-related chemicals, while those of the chiral nematic liquid crystals comprise of non-sterol based chemicals.

However, from the product and application information of Hallcrest, Inc. (18), there is a third group, which is the combination of the above two groups. The combination shows a continuum of physical and chemical properties between pure cholesteric and pure chiral nematic liquid crystals. They combined the advantages of both groups, which gives desired color changes within specified temperature ranged by showing colors by selectively reflecting incident white light. These colors go from colorless to red, orange, yellow, green, blue, violet, and back to colorless again when heated. The change sequence is reversed when cooling.

The Hallcrest, Inc. divide the thermochromic liquid crystals into three exploitable forms: unsealed liquids, micro encapsulated form, and coated or printed sheets. The unsealed liquids have two forms: neat liquid crystal mixture, and solutions. These forms are difficult to use because they need to be thin, uniform films and are sensitive to fats, grease, and organic solvents. Furthermore, dust and fiber particles can be easily trapped. The microcapsulated form is the most versatile. It has two forms: aqueous slurries, and coating formulations. It is a small sphere comprised of a tiny drop of liquid crystal surrounded with a continuous polymer coating to give discrete microcapsules. The diameter is very small ranging from a few microns to a few millimeters. It is isolated from the atmosphere to prevent the deleterious effects and UV light, solvents and other impurities by protective barriers. The last form is coated or printed sheet. A thin film of liquid

crystal is sandwiched between a transparent polymer substrate, and back absorbing background. The use of different forms of materials depends upon different temperature ranges and flow visualization.

Hippensteele et al. (19) evaluated a method for heat transfer measurements and thermal visualization using a composite of a heater element and liquid crystal. The cholesteric liquid crystal sheet was selected for use in the experiment. Two kinds of heaters were used, vapor-deposited gold and a carbon-coated sheet. The liquid crystal sheet was calibrated for color versus temperature by immersing the sheet in hot water and then observing its color using a camera.

They found that the composite of liquid crystal painted on a heater element provided an accurate device for the high-resolution measurement of heat transfer and for determining local heat transfer coefficient at or near room temperature. The heating uniformity of the composite of a heater and a liquid crystal sheet was determined by using an energy balance for the surface-convection heat transfer.

$$q_e - q_l = hA(T_c - T_a)$$

where q_e = heat flux from the electric power input

q_l = heat loss due to conduction and radiation

T_c = temperature of liquid crystal at calibrated color

T_a = air temperature

The same investigators (20) demonstrated the method of using a liquid crystal/heater composite sheet for heat transfer research, and verified the accuracy and resolution of the resulting heat transfer coefficient. The composite of

cholesteric liquid crystal and carbon-impregnated paper, which produced the uniform heat flux, were wrapped around an airfoil of a test turbine blade. The turbine blade surface was heated, and the free stream was at room temperature. The local heat transfer coefficients were presented for Reynolds number from 2.8×10^5 to 7.6×10^5, and compared well with the numerical values obtained from STAN5 boundary layer code program. They found that the yellow color occurred over the narrowest temperature band. Therefore, the yellow color was used as the calibration temperature. The uniformity of the heater was measured. The maximum error in the experimental heat-transfer coefficients was 6.2% with a maximum heat loss due to bladed-chord-plane conduction. They finally concluded that this method provided an accurate, quantitative, and continuous map of heat-transfer coefficients on the blade surface.

Simonich and Moffat (21) developed a technique for heat transfer measurement using cholesteric liquid crystals to infer temperature. This technique allows for the quantitative visualization of the heat transfer coefficient over a large area. They constructed a heater/temperature indicator package using the integral method. The heater is a very thin layer of nearly transparent vapor-deposited gold on one side of the plastic, virtually eliminating any contact resistance. The gold film is so thin that it still passes 80% of the light incident on it in the visible spectrum. The advantage of this method is that if a proper thickness of insulation is chosen so that no heat escapes out of the bottom, there is little temperature gradient through the liquid crystal. They studied both free-convection and laminar-forced

flows using water as a working fluid. For the laminar forced-convection case, the value of heat transfer coefficient from liquid-crystal contour line agreed with the value predicted by STAN5, a two-dimensional, finite-difference, boundary-layer code.

Measurement of the effects of a concave curvature on turbulent boundary-layer heat transfer was also investigated. They studied the frequency response of liquid-crystal package, because the vortices' effect on heat transfer would be a time-varying change in the heat transfer coefficient. Sinusoidally varying heat transfer coefficient and sinusoidally varying heat flux models were solved. They found that the frequency response for the latter case agreed well with the analytical solution. The frequency response for varying heat transfer coefficient differed by $\pm 2.5\%$ from its analytical solution.

Camci et al. (22) employed a hue capturing technique for the quantitative interpretation of liquid crystal images in convective heat transfer studies. They found that hue and temperature related linearly. This method is more advantage than that in past studies due to the ability to generate many isotherms simultaneously from a single-crystal image at a high resolution in a very time-efficient manner. It was found that this method was very suitable for transient heat transfer studies with an assumption of one-dimensional heat flow into a semi-infinite body. They captured 16 individual color images at different times. The experiment was run at Re = 30,000. They concluded that the pixel by pixel color

capturing capability of this method was extremely useful for two-dimensional processing of color information on more complex heat transfer surfaces.

Application of liquid crystal to convective heat transfer measurement can be categorized into steady state and transient experiments. The steady-state mode is appropriate for constant heat flux surface, while the transient method better suits an isothermal surface boundary condition.

Hippensteele et al. (23) evaluated a technique using a composite of heater element and liquid crystals from a complex curved surface. They employed the real time hue conversion process on a complex curved surface using a transient heat transfer technique with high spatial resolution focusing on the encapsulated liquid crystals with a narrow color band. The assumption for the transient heat transfer technique, which allows the use of one-dimensional transient heat transfer, was a small penetration depth of the thermal pulse into the plexiglas wall compared to its total thickness. The increase of wall temperature for an impulsively started heat transfer experiment can be related to time as

$$\theta = \frac{T_w - T_i}{T_{o,\infty} - T_i} = 1 - \exp(\beta^2) erfc(\beta)$$

where θ = dimensionless temperature

$$\beta = h\left(\frac{t}{\rho c_p k}\right)^{1/2}$$

It was found that the high spatial resolution of the transient method with pixel by pixel processing could be used in unsteady heat transfer.

Wang et al., (24) presented a method of processing the liquid crystal color change data obtained from transient heat transfer experiments using the full intensity history. Later they (25) chose to use the hue value as the color index and calibrated to enable the temperature to be measured for a transient experiment. They directed the conditions to choose the best method as a simple and monotonic function of the liquid crystal temperature and independence of the local illumination. Two methods employing information redundancy to achieve high accuracy and resolve more than one unknown were presented: the hue history time scaling method and the temperature history matching method. For the first method, the hue history of every surface location can be expressed by

$$H(\beta, T_{gas}, T_{initial}) = H((1-\exp(\beta^2)\mathrm{erfc}(\beta))(T_{gas}-T_{initial})+T_{initial})$$

where $\beta = \dfrac{h\sqrt{t}}{\sqrt{\rho c k}}$

h is the heat transfer coefficient

t is time

ρ is the density of the fluid

c is the specific heat capacity

k is the conductivity of fluid

The hue versus temperature calibration is not required for this method. Each hue time history is scaled to that from a reference location, where the heat transfer coefficient is known as a function of the Reynolds number.

The latter method needs the hue versus temperature calibration. The surface temperature history is related to the heat transfer coefficients, and the gas and the initial temperatures by

$$T = (1-\exp(\beta^2)\mathrm{erfc}(\beta))(T_{gas}-T_{initial})+T_{initial}$$

They reported that when the corrected values were chosen for all the parameters in the above equation, the predicted temperature history should match the temperature history obtained from the hue measurement. They found that the latter method was able to determine more than one thermal condition (in this case T_{gas} and h). It was found that hue time scaling was faster than intensity time scaling. This is because hue is independent of strength of illumination and does not need strength of signal scaling. Finally, they concluded that the liquid crystal hue change could be calibrated accurately versus temperature with high resolution.

CHAPTER III

EXPERIMENTAL SETUP

There are three main parts in this chapter. The first part deals with the air delivery system: air supply, plenum chamber, and orifice plates with both circular and cusped ellipse shapes. The second part covers the impingement surfaces for both isothermal and uniform heat flux discussing about apparatus and setup. The last one describes the temperature measuring apparatus, which are thermocouples and liquid crystals in the present study.

Air Delivery System

The air, which was a working fluid in this study, came from a 90 psia dried compressed air supply. As shown in Figure 3.1, the surge tank eliminates the pressure fluctuation of air from the supply. The air then passed to gate valve number 1, which was used to adjust pressure coarsely. The other function of gate valve number 1 was to prevent disturbing air flow settings when turning a compressor on and off. Then the air was sent to remove impurities by a filter.

A pressure regulator was placed after the filter to measure pressure after filtering. The pressure of the air after filtering was approximately 40 psia. For high velocity air, gate valve number 2 was opened and the gate valves number 3 and 4 were closed, so that the air pressure could be read by the large-scale flow meter. Then the air passed through gate valve number 2 to the plenum chamber. However, at very low velocity, the large-scale flow meter was unable to read such low scale.

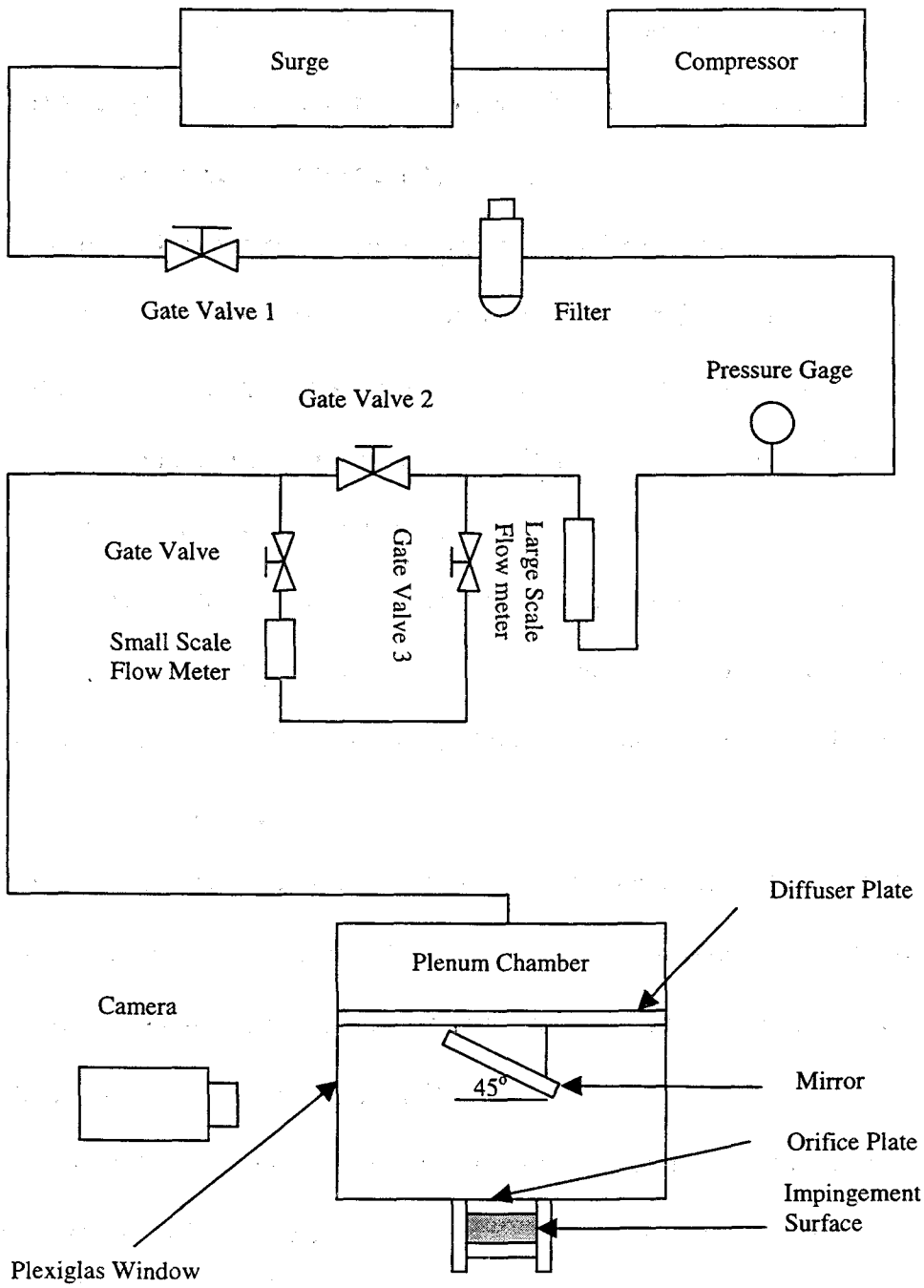

Figure 3.1. Scheme of Air Delivery System

The gate valve number 2, thus, was closed, so the air passed through the large-scale flow meter to gate valve number 3. The small-scale flow meter then read out. Next the air passed to gate valve number 4, and into the plenum chamber with the maximum pressure of 24 psia, approximately.

The plenum chamber had a dimension of $0.41 \times 0.41 \times 0.41$ meter. The air came to the plenum chamber and before flowing to the orifice plate, it passed through a diffuser. The diffuser was mounted 16 mm below the top of the plenum chamber, created uniform flow, which was the high-pressure still air, above the orifice plate. It was made of two layers of screens.

Two orifice plates used in this study were made from quartz, 1.27-mm thick. A seven-by-seven square jet array was used. Two different orifice geometries, which had the same hydraulic diameter, were tested: circular and cusped ellipse as shown in Figures 3.2 and 3.3.

A quartz orifice plate was used because of its clearness, so that pictures could be taken from above. A Sony CCD camera was used to take pictures in the experimentation of the uniform heat flux surface from a mirror that was mounted on the bottom side of the diffuser plate for 45° as shown in Figure 3.4.

Both an isothermal and a uniform heat flux impingement surface were placed onto a plexiglas base, which was mounted to the other three side walls. The setups were a little bit different for both cases due to copper bus bars, and the leads mounted to them for the uniform heat flux impingement surface. Setups for the

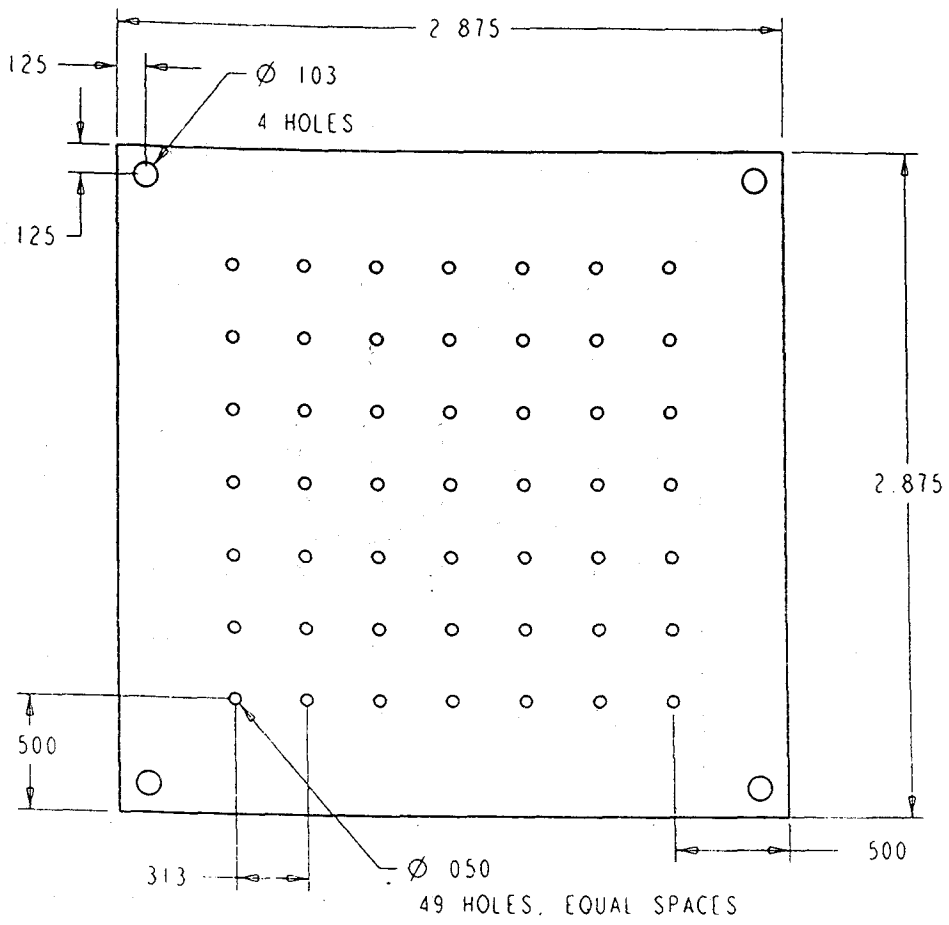

Figure 3.2. Circular Jet Orifice Plate

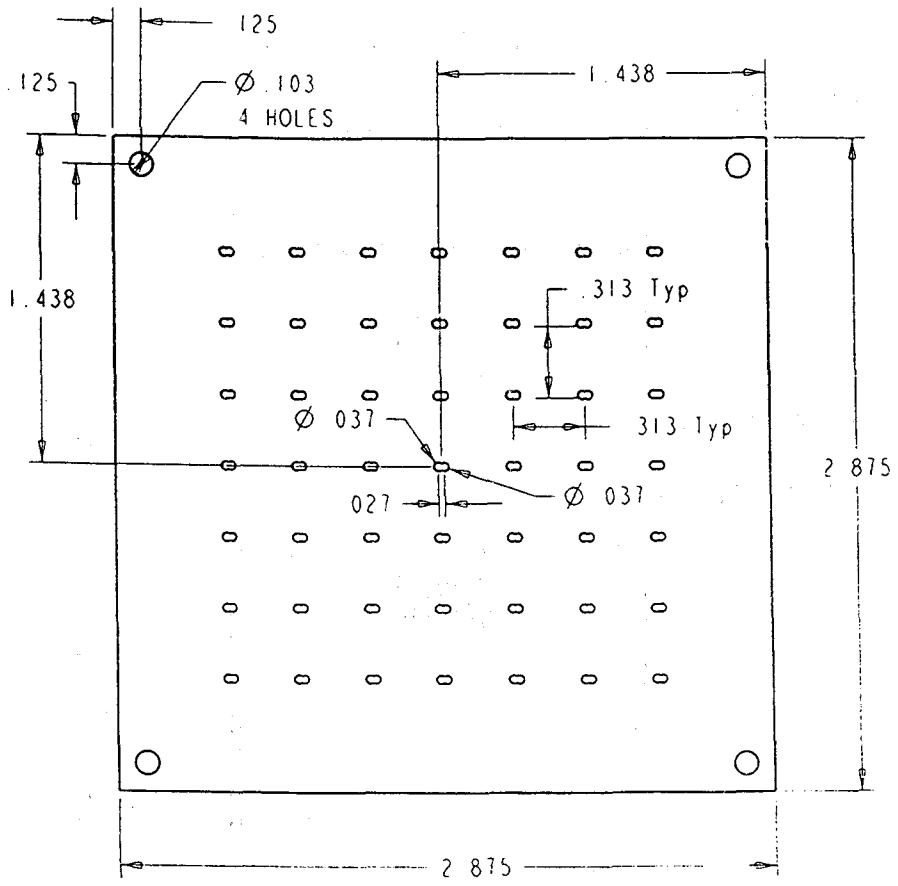

Figure 3.3. Cusped Ellipse Orifice Plate

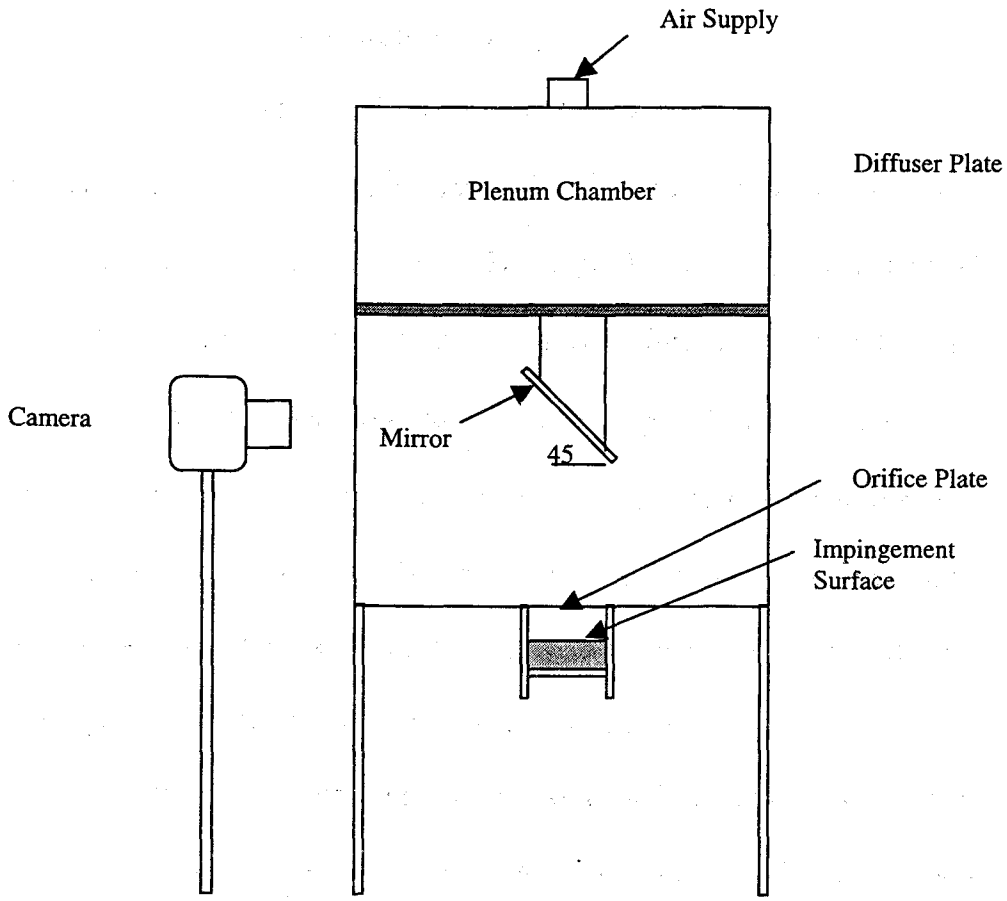

Figure 3.4. Camera Setup for Uniform Heat Flux Impingement Surface

isothermal and the uniform heat flux surface are shown in Figure 3.5 and 3.6, respectively.

Impingement Surface

Isothermal Impingement Surface

The impingement surface was a 5.556×5.556×0.635 cm copper block. There were three groves on the bottom surface of the copper block for five locations of thermocouples to measure the temperature. The heater dimension was 5×5.5 cm and 16.4-Ω resistance and was adhered to the plexiglas block of dimension 5.556×5.556×2.54 cm. A groove was made both on the top and the bottom of the plexiglas block to place thermocouples to measure the temperature difference between the top and the bottom surfaces, to calculate the heat conduction loss. The power was supplied to the heater by a 30-VDC power supply.

The impingement surface, the heater, and the plexiglas block were assembled on a plexiglas base, which was mounted to the other three plexiglas side walls. The jet-to-plate distance was adjusted by using a slot on the supporters of the plexiglas base.

Uniform Heat Flux Impingement Surface

The heater for the constant heat flux impingement surface was a sheet of 25.4 μm thick 301 stainless steel. A liquid crystal sheet was put on the top of the foil, which was on top of a 19.05-mm thick plexiglas block. The foil heater was clamped to the plexiglas block by two 0.79375-mm thick copper bus bars. To

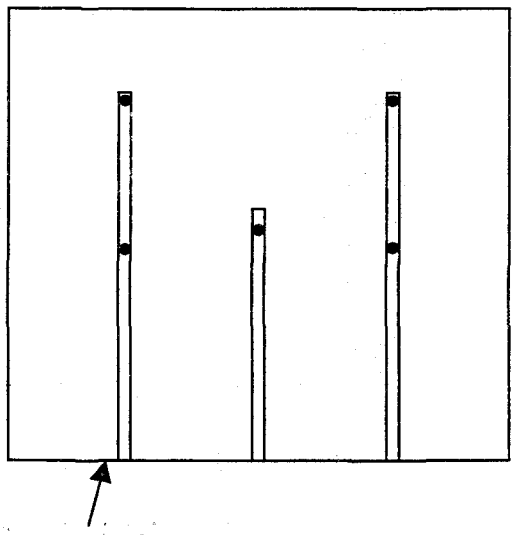

Copper block with 3 grooves for 5 locations of thermocouples

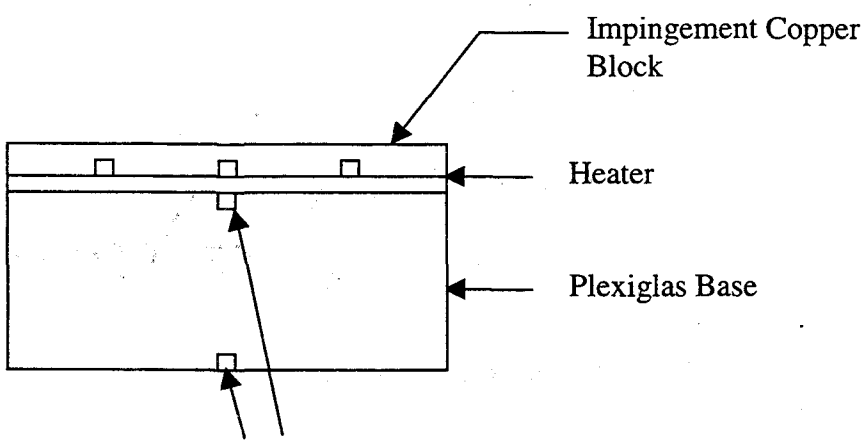

Figure 3.5. Setup of Isothermal Impingement Surface

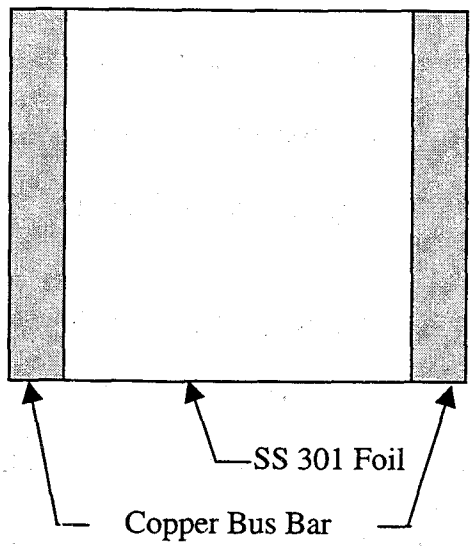

Top View of Composite

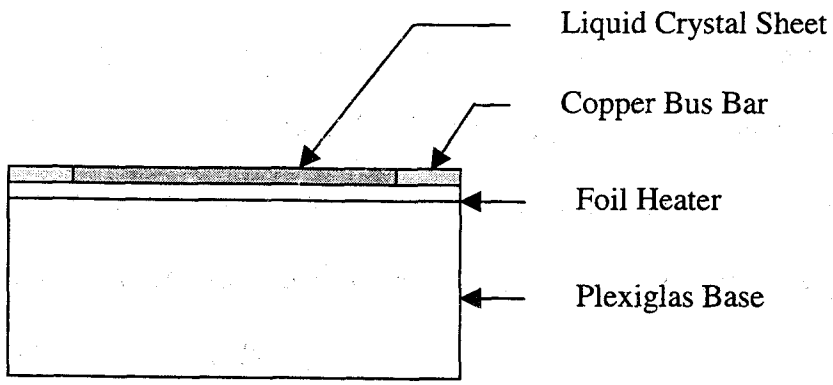

Figure 3.6. Setup of Uniform Heat Flux Impingement Surface

assure good contact between the foil and the liquid crystal sheet, high conductivity paste was used. A DC power supply was a power source for the foil heater.

The impingement surface was placed on a plexiglas base, which was a little bit wider than the impingement surface to have space for leads as shown in Figure 3.7. The leads then were connected to a DC power supply.

Temperature Measuring Apparatus

Thermocouples

Type-J thermocouples were used in the experiments. The leads of thermocouples were made from anumel. The range was from –270°C to 1,372°C. The thermocouples were connected to the input module, which was plugged into the Fluke data logger at the rear panel. The Fluke data logger had a resolution of ±0.05°C. The thermocouples were calibrated in water bath with a thermostat controlled the set temperature. The temperature was measured using a glass thermometer with resolution of ±0.1°C. The data logger with resolution of ±0.05°C was used to read out the temperature from thermocouples. The total uncertainty of the temperature readings from the thermocouples was ±0.11°C (See Appendix A for uncertainty analysis details).

Liquid Crystals

A sheet of liquid crystals, R25C5W manufactured by Hallcrest, Co. was used in the present study. The sheet changed color over a range of 5°C starting from approximately 25°C. The liquid crystals were used to indicate a heating

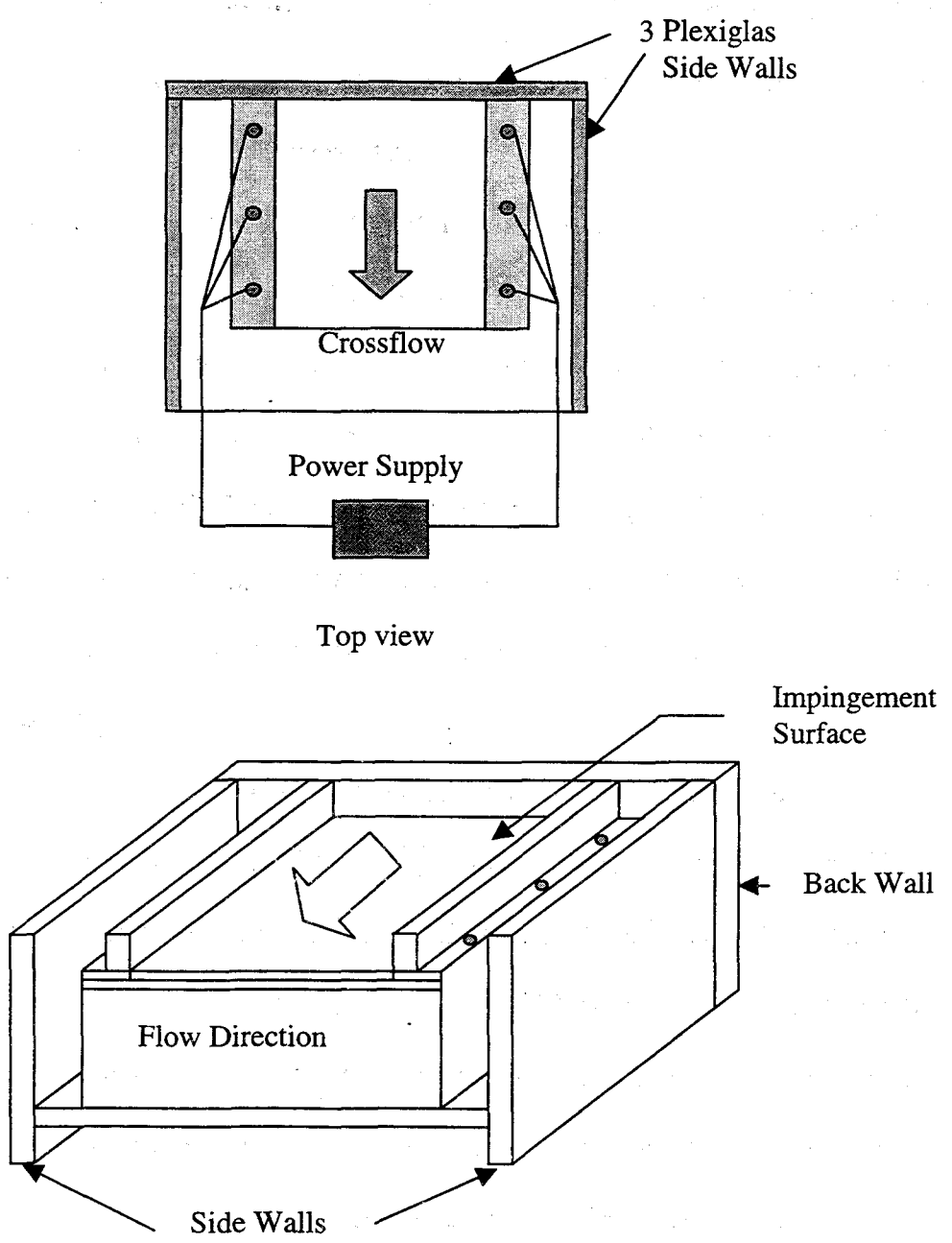

Figure 3.7. Uniform Heat Flux Impingement Surface Surrounded by Three Side Walls and Crossflow

surface temperature profile for all points on the surface. Before running the experiment, the liquid crystals were calibrated for the correlation between temperature and hue of the liquid crystals.

In order to calibrate the liquid crystals, the apparatus was put together. Two copper bus bars that were used to heat up a stainless steel foil were placed onto a plexiglas base. Five thermocouples were put between the foil and the liquid crystal sheets. A plexiglas frame was put on top of the liquid crystal sheet. The temperature was controlled by adjusting the current and the voltage of the power supply. A picture of the liquid crystal sheet was taken by a SONY CCD video camera. The image was imported into a computer and analyzed using MATLAB Imaging Toolbox.

The image file that was imported into the computer was in RGB or red-green-blue format. Each pixel of the image had the value of red, green, and blue, which could be mixed to make any other colors. MATLAB created three matrices of those three primary colors. However, the RGB signal is very sensitive to surrounding conditions such as background lighting and angle between lights and liquid crystal surface. To reduce that sensitivity, alternative way can be used to interpret data, which is the value of hue, saturation, or intensity. Nevertheless, the hue value was chosen to use because it is related to the dominant wavelength of color, and has less variation with changes in saturation and intensity. Comparing to the RGB value, the hue value is less sensitive to the angle of lighting.

The MATLAB program with Image Processing Toolbox was used to convert the RGB input image file to a file containing hue value. The hue value was then related to temperature.

In this study, the calibration of liquid crystal was carried out between the temperatures of 26.01 and 29.22°C, with twenty increments of 0.2°C. The average hue value for each frame according to the temperature was recorded as shown in Figure 3.8. The uncertainty of the temperature was estimated from the uncertainty of thermocouples, the uncertainty of the hue value, and the average hue value taken for each frame. The temperature for each hue value between calibration points was found using linear interpolation. The uncertainty of the temperature was found to be ±0.03°C.

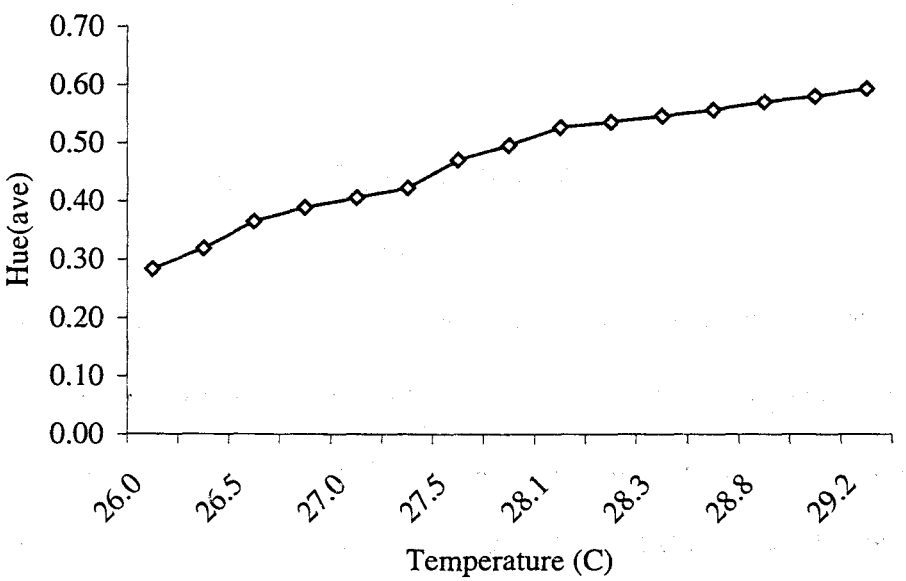

Figure 3.8. Hue vs. Temperature (Liquid Crystal Calibration)

CHAPTER IV

EXPERIMENT PROCEDURE AND ANALYSIS

This chapter is divided into two parts, the experimental procedure for isothermal impingement surface and for uniform heat flux impingement surface. Each part is discussed relative to the test plan, experimental procedure, and data reduction.

Isothermal Jet Impingement Surface

Test Plan

The air jets from a seven-by-seven square array of a peanut-shaped and a circular orifice plates impinge on the isothermal surface. Data were taken over nominal volume flow rates of 8, 10, 11, 12 and 14 cfm, and the jet-to-plate distances (H/D_h) of 1, 2, 3, and 4 for each Reynolds number. The measured parameters were

- Surface temperature, T_s
- Plenum temperature, T_j
- Plenum pressure, P_p
- Heater input voltage, V
- Heater input current, I

Then the parameters that are reported for the test based on those measured parameters are the average heat transfer coefficient, $\overline{h}$, and Nusselt number as a

function of Reynolds number and jet-to-plate distance. Finally, the results are compared to the available information in the literature.

Experimental Procedure

Reynolds number used here is based on single jet area. The relationship is given by

$$\mathrm{Re} = \frac{\rho V D_h}{\mu} \tag{4.1}$$

where $V = \dot{Q} / A$

Then the heater is activated, and the surface temperature are monitored until a steady state is reached, which means that the temperature is constant. The one-dimensional conduction losses are less than 1.5% of the input power; they are neglected. Finally, the data mentioned above are recorded.

Data Reduction

At the steady state condition, an energy balance over the heated copper block can be performed as

$$q_{in} = q_{out} \tag{2}$$

The heater supplies the input energy with constant resistance. Therefore,

$$q_{in} = \frac{V^2}{R} \tag{3}$$

$$q_{out} = \bar{h} A_s (T_s - T_j) \tag{4}$$

Since the conduction loss is less than 1.5% of the input energy, this amount is negligible. Thus, the energy balance becomes

$$\frac{V^2}{R} = \bar{h} A_s (T_s - T_j) \tag{5}$$

And the average heat transfer coefficient, which is the only unknown in the above equation, can be found. The heat transfer coefficient can be reported in term of Nusselt number:

$$\overline{Nu} = \frac{\bar{h} D_h}{k_{air}} \tag{6}$$

The uncertainty for $\bar{h}$ varies from 1.75% to 2.39%. The uncertainty for $\overline{Nu}$ is from 2.07% to 2.64%. The uncertainty of Reynolds number was from 4.27% to 6.67% (Reference Appendix A).

Uniform Heat Flux Jet Impingement Surface

Test Plan

Similar to those for the isothermal jet impingement surface, a circular and cusped ellipse plates are used. The conditions required in this case are also over the nominal volume flow rates of 8, 10, 11, 12 and 14 scfm, and the jet-to-plate distances (H/D_h) of 1, 2, 3 and 4. The measured parameters are the same as those for the isothermal surface case except for the method of measurement of the surface temperature. In this case, the temperature for each pixel in the image is required according to the data obtained from the liquid crystal calibration.

The required parameters for heat transfer distribution are also the average heat transfer coefficient ($\bar{h}$) versus flow rate, and reported in the form of the average Nusselt number ($\overline{Nu}$) versus Reynolds number at each jet-to-plate distance.

Experiment Procedure

The steady state method is used in the experiment. First, the desired jet plate is inserted to the bottom plate of the plenum chamber. Then, the uniform heat flux surface is placed underneath the plenum chamber. The jet-to-plate spacing then is adjusted in order to create proper H/D_h spacing. Next, the liquid crystals are lined up beneath the jet array by looking through the mirror. Once they are lined up, the power supply is turned on to allow the foil heater to begin heating, and the required air flow rate is set. Both temperature and air flow rate are allowed to stabilize. The CCD camera is adjusted in order to get the liquid crystals in focus. Now a test is ready. Finally, the image taken by the CCD camera is imported to the computer.

Data Reduction

An image in TIFF format taken by the CCD camera has a number of pixels. Each pixel contains the value of RGB or Red-Green-Blue. Then the image of 480x640 pixels is converted into a 480x640 matrix of hue value by using MATLAB Image Processing Toolbox. According to the calibration of liquid crystals, the hue values are thus converted into temperature. Therefore, a matrix of the values of temperature is obtained.

At locations in the matrix that the temperature information is not available, depending on the information from the calibration of the liquid crystals, those points are assigned to be zero. Then they are replaced by the median value of a three-by-three neighborhood around the corresponding pixel. The next stage is to determine the heat transfer coefficient for each pixel location. Then, the heat transfer coefficient matrix is obtained.

The MATLAB program creates a data file containing the temperature matrix, the local heat transfer coefficient matrix, the average temperature and the heat transfer coefficient. Both of the average temperature and the heat transfer coefficient were based upon the pixels with sufficient information of temperature only. Moreover, the surface plots of the Nusselt number were created for the better demonstration as well as the sliced view of the three-dimensional plots. The sliced view demonstrates the comparison of the results from different jet geometries and test conditions.

CHAPTER V

RESULTS AND DISCUSSION

This section discusses the result of the experiments, which are divided into three main sections: isothermal surface jet impingement, uniform heat flux surface jet impingement, and the comparison of the results of the two methods. In the first section, the results of average heat transfer distribution are discussed. While, the second section discusses both local and average heat transfer distributions. Finally, the average heat transfer coefficient distributions from both isothermal and uniform heat flux impingement surfaces were compared. The experiments for each part was done for the circular and cusped ellipse orifices, which have the same cross sectional area. For each geometry, five flow rates which correspond to the nominal flow rates of 8, 10, 11, 12 and 14 cfm, were tested, each at four jet-to-plate spacings from 1 to 4 hydraulic jet diameters.

Isothermal Impingement Surface

Circular Jet Array

Figure 5.1 shows the plot of the average Nusselt versus Reynolds number for four H/D_h values for the circular jet array. For all H/D_h values, Nusselt number increases linearly with Reynolds number based on the regression analysis. Slopes of these lines are all very similar. For H/D_h of 1, the Nusselt number is slightly more sensitive to the change of the Reynolds number. The trend for H/D_h equal to 1

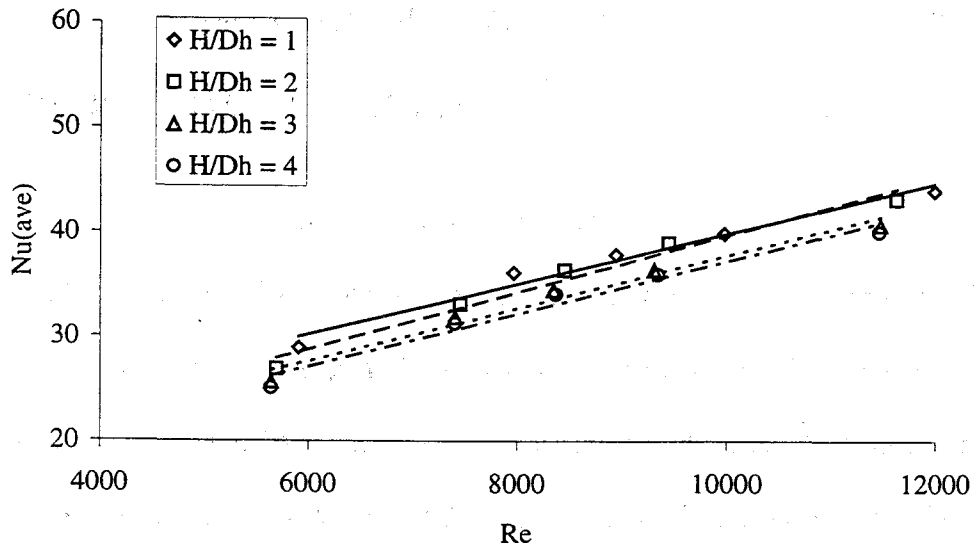

Figure 5.1. Nusselt number vs. Reynolds number, Isothermal, Circular Jets

gives the highest Nusselt number compared to the other impingement distances at the same Reynolds number. From the plot, the results for H/D_h values of 1 and 2 are very close to each other, and the results for H/D_h values of 3 and 4 are very close to each other. The results for H/D_h of 2 and 3, differ from 3.78 to 6.63%. This is within the range of uncertainty for these data.The correlation found for the circular jet array is

$$Nu = 0.1135\,\mathrm{Re}^{0.64}(H/D_h)^{-0.088} \tag{5.1}$$

where $5500 \leq \mathrm{Re} \leq 12000$ and $1 \leq H/D_h \leq 4$.

Cusped Ellipse Jet Array

Similar to the data for the circular jet array, results are shown in Figure 5.2. The slopes of all curves for cusped ellipse jets are linear, and similar in shape to one another. From the regression analysis of the data, for H/D_h equal to 1 yields the highest Nusselt number. The smaller H/D_h values give higher Nusselt numbers. Again, as for the circular jets the results for H/D_h of 1 and 2 are very close to each other as well as are those for H/D_h of 3 and 4. These differences are within the range of the uncertainty for the data. The results for H/D_h values of 2 and 3 are 2.79 to 6.11% different. Only at the lowest Reynolds number, the difference is within the uncertainty of the data. The correlation of the Nusselt number, Reynolds number, and the H/D_h value is found as following

$$Nu = 0.1289\,\mathrm{Re}^{0.63}(H/D_h)^{-0.11} \tag{5.2}$$

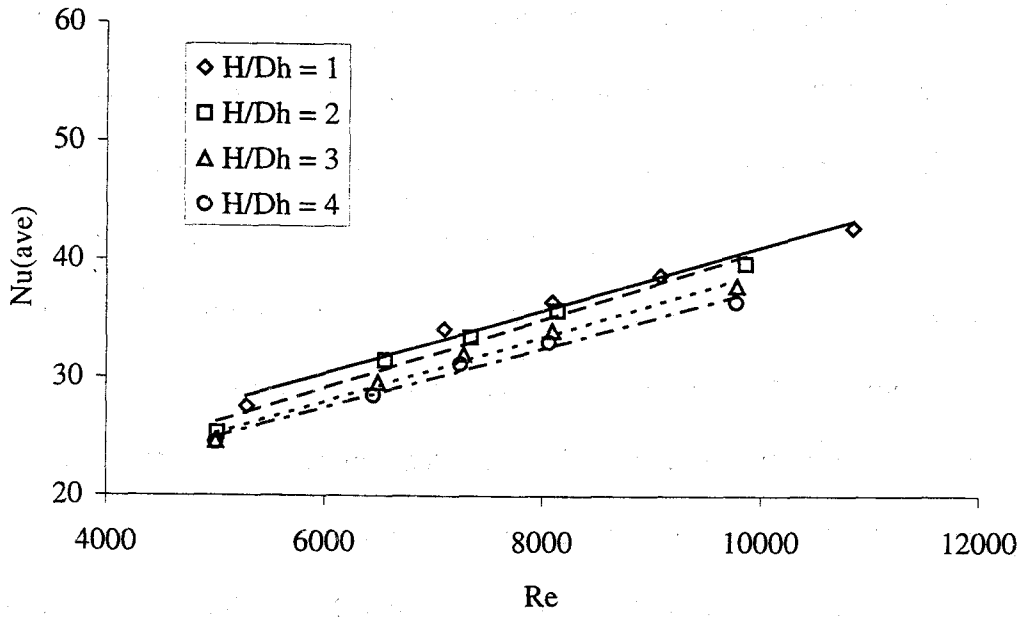

Figure 5.2. Nusselt number vs. Reynolds number, Isothermal, Cusped Ellipse Jets

where $5000 \leq Re \leq 10000$ and $1 \leq H/D_h \leq 4$. In general the correlations of equations (5.1) and (5.2) are very close.

Comparison of Results for Both Geometries

Figure 5.3 shows the plots of the average Nusselt number versus Reynolds number for both geometries at each H/D_h for the isothermal impingement surface. It is shown that for every H/D_h the cusped ellipse jets give a slightly better performance than the circular jets for the same Reynolds number. From the trend of the plots for each jet-to-plate spacing, at the higher Reynolds number, the cusped ellipse jet array gives higher results, while at the lower Reynolds number, especially below 5000, the circular jet array tends to give a better performance.

Since the two geometries were not evaluated at exactly the same Reynolds number, due to the different hydraulic diameters, the comparison cannot be described numerically. However, comparison can be demonstrated in terms of the heat transfer coefficient and volume flow rate instead of Nusselt number and Reynolds number respectively. This is shown in Figure 5.4. Here it is seen that the circular jet array gives a better performance than the cusped ellipse jet array in terms of average heat transfer coefficient at a given volume flow rate. For both geometries, the heat transfer coefficient increases linearly with the volume flow rate. Slopes of curves for both geometries at the same jet-to-plate spacing are similar. The difference of the results for both geometries for H/D_h equal to 1 at the flow rate of 0.0042 and 0.0056 m^3/s is 10.43 and 5.47%, respectively. At other flow rates for the same H/D_h, the differences differ from 2.76 to 3.67%. These are within

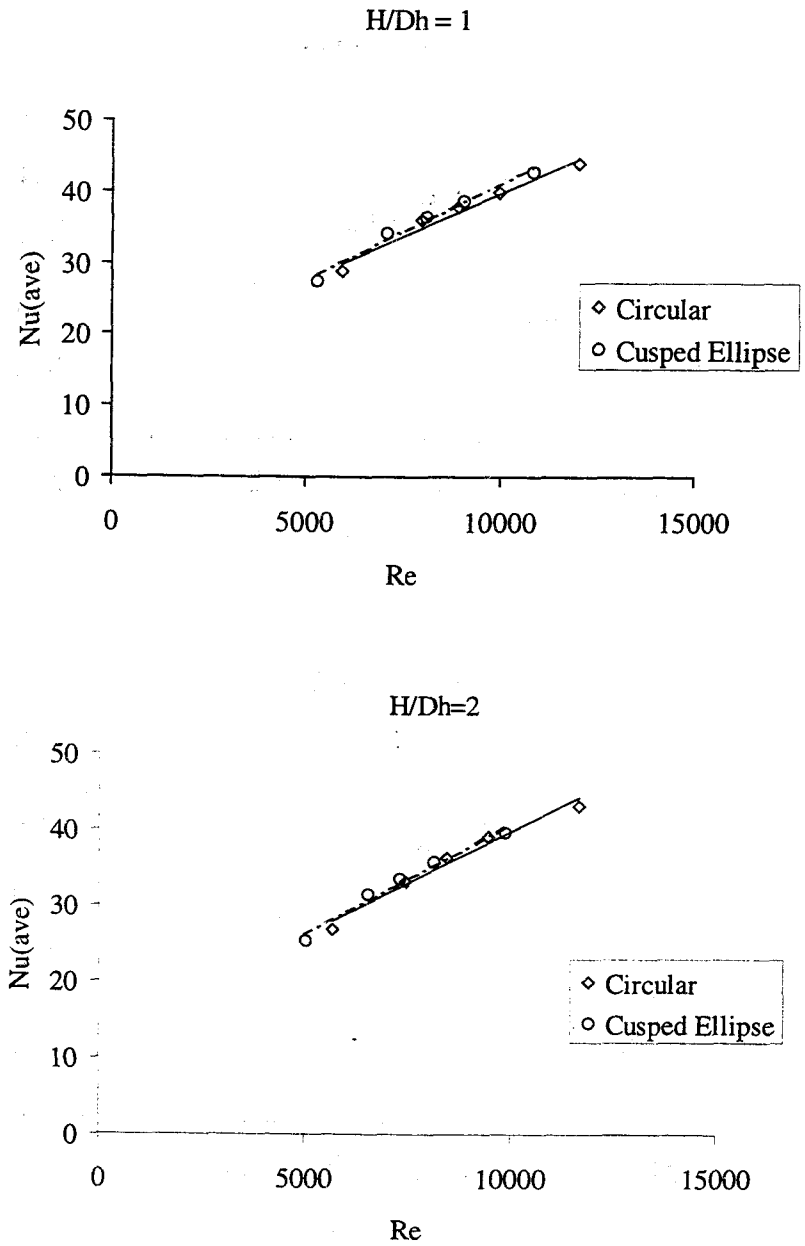

Figure 5.3(a). Nusselt Number vs. Reynolds number, Isothermal Impingement Surface

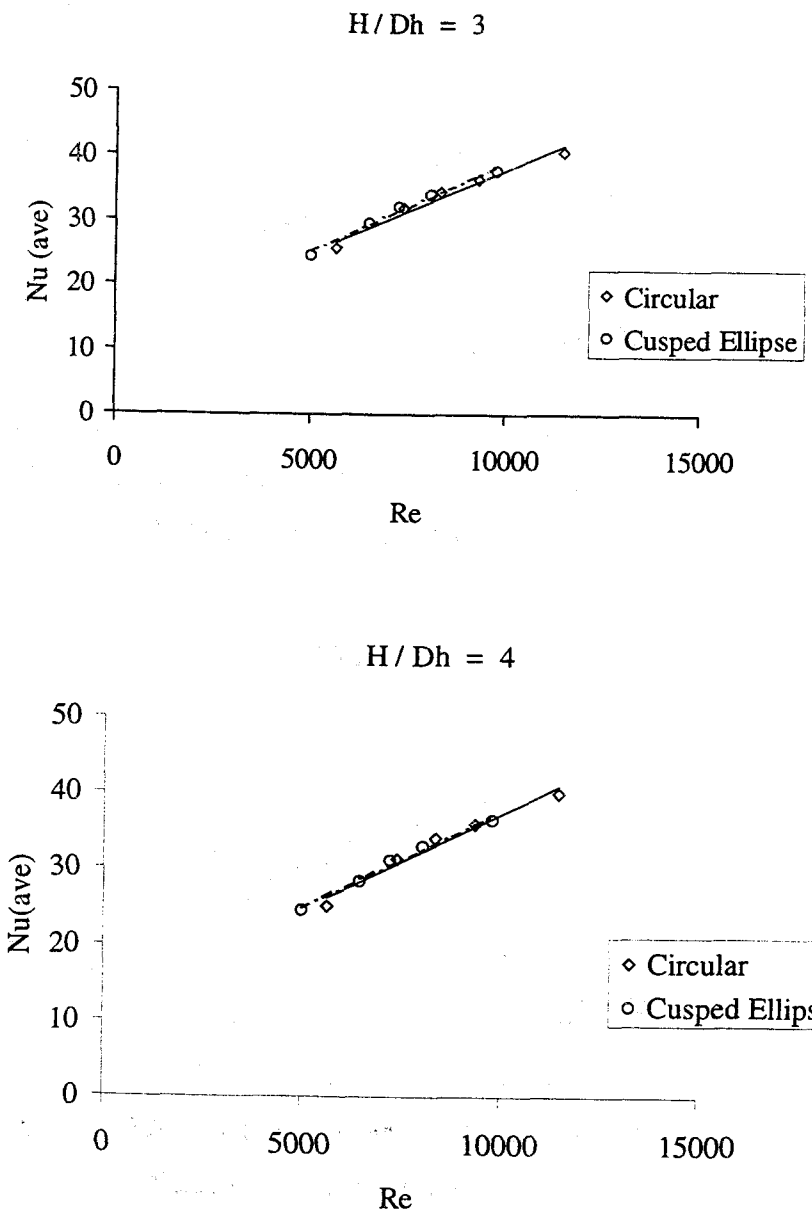

Figure 5.3(b). Nusselt Number vs. Reynolds Number, Isothermal Impingement Surface

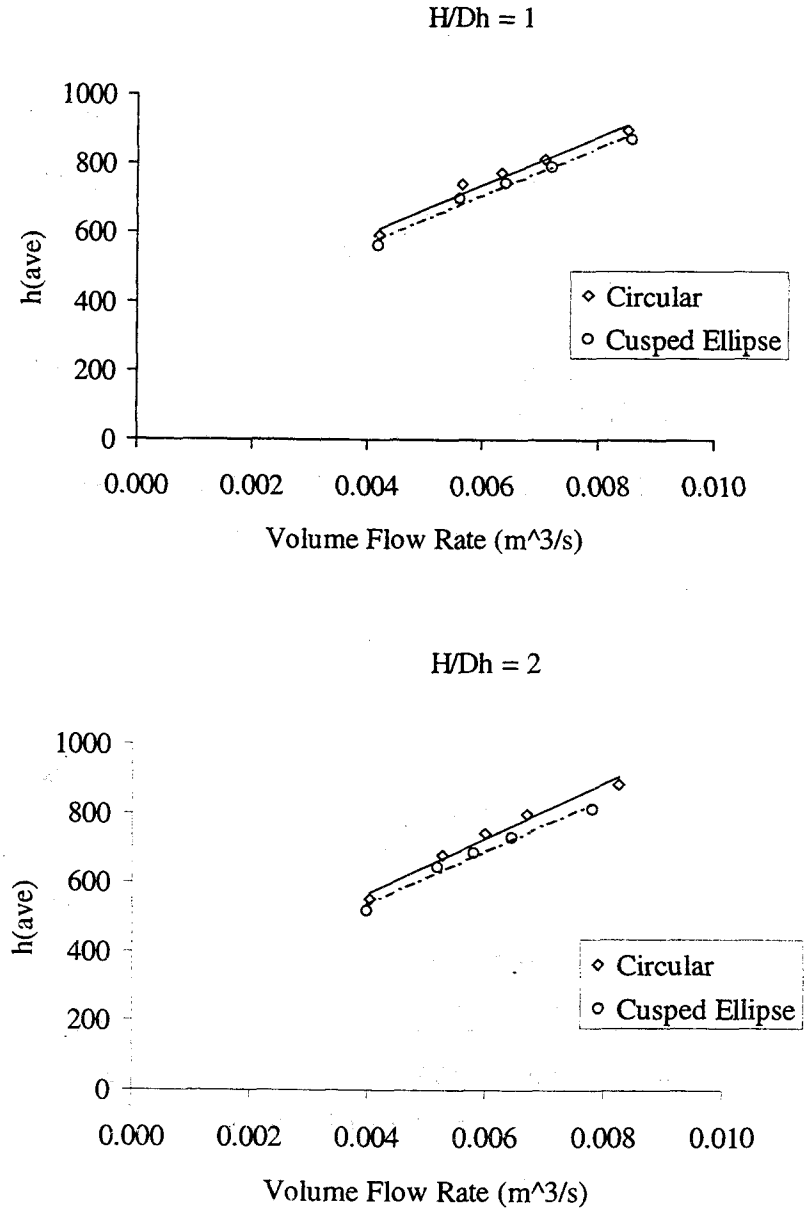

Figure 5.4(a). Average Heat Transfer Coefficient vs. Volume Flow Rate, Isothermal Impingement Surface

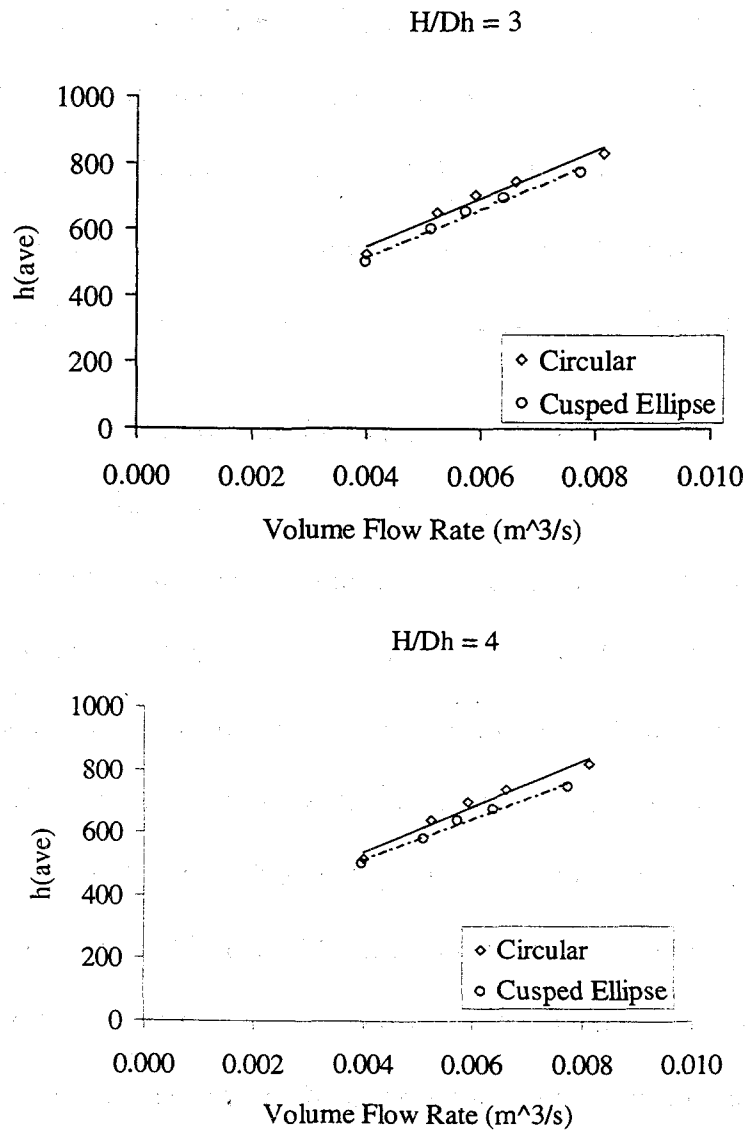

Figure 5.4(b). Average Heat Transfer Coefficient vs. Volume Flow Rate, Isothermal Impingement Surface

the range of uncertainty for these data. The difference for the results for H/D_h equal to 2 is between 4.88 and 8.31%. For H/D_h of 3, it ranges from 3.96 to 7.19%. For H/D_h of 4, at the flow rate of 0.004 m^3/s, the circular jets give a higher average heat transfer coefficient than the cusped ellipse jets by 2.34%, which is in the range of uncertainty for the experiment. At the other flow rates, the circular jets give higher average heat transfer coefficients than the cusped ellipse jets by 8.13 to 8.97%.

Comparison to Results in the Literature

The results of the present study is compared to those of Metzger et al. (7) and Obot and Trabold (8) as shown in Figure 5.5 because they used a similar set-up for the same jet geometry, a circular jet array with the crossflow. At the H/D_h equal to 1, the results of the current study are similar to those of Mezger et al. (7) rather than Obot and Trabold (8). This is because Obot and Trabold (8) used jet-to-plate spacings ranging from 2 to 16, while Metzger et al. (7) used those ranging from 1 to 3. Furthermore, Obot and Trabold (8) used jet diameters of 3.175 mm, while the current study used the same diameter as Metzger et al. (7) did, which was 1.27 mm. At H/D_h equal to 2, the results from the current study are more similar to those of Obot and Trabold (8) than Metzger et al. (7), since Metzger et al. (7) used an unequal jet-to-jet spacing for the streamwise and spanwise direction, which were 8 and 10 diameters, respectively. Obot and Trabold (8) used the streamwise and spanwise jet-to-jet spacings of 5.6 and 4 diameters, respectively. The current study used the jet-to-jet spacing of 6.25 for both directions. At H/D_h value of 3, the present study results are 1.49 to 4.09% different from the results of Metzger et al.

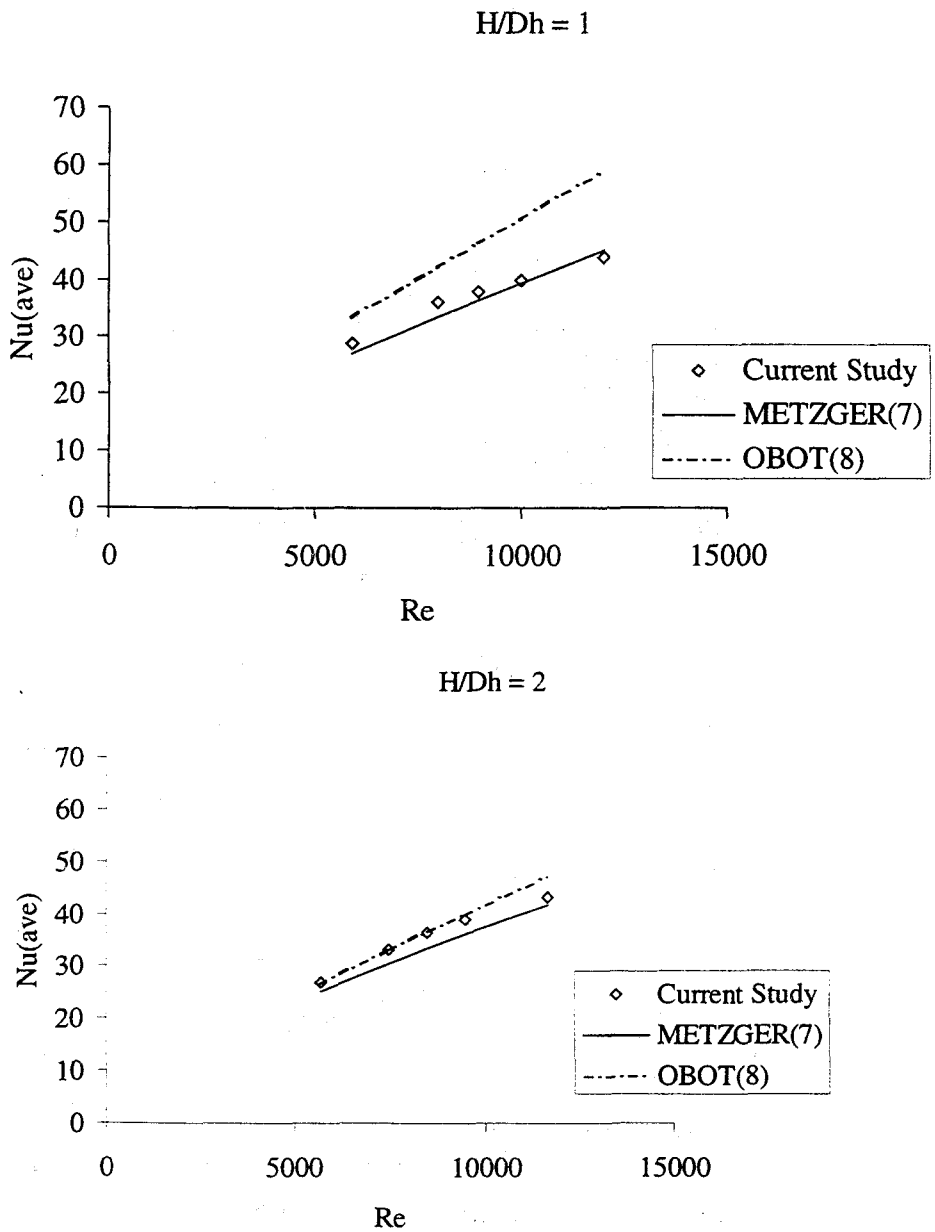

Figure 5.5(a). Comparison to Literature, Isothermal, Circular Jets

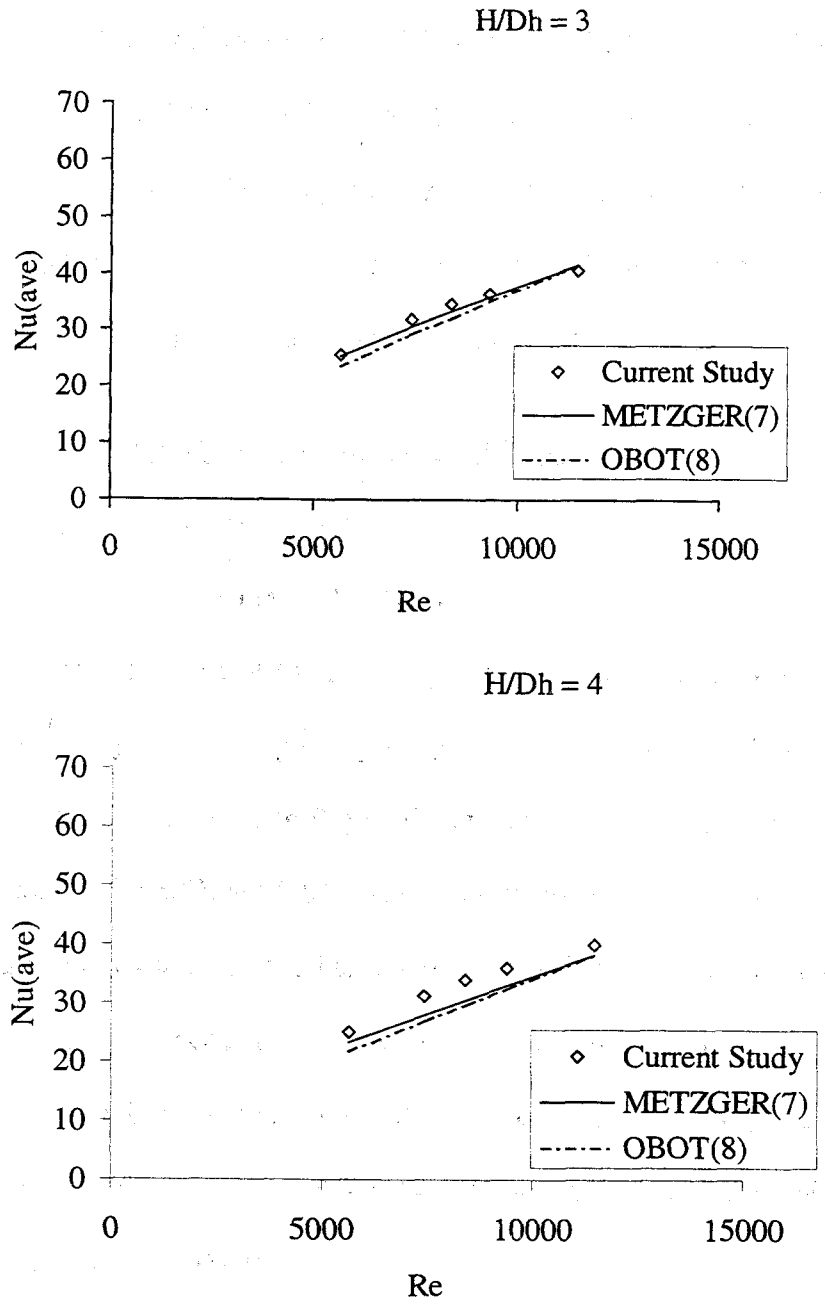

Figure 5.5(b). Comparison to Literature, Isothermal, Circular Jets

(7). Interestingly, at H/D_h of 4, the current study has results more similar to the result of Metzger et al. (7) for the same H/D_h. The results of Metzger et al. (7) were valid for the H/D_h values of 1 to 3, while those of Obot and Trabold (8) were valid for H/D_h values from 2 to 16. Overall, the significant factors that result in the differences are the jet-to-plate spacing employed in each study, the jet size, and the size of the jet-to-jet spacings in both streamwise and spanwise directions.

Uniform Heat Flux Impingement Surface

Average Nusselt Number

Circular Jet Array

Figure 5.6 shows the plot of the average Nusselt number versus Reynolds number for the circular jet array impinging on a uniform heat flux surface. The Nusselt number increases linearly with Reynolds number for all H/D_h values. The difference of the results for different H/D_h values is interesting. The results for the H/D_h of 1 and 2 are very close to each other in the range of 0.94 to 3.95% different. This is within the range of uncertainty for these data. The results for the H/D_h of 3 and 4 are also very close, but somewhat more different than that for H/D_h of 1 and 2, with a difference ranging between 8.04 and 14.05% with the lower H/D_h values. The correlation was found as follows

$$\overline{Nu} = 0.1264\,\mathrm{Re}^{0.68}(H/D_h)^{-0.135} \tag{5.3}$$

which is valid for $5500 \le \mathrm{Re} \le 11000$ and $1 \le H/D_h \le 4$.

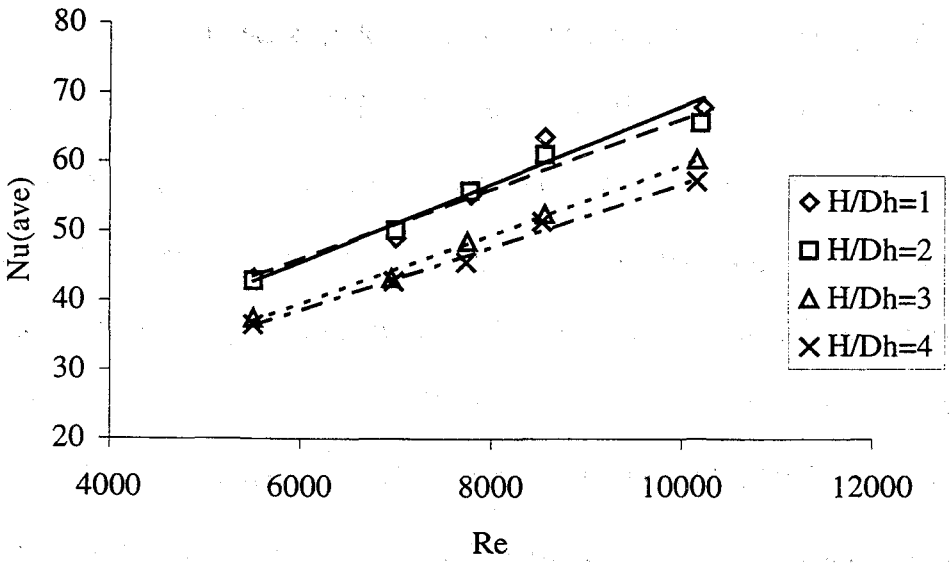

Figure 5.6. Nusselt Number vs. Reynolds Number, Uniform Heat Flux, Circular Jets

Cusped Ellipse Jet Array

The plot of the average Nusselt number versus Reynolds number for the cusped ellipse jet array is shown in Figure 5.7. The Nusselt number increases linearly with Reynolds number. The H/D_h of 1 gives the best result for all values of Reynolds number, and is the most sensitive to the change of the Reynolds number. The plot for H/D_h of 2 is the second most sensitive to the change of Reynolds number. The H/D_h of 3 and 4 yielded similar sensitivities to the change of the Reynolds number. The values of Nusselt number for H/D_h of 1 is 1.19 to 13.02 higher than that of the H/D_h of 2. The difference between the results for the H/D_h of 3 and 4 is in the range of 1.14 and 8.18%. This is within the range of uncertainty for these data. Remarkably, like in the case of the circular jet array, the difference between the Nusselt numbers for the H/D_h of 2 and 3 lies between 6.10 and 14.02%. At a Reynolds number of 9000, the Nusselt number for the H/D_h of 1 is 23.44% higher than that for the H/D_h of 4. The correlation of the average Nusselt number, the Reynolds number, and the jet-to-plate spacing for the cusped ellipse jets was found as follows

$$\overline{Nu} = 0.124\,\mathrm{Re}^{0.7}(H/D_h)^{-0.184} \tag{5.4}$$

where $5500 \le \mathrm{Re} \le 10000$ and $1 \le H/D_h \le 4$.

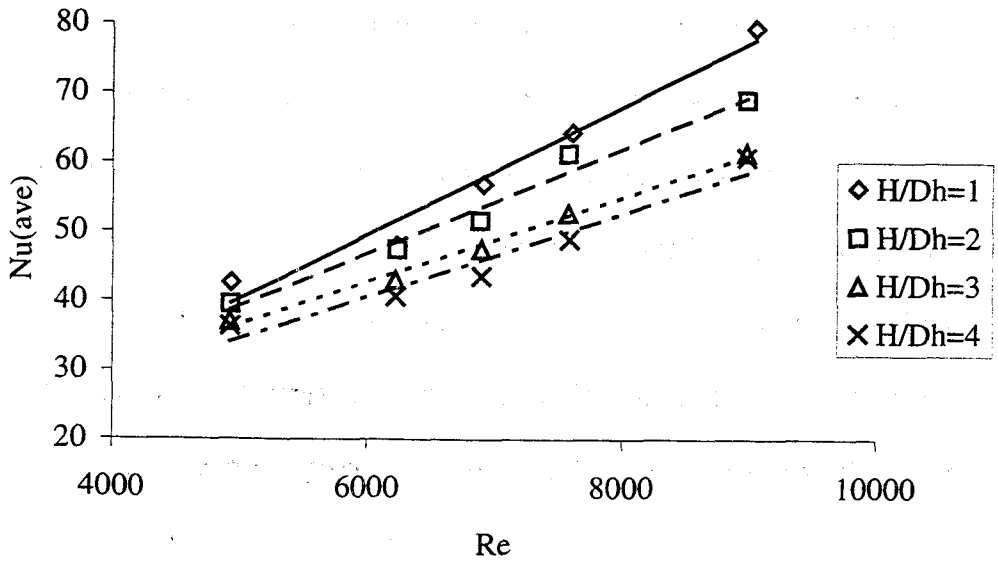

Figure 5.7. Nusselt Number vs. Reynolds Number, Uniform Heat Flux, Cusped Ellipse Jets

Comparison of Results for Both Geometries

Figure 5.8 shows the comparison of the results of the average Nusselt number versus Reynolds number for the circular and cusped ellipse jet arrays. For all H/D_h, the cusped ellipse jet array gives better performance than the circular jets, especially at the higher Reynolds number. In the plot of the average Nusselt number versus Reynolds number, the cusped ellipse jets have the more sensitivity of the average Nusselt number to the change of Reynolds number than the circular jets, especially at H/D_h of 1. Since both geometries do not give the same Reynolds number at the same flow rate, the clear explanation for this figure cannot be done numerically because the hydraulic diameter for the cusped ellipse jet are not identical to the circular jet. Therefore, the comparison of the results for both geometries in terms of the average heat transfer coefficient and volume flow rate can be presented more clearly in place of the average Nusselt number and Reynolds number in the next figure.

Figure 5.9 shows the plot of the average heat transfer coefficient versus volume flow rate in order to compare the results of both geometries. There is a crossover between the plots for the circular jet array and the cusped ellipse jet array for each jet-to-plate spacing. At the lower flow rate, the circular jet array tends to give a better performance. However, at the higher flow rates, the cusped ellipse jet array gives better results. At H/D_h of 1, the crossover occurs at a lower flow rate. At the volume flow rate of 0.0072 m^3/s, the cusped ellipse jet array yields 11% higher average heat transfer coefficient than the circular jet array. At other volume

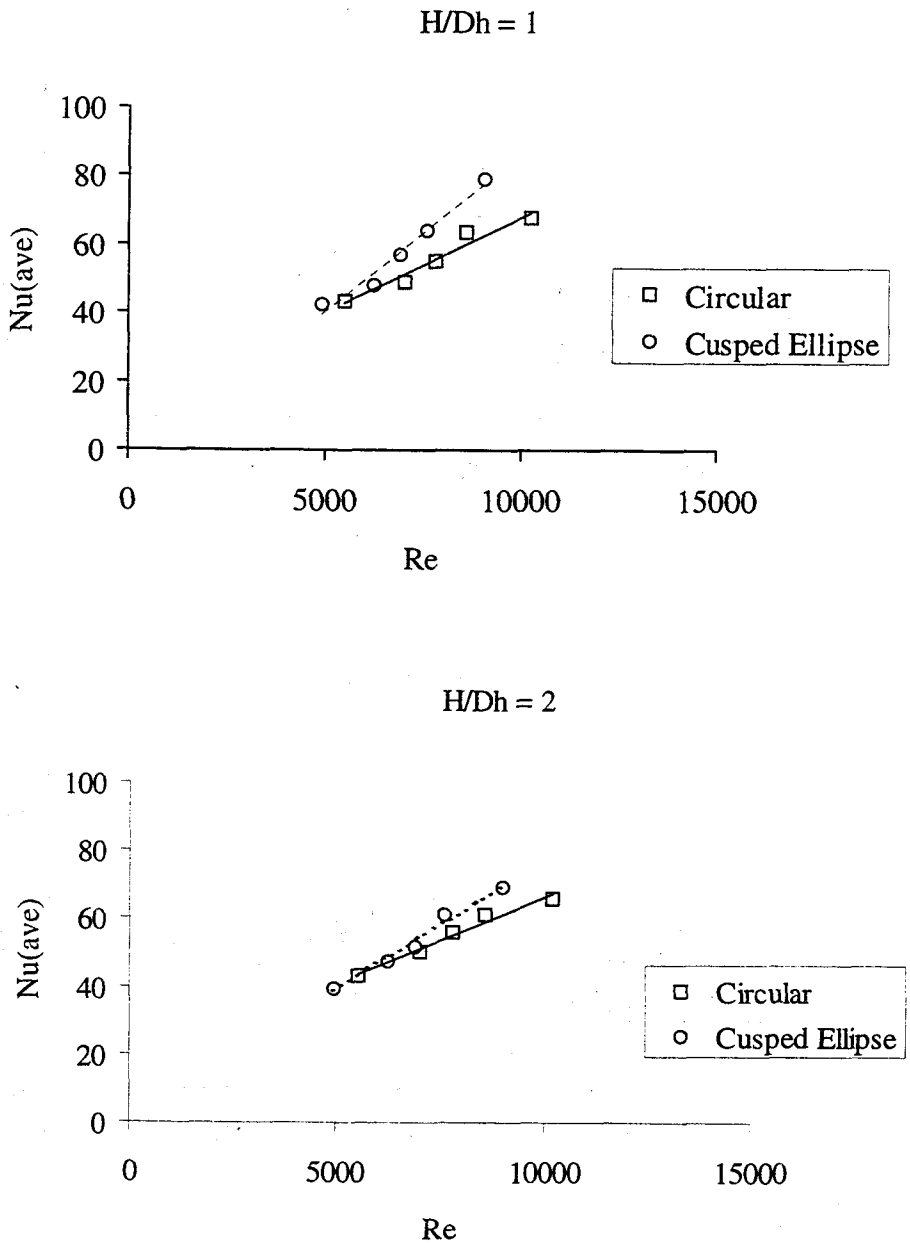

Figure 5.8(a). Nusselt Number vs. Reynolds Number, Uniform Heat Flux

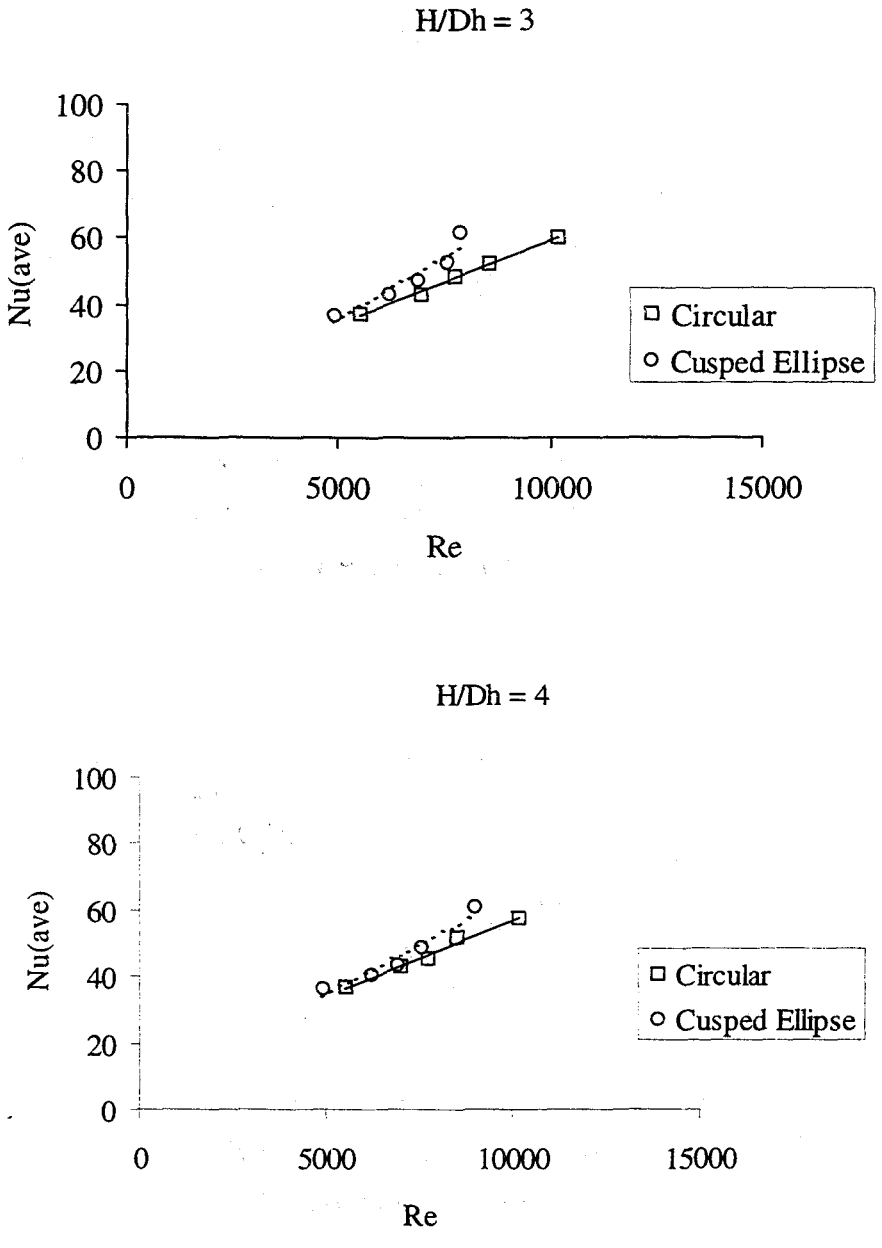

Figure 5.8(b). Nusselt Number vs. Reynolds Number, Uniform Heat Flux

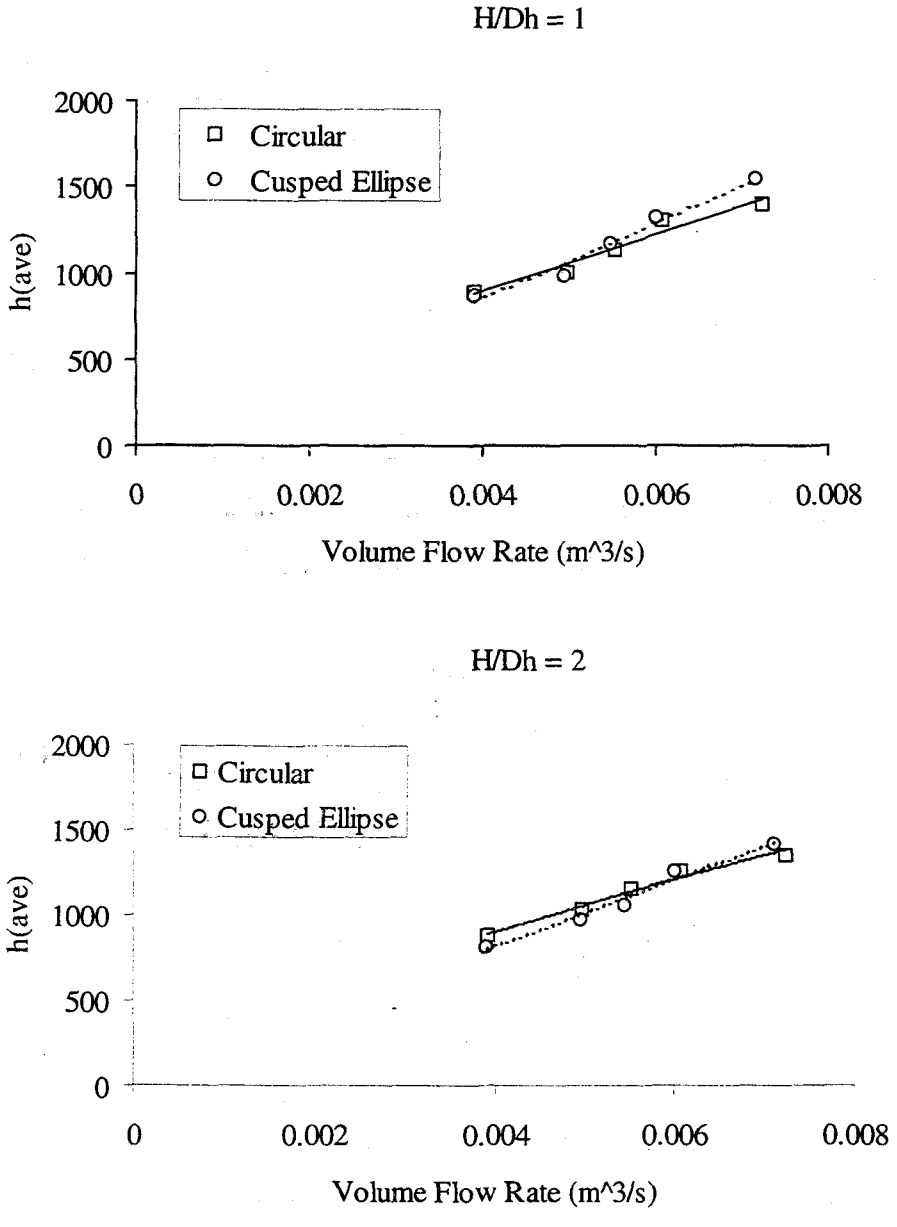

Figure 5.9(a). Average Heat Transfer Coefficient vs. Flow Rate, Uniform Heat Flux

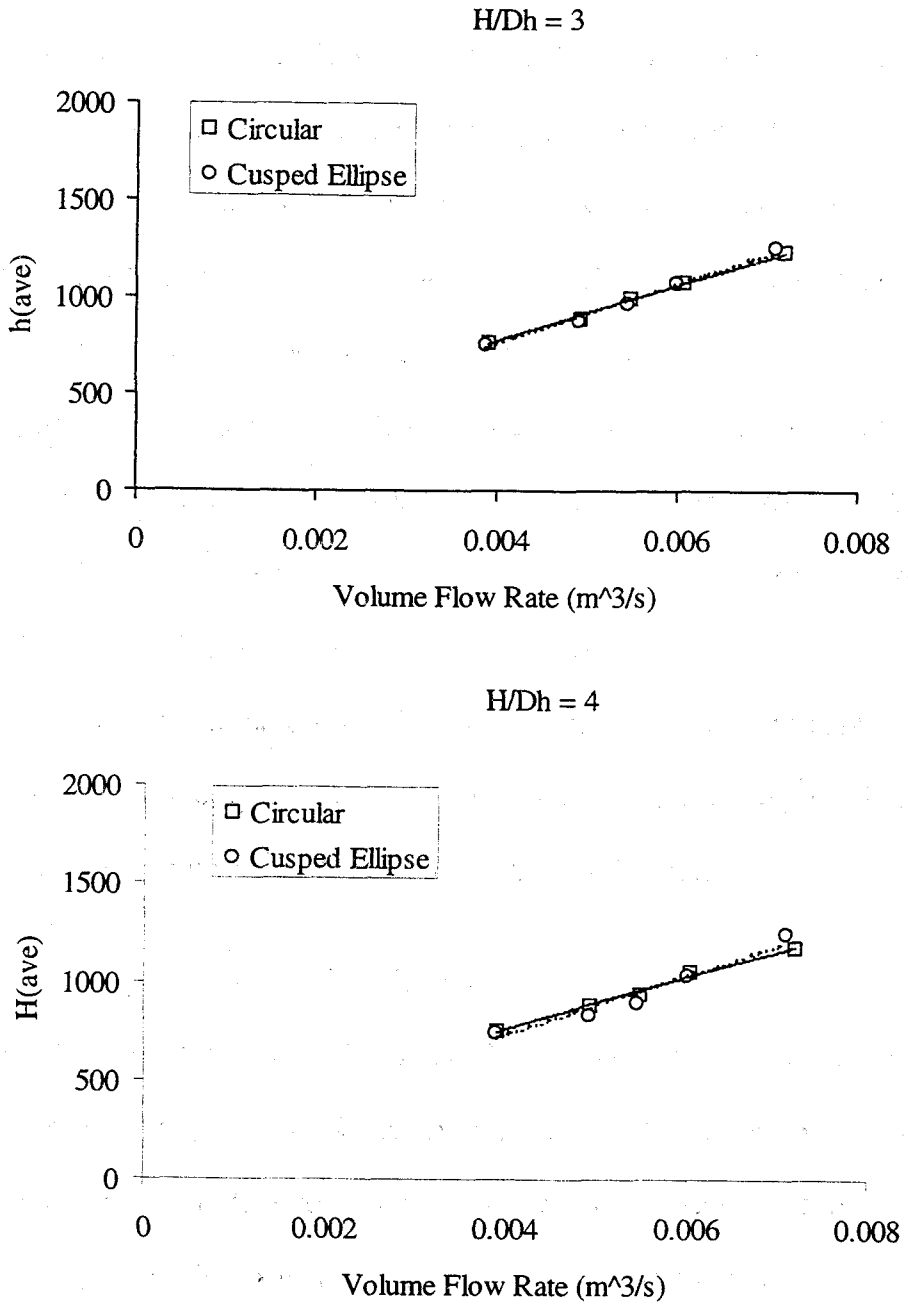

Figure 5.9(b). Average Heat Transfer Coefficient vs. Flow Rate, Uniform Heat Flux

flow rates at H/D_h of 1, the difference is in the range of 1.02 and 2.99%. This is in the range of uncertainty for these data. At H/D_h of 2, the crossover occurs at a higher flow rate than that for H/D_h of 1. For example, at the volume flow rate of 0.039 m^3/s, the circular jet array gives an average heat transfer coefficient 8% higher than the cusped ellipse jet array. At the flow rate of 0.0072 m^3/s, the cusped ellipse jet array performs 5% better than the circular jet array. This is within the range of uncertainty for the data. At H/D_h of 3, the circular jets gives 0.58 to 2% higher heat transfer coefficient at the lower flowrate, but at the flowrates of 0.006 and 0.007 m^3/s, the cusped ellipse jets give 0.3 and 1.8% higher heat transfer coefficient, which are within the uncertainty of the experiment. At the jet-to-plate spacing of 4, the heat transfer coefficient for the circular jets is between 0.44 and 5% higher than the cusped ellipse. This is within the range of uncertainty for these data. At 0.007 m^3/s, the heat transfer from cusped ellipse is 6% higher.

Local Nusselt Number

Figure 5.10 shows the surface plot of the Nusselt number versus the x and y pixel count for the circular jet array at Reynolds number of 7005 and the H/D_h of 2. Negative x is the streamwise direction and y is the spanwise direction. Figure 5.11 shows the surface plot for the cusped ellipse jet array at Reynolds number of 6235 and H/D_h of 2. Both figures are at the same flow rate. Each single peak in the surface plots represents a location underneath each jet. Each peak is neither smooth nor symmetric. This could be explained that there are secondary peaks, according to Viskanta (14), but the effect of the crossflow wipes out some of those peaks. To

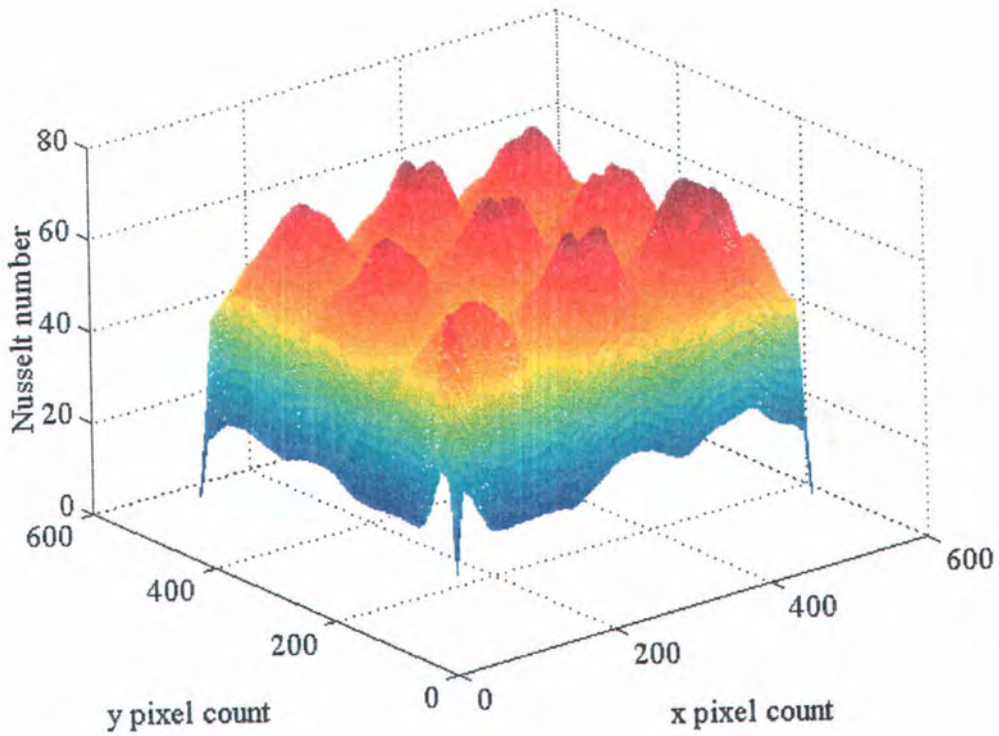

Figure 5.10. Three-Dimensional Plot, Circular, Re = 7005, $H/D_h = 2$

x is the streamwise direction and y is the spanwise direction

Flow is in the negative x direction

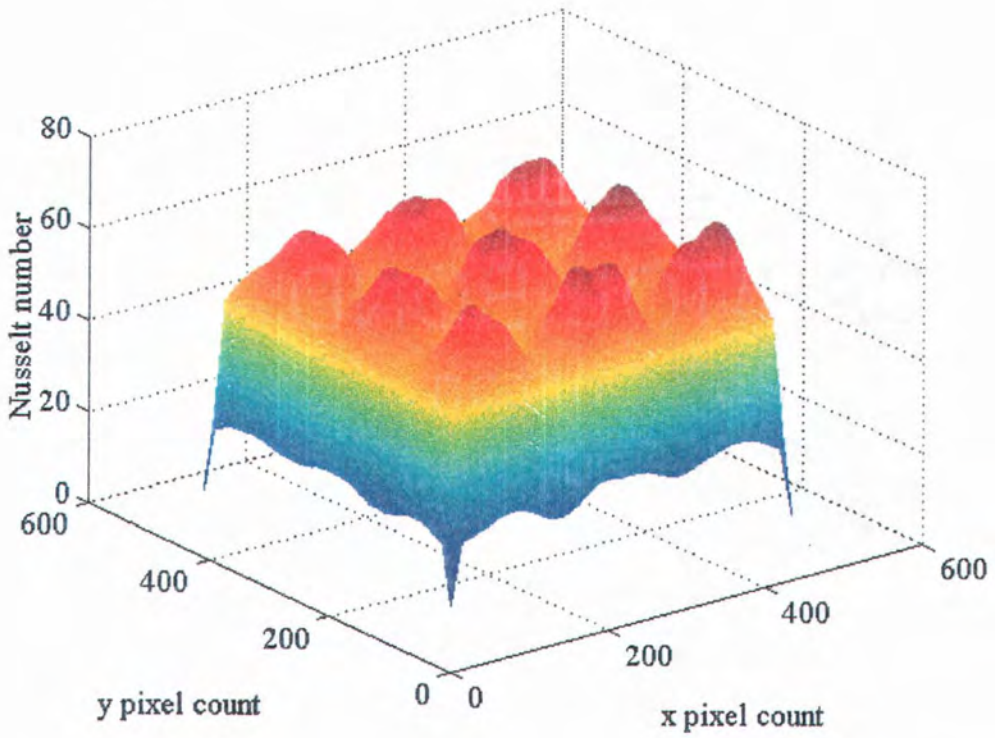

Figure 5.11. Three-Dimensional Plot, Cusped Ellipse, Re = 6235, $H/D_h = 2$

better see the local variation, slice plots are used which are taken through the center row in the streamwise and spanwise directions of the surface plots.

Figures 5.12 and 5.13 represent the slice plot for the surface plot in Figure 5.10 taken through the center rows in the streamwise and spanwise directions, respectively, at a Reynolds number of 7005. Figures 5.14 and 5.15 are slice plots for Figure 5.11 in the streamwise and spanwise directions, respectively, as well. The airflow is in the negative x direction. Here, crossflow is complete, or the maximum, according to Obot and Trabold (8), which means that the air was forced to exit in one direction and the other three sides were closed. Consider Figures 5.12 and 5.14, the streamwise cross sectional slices shows that the upstream peak has the highest maxima, the middle peak is the second highest, and the downstream location has the lowest peak. Figures 5.13 and 5.15 show the spanwise cross sectional slices. All peaks for each geometry tend to be consistent. Since all of the flow was in the streamwise direction, because of symmetry and no variation in the spanwise direction, is expected.

Figures 5.12 to 5.15 were taken at the same flowrate, 0.0049 m^3/s. Since both geometries do not give exactly the same Reynolds number value at the same flowrate, the Nusselt number distributions of both geometries cannot be compared quantitatively on the same axes. It is, therefore, more informative to compare the results of both geometries in the form of heat transfer coefficient as in Figures 5.16 to 5.19.

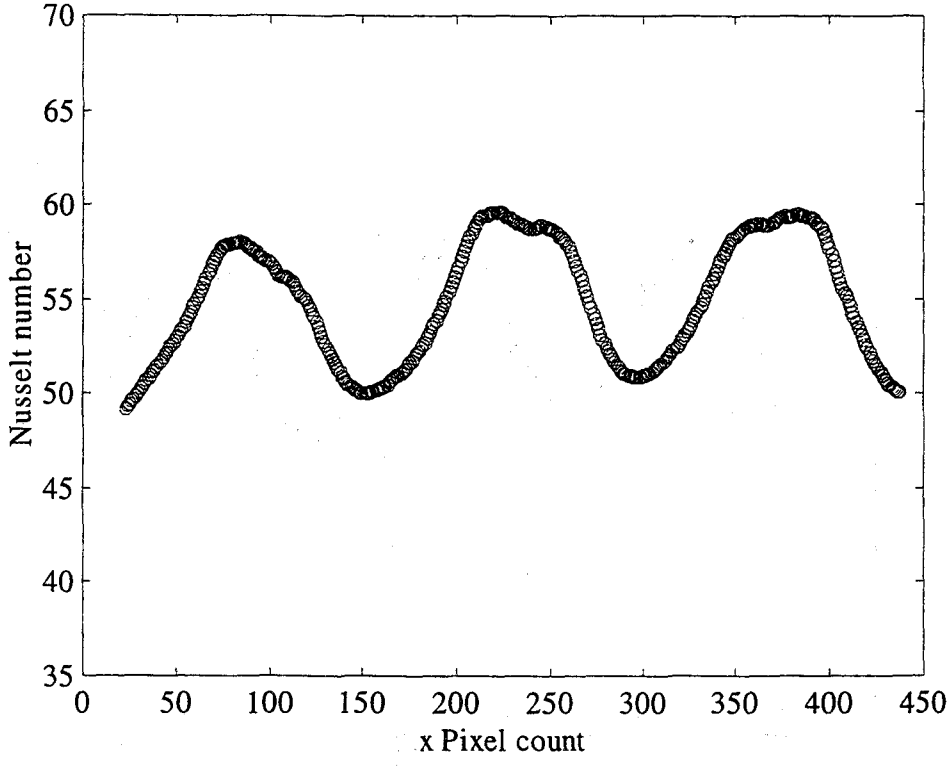

Figure 5.12. Center Cross Section (x slice), Circular, Re = 7005, $H/D_h = 2$

Crossflow is in the negative x direction.

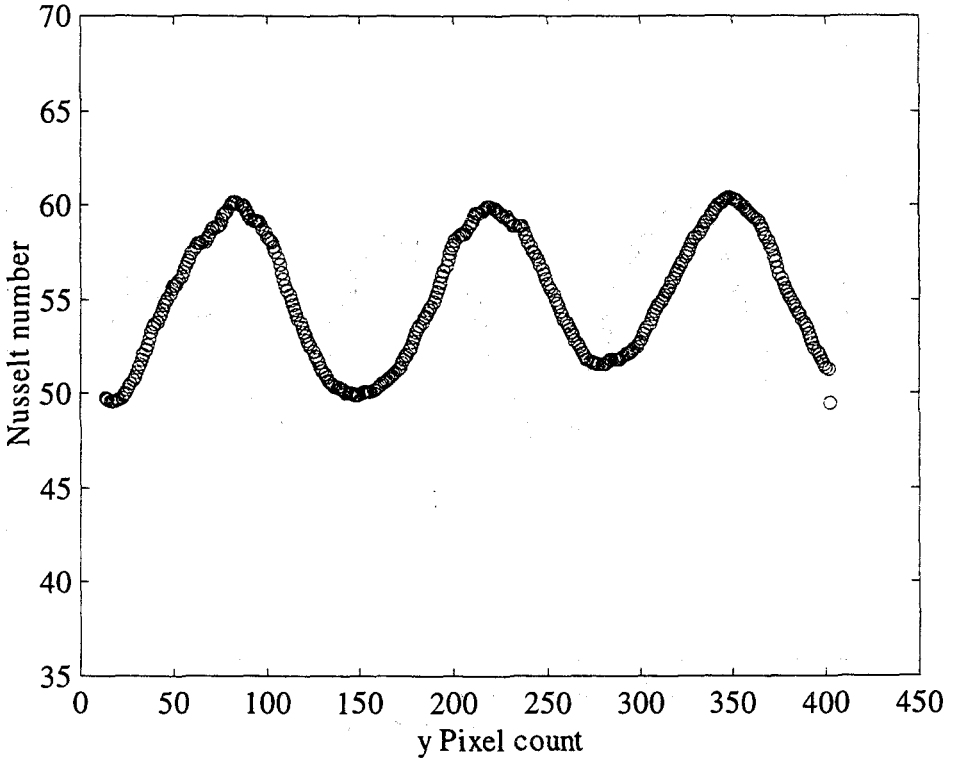

Figure 5.13. Center Cross Section (y slice), Circular, Re = 7005, $H/D_h = 2$

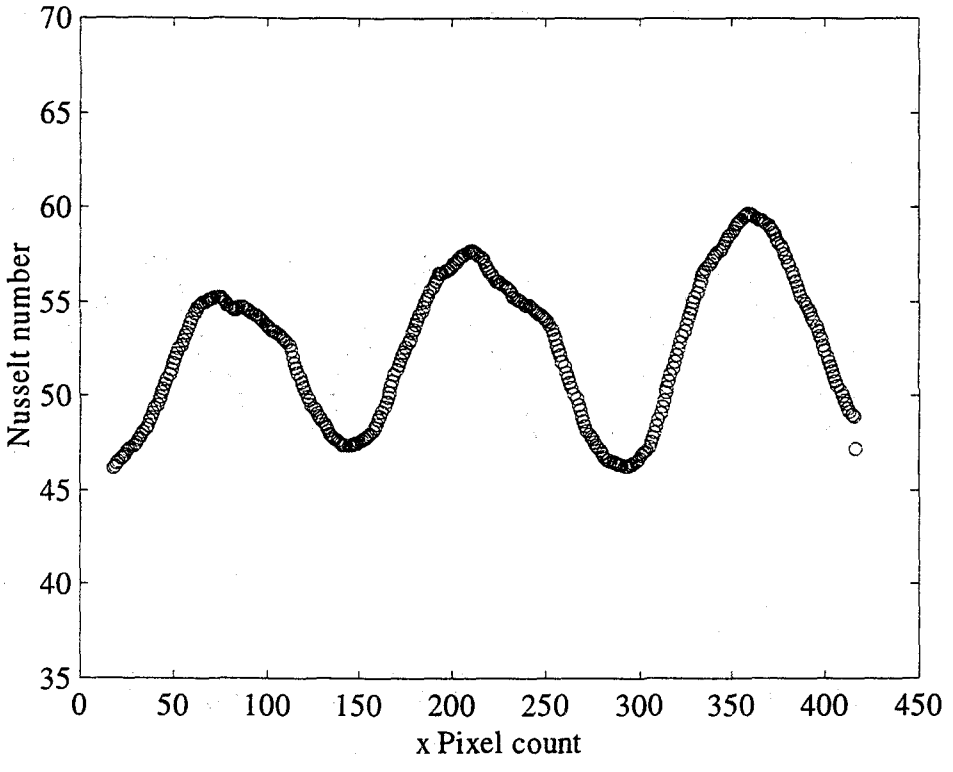

Figure 5.14. Center Cross Section (x slice), Cusped Ellipse, Re = 6235, $H/D_h = 2$

Crossflow is in the negative x direction.

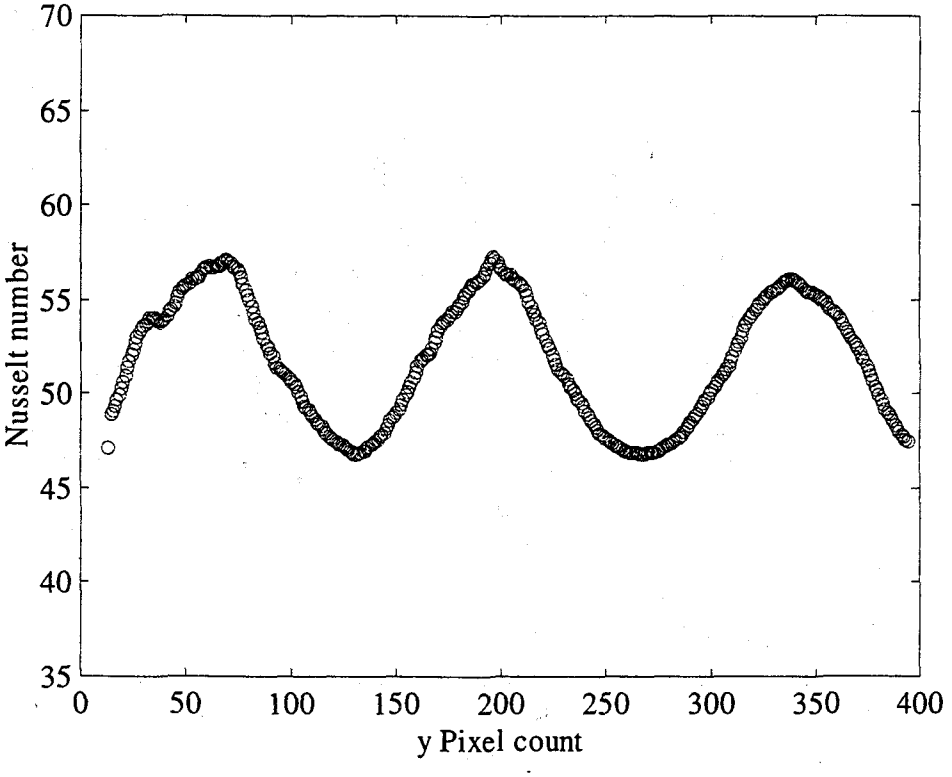

Figure 5.15. Center Cross Section (y slice), Cusped Ellipse, Re = 6235, $H/D_h = 2$

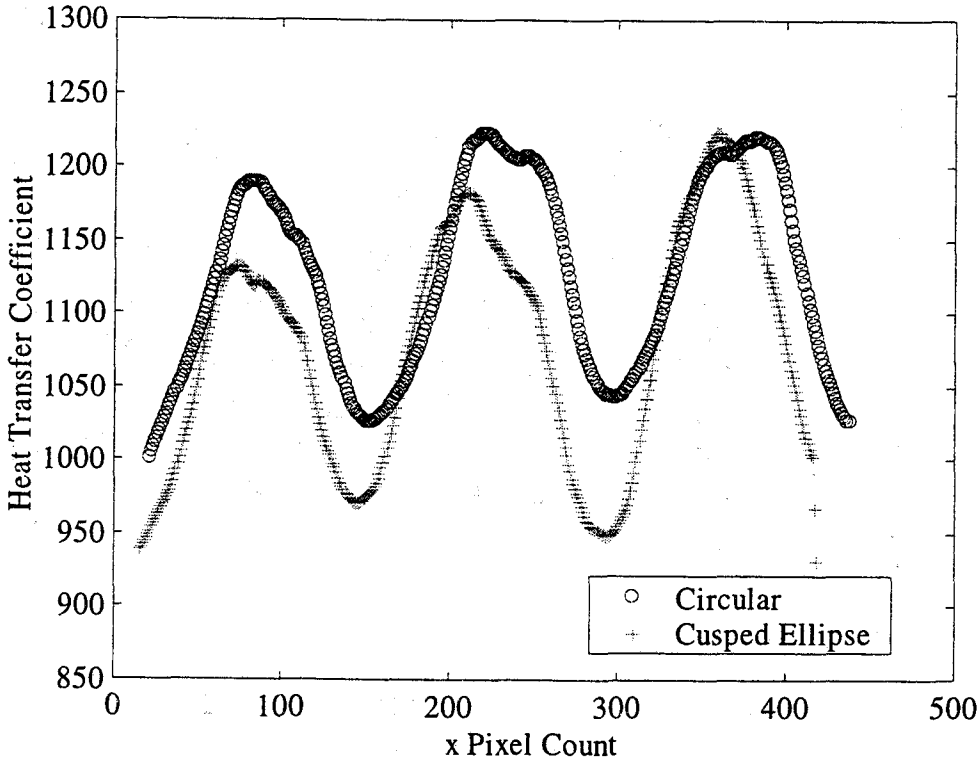

Figure 5.16. Center Cross Section (x slice), Flowrate 0.0049 m^3/s, $H/D_h = 2$

Crossflow is in the negative x direction.

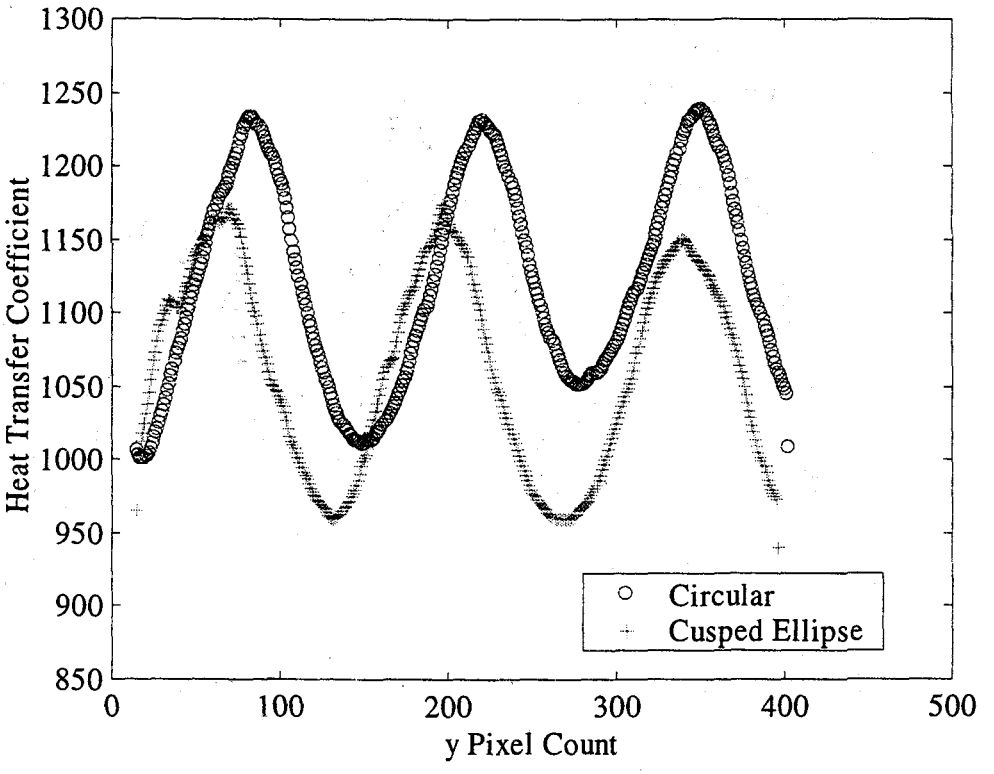

Figure 5.17. Center Cross Section (y slice), Flowrate 0.0049 m^3/s, $H/D_h = 2$

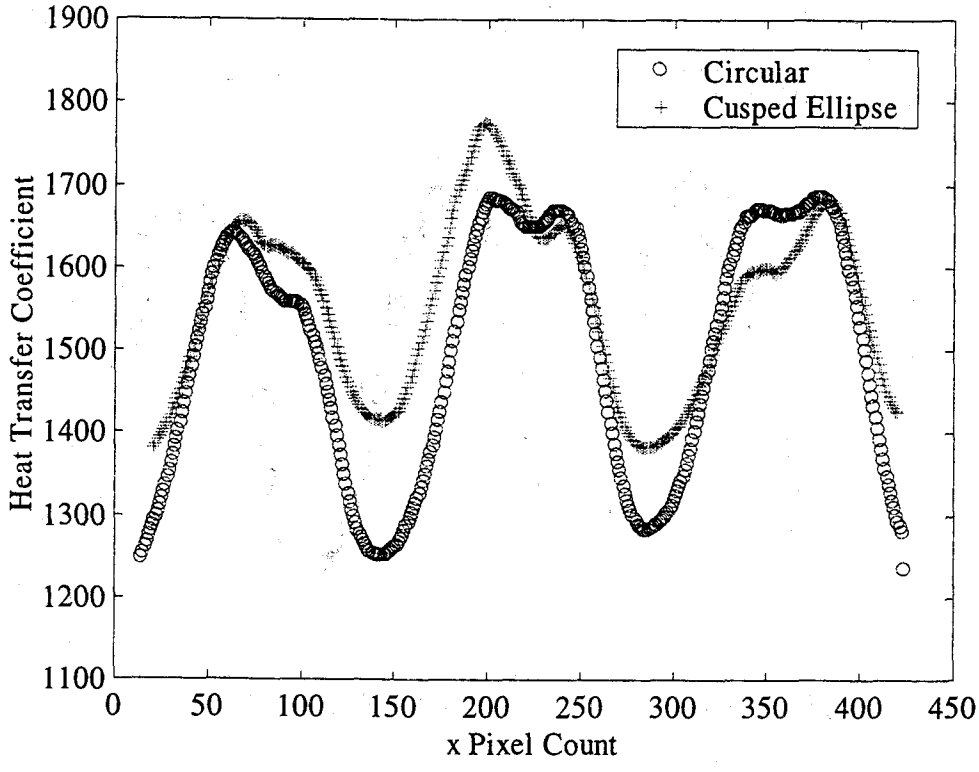

Figure 5.18. Center Cross Section (x slice), Flowrate 0.0072 m^3/s, $H/D_h = 2$, Crossflow is in the negative x direction.

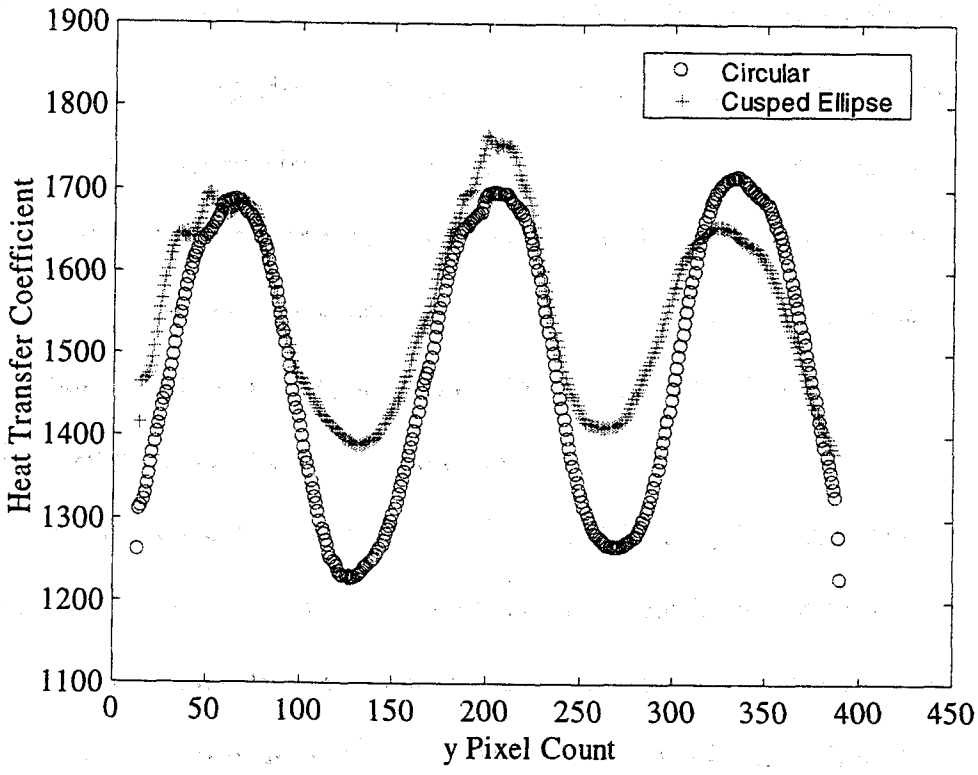

Figure 5.19. Center Cross Section (y slice), Flowrate 0.007 m^3/s, $H/D_h = 2$

Figures 5.16 and 5.17 represent the comparison of the local heat transfer distributions along the streamwise and spanwise directions, respectively, for both geometries at the flow rate of 0.0049 m^3/s and H/D_h of 2. The maxima and the minima peaks for the circular jet array are higher than those for the cusped ellipse jet array. Recalling the comparison of the average heat transfer coefficient, at this flowrate, the circular jets give a better performance than the cusped ellipse jets. The local results agree well with the average result. For the local heat transfer distribution, the heat transfer coefficients for the circular jets drop between 14 and 17% from maximum to minimum, and those for the cusped ellipse jets drop between 15 and 26% from maximum to minimum.

At the higher flowrate, such as 0.0072 m^3/s, and H/D_h of 2, the peaks for the cusped ellipse jets are slightly higher than the peaks for the circular jets as shown in Figures 5.18 and 5.19. But, the minimum peaks for the cusped ellipse jets are approximately 100-200 W/m^2 K higher than those for the circular jets. From the local distribution at this condition, the cusped ellipse jets give better performance than the circular jets. The heat transfer coefficients for the cusped ellipse jets drop from 15 to 22% from maximum to minimum, while those for the circular jets drop from 23 to 26%.

Figure 5.20 shows the plot of the average root mean square values of the heat transfer coefficient over all Reynolds number versus H/D_h. For the circular jets, the average value of the root mean square values for all Reynolds number at each H/D_h are 0.1862 for H/D_h of 1, 0.1636 for H/D_h of 2, 0.1600 for H/D_h of 3,

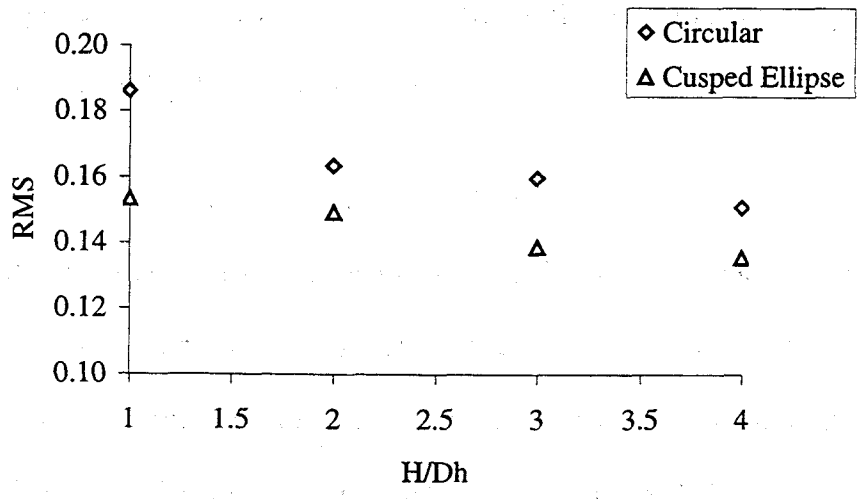

Figure 5.20. Average Normalized Root Mean Square of heat transfer coefficient vs. H/D_h

and 0.1511 for H/D_h of 4. For the cusped ellipse jets, the average root mean values for H/D_h of 1, 2, 3 and 4 are 0.1535, 0.1494, 0.1390, and 0.1357, respectively. The heat transfer distributions are more uniform as H/D_h increases. The root mean square value for the cusped ellipse jets is 10 to 21% lower than the root mean square for the circular jets. This means that local heat transfer coefficients for the cusped ellipse jets fluctuate from the mean value less than those for the circular jets. The cusped ellipse jets give a better uniformity of the heat transfer compared to the circular jets for each jet-to-plate spacing.

Comparison to Literature

The paper by Schroeder and Garimella (14) is first used for comparison of the average Nusselt number for a uniform heat flux impingement surface for circular jets. The comparison is shown in Figure 5.21. The result of the current study is essentially no different from the result of Schroeder and Garimella (14). The difference is in the range of 0.02 to 8.40%. Reasons for these differences include that Schroeder and Garimella (14) used a jet-jet spacing of 4 diameters while the current study has a jet-jet spacing of 6.25 diameters. A second possible reason is the size of the jet. Schroeder and Garimella (14) employed a jet diameter of 1.59 mm, while the present study used the jet diameter of 1.27 mm. For the local heat transfer coefficient distribution, the shape of the plot for the current study was similar to that for Schroeder and Garimella (14).

The second study used to compare with the present study is that of Huber and Viskanta (15). The current study is 26 to 36% higher than that of Huber and

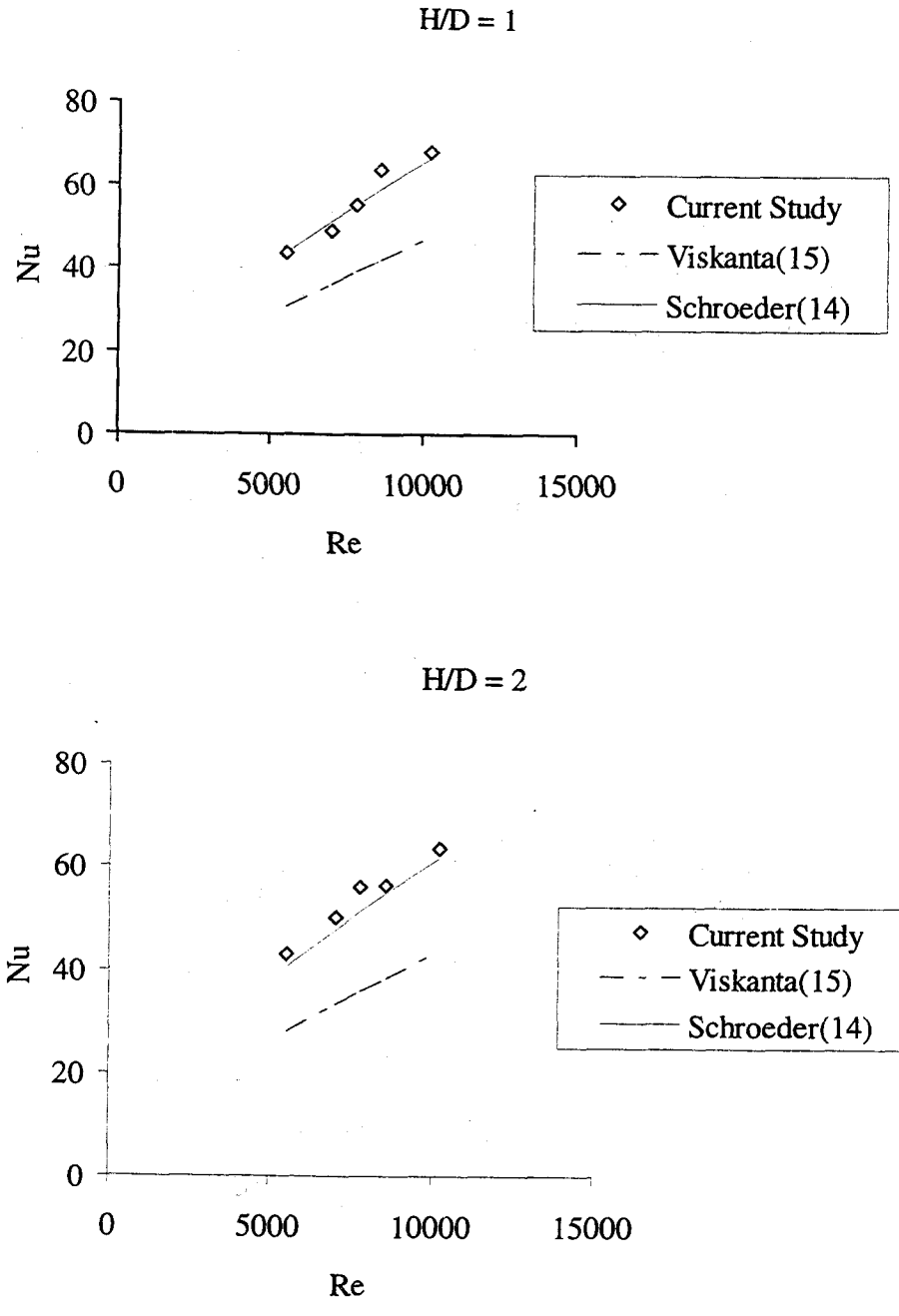

Figure 5.21(a). Comparison to Literature, Uniform Heat Flux, Circular Jets

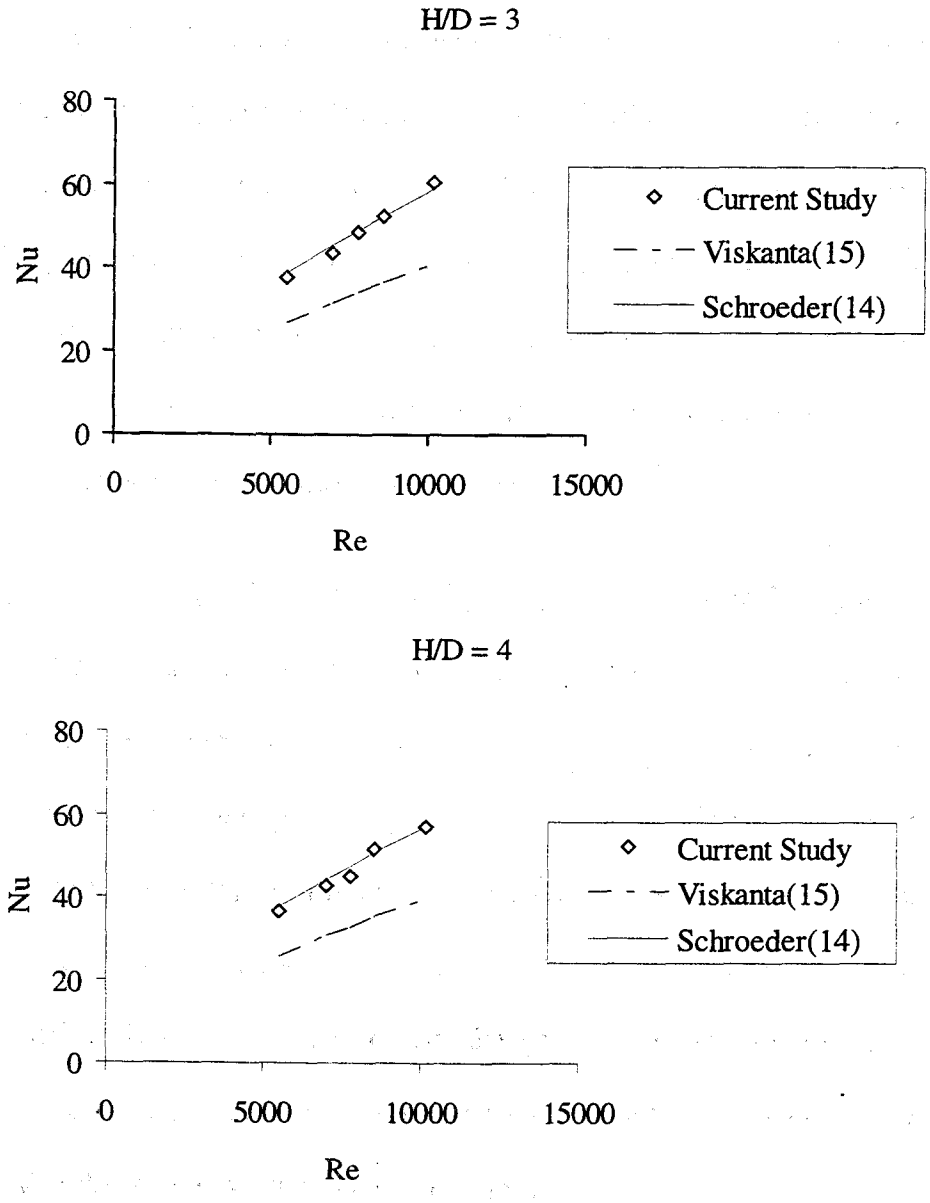

Figure 5.21(b). Comparison to Literature, Uniform Heat Flux, Circular Jets

Viskanta (15). The very significant reason for this has to be that in the study of Huber and Viskanta (15) the diameter of the jet used was 5 times of the size of the jet used in the current study. For the local heat transfer distribution, the plot of the present study has a similar shape to the study of Huber and Viskanta (15) in that there were the presence of secondary peaks. Huber and Viskanta (15) explained that these secondary peaks increased the average heat transfer coefficient, and the maximum was not at the stagnation points, but at the secondary peaks. In the present study, these peaks are distorted by the jet crossflow.

Comparison of Average Nusselt Numbers for Both Surface Boundary Conditions

Figure 5.22 shows the comparison of the average Nusselt numbers of the circular jets for the isothermal impingement surface and the uniform heat flux impingement surface. For every jet-to-plate spacing, the uniform heat flux impingement surface gives higher average Nusselt numbers than the isothermal impingement surface. The average Nusselt number from the uniform heat flux impingement surface is more sensitive to the change of Reynolds number. The uniform heat flux impingement surface gives an average Nusselt number 22 to 37% higher than that of the isothermal impingement surface.

The comparison for the cusped ellipse jets is shown in Figure 5.23. Similar to the comparison for the circular jets above, the uniform heat flux impingement surface gives a higher average Nusselt number than the isothermal impingement surface for every H/D_h value. The average Nusselt number for the uniform heat flux impingement surface is more sensitive to the change of the Reynolds number value.

The difference between the Nusselt number for the two boundary conditions is in the range of 29 to 46%.

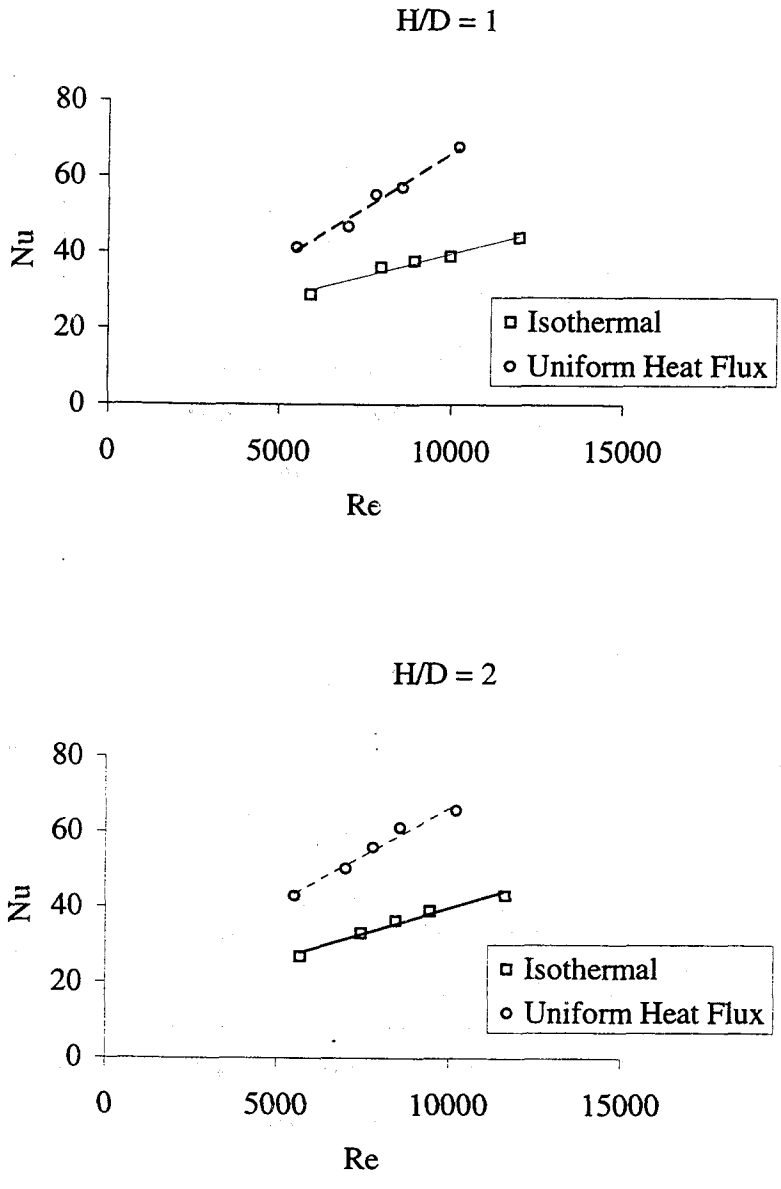

Figure 5.22(a). Comparison between both Surface Boundaries Conditions, Circular Jets

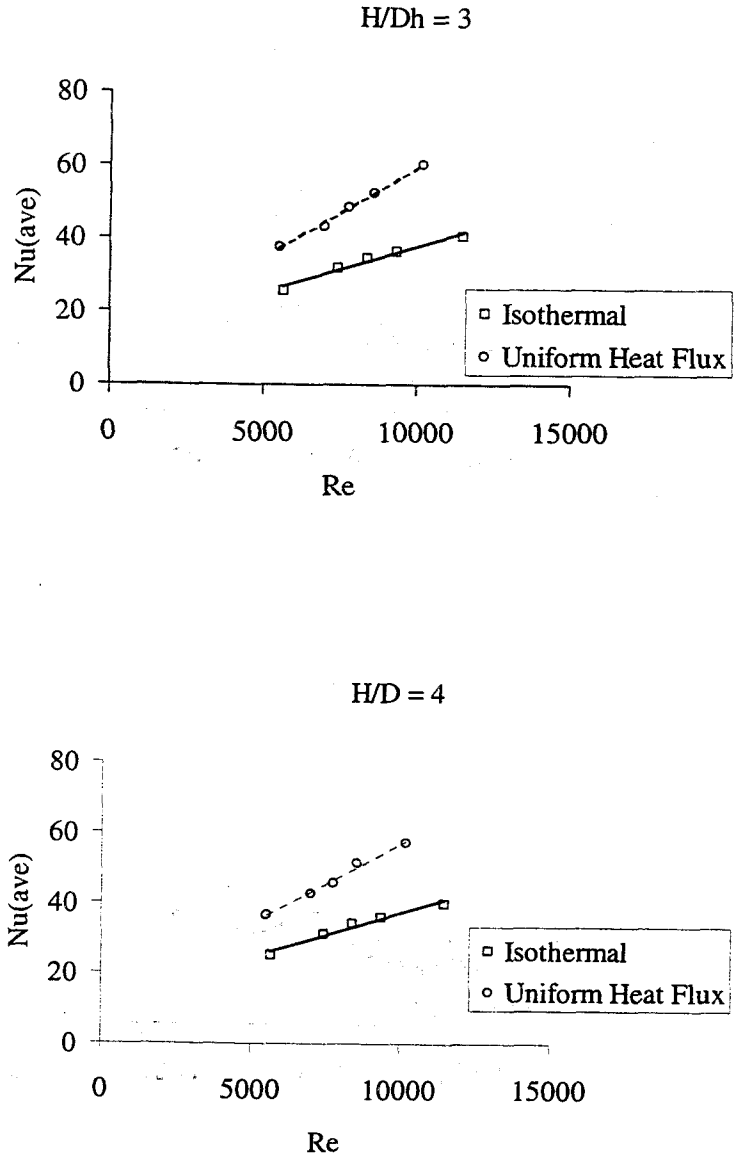

Figure 5.22(b). Comparison between both Surface Boundaries Conditions, Circular Jets

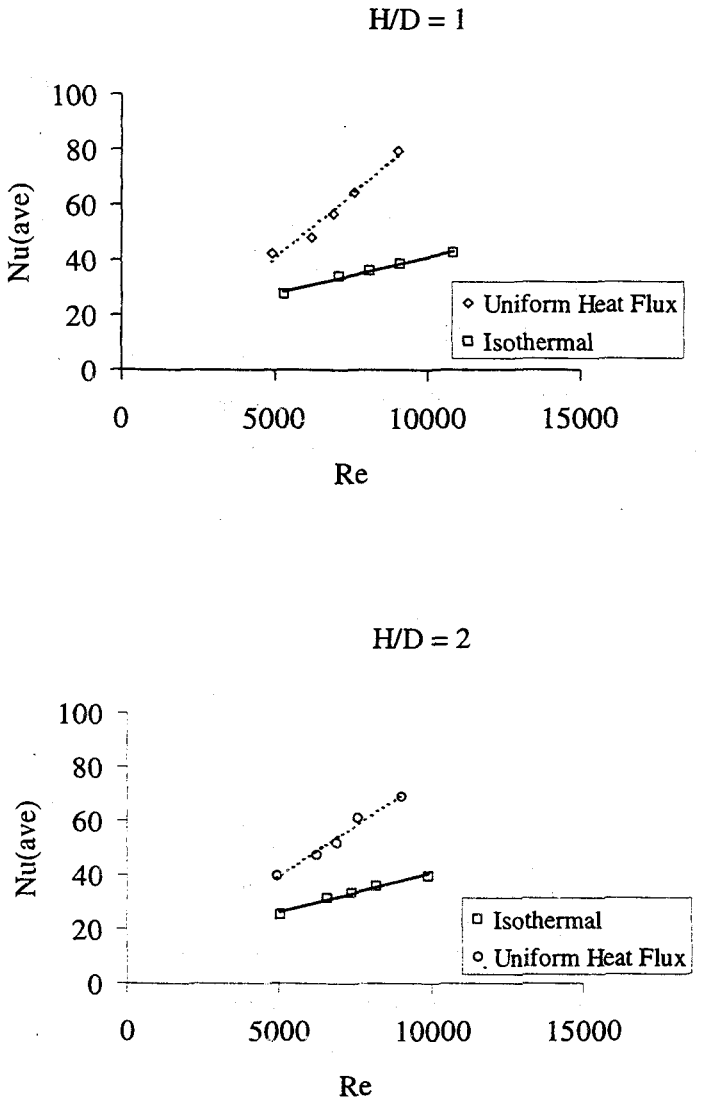

Figure 5.23(a). Comparison between both Surface Boundary Conditions,

Cusped Ellipse Jets

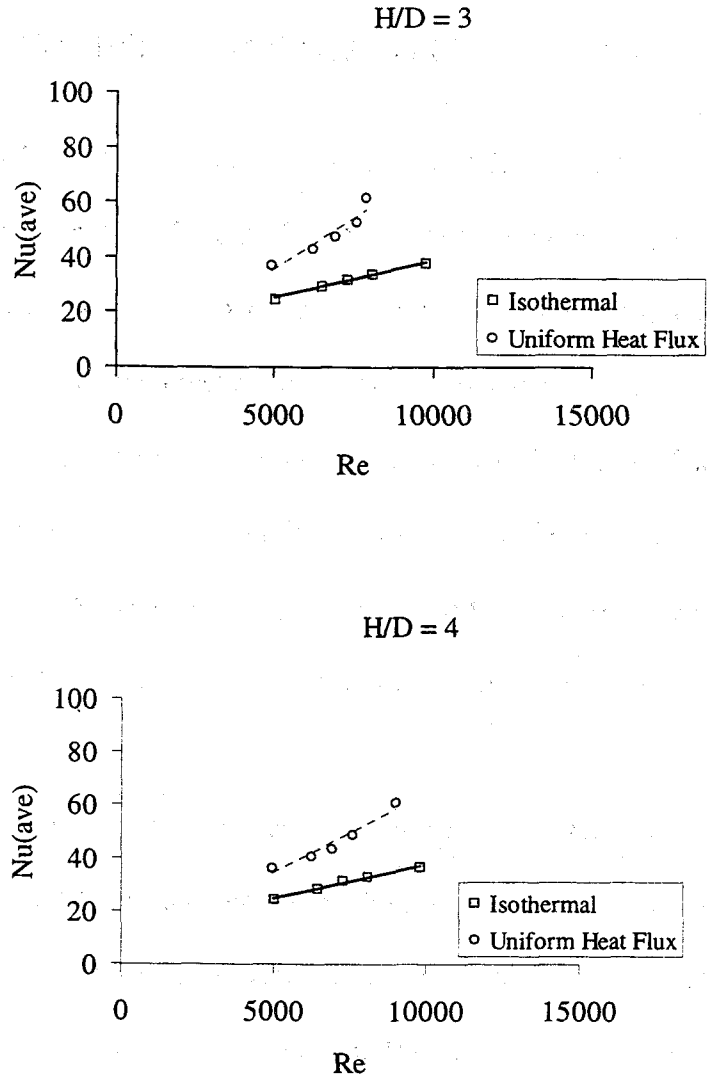

Figure 5.23(b). Comparison between both Surface Boundary Conditions,

Cusped Ellipse Jets

CHAPTER VI

CONCLUSIONS AND RECOMMENDATIONS

The goals for this study are to evaluate the effect of the nozzle geometry, and to investigate the effect of the surface boundary condition on jet impingement heat transfer with crossflow. Both nozzle geometries: circular and cusped ellipse jets, have the same cross sectional areas. For both boundary conditions, the cusped ellipse jets tended to give better heat transfer performance based on Nusselt number versus Reynolds number. The variable parameters in the experiment were the volume flow rate, and the jet-to-plate spacing. Overall, a decrease in the jet-to-plate spacing and an increase of the volume flow rate results in an increase of the heat transfer coefficient.

For the isothermal surface boundary condition, the cusped ellipse jets give a higher average Nusselt number, based on hydraulic diameter for all Reynolds numbers. The average Nusselt number for the cusped ellipse jet array is more sensitive to the change of Reynolds number than that for the circular jet array. Based on the volume flow rate, however, the circular jet array gives a higher heat transfer coefficient at the same flow rate. The sensitivity to the change the volume flow rate of the heat transfer coefficient from both geometries were similar.

For the uniform heat flux surface boundary condition, considering the average heat transfer distribution, the cusped ellipse jets show higher average Nusselt number, and have more sensitivity to the change of the Reynolds number. Based on the volume flow rate, there are crossovers in every jet-to-plate spacing.

At the lower flow rate, the circular jets tended to have the higher heat transfer coefficient. At the higher flow rate, the cusped ellipse tends to give the higher heat transfer coefficient. The crossovers are obvious for the jet-to-plate spacings of 1 and 2, but not for the jet-to-plate spacings of 3 and 4.

For the local heat transfer coefficient, distributions over the surface for both geometries are similar. Peaks decrease along the streamwise direction. This is caused by the crossflow and mixing of adjacent jets. Therefore, the farther jet from the exhaust results in the higher peak. At the lower flow rate, the circular jets give the higher peaks of both maxima and minima. However, at the higher flow rate, the cusped ellipse jets give the higher peaks both maxima and minima. For every flow rate, the cusped ellipse jets had the more uniform heat transfer distribution.

Comparing the two surface boundary conditions, the uniform heat flux impingement surface had the higher Nusselt numbers than the isothermal impingement surface. This is speculated to be a result of different temperature profiles dependent on the surface boundary conditions. Further study is recommended to fully understand this difference.

To enhance the heat transfer performance, the follows are recommended. The higher flow rate and small jet-to-plate spacing will cause more turbulence. In order to reduce the jet interference, I would recommend the spent air exit, and increase jet-jet spacing. In terms of geometry of the orifice plate, since the cusped sections can cause more turbulence, and the higher heat transfer distribution can be achieved, I would like to recommend "club" or Mickey Mouse shape.

BIBLIOGRAPHY

1. Metzger, D.E., "Heat Transfer in Gas Turbine Engines," Winter Annual Meeting of The American Society of Mechnical Engineers, Boston, Massachusettes, Vol. 87, December 13-18, 1987.

2. Behbahani, A. I., Goldstein, R. G., "Impingement of a Circular Jet With and Without Crossflow," Int. J. Heat Mass Transfer, Vol. 25, No. 9, pp. 1977-1982, 1982.

3. Kercher, D.M., Tabakoff, W., "Heat Transfer by a Square Array of Round Air Jets Impinging Perpendicular to a Flat Surface Including the Effect of Spent Air," Journal of Engineering for Power, January 1970, pp. 73-82.

4. Hrycak, P., "Heat Transfer from Round Impinging Jets to a Flat Plate," Heat Mass Transfer, Vol. 26, No. 12, pp. 1857-1865, 1983.

5. Hamahah, T. T., " Impingement Cooling of a Simulated Electronic Package with a Square Array of Round Air Jets," 1989 National Heat Transfer Conference, pp. 107-112, 1989.

6. Florschuetz, L. W., Su, C. C., "Effects of Crossflow Temperature on Heat Transfer Within an Array of Impinging Jets," Transaction of ASME, Vol. 109, Feb. 1987, pp. 74-82.

7. Obot, N. T., Trabold, T. A., "Impingement Heat Transfer Within Arrays of Circular Jets: Part 1- Effects of Minimum, Intermediate, and Complete Crossflow for Small and Large Spacings," Transaction of the ASME, Vol. 109, November 1987, pp. 872-879.

8. Florschuetz, L.W., Truman, C.R., Metzger, D.E., "Streamwise Flow and Heat Transfer Distribution for Jet Array of Impinging Jets," Journal of Turbomachinery, Vol. 103, July 1981, pp. 337-342.

9. Baugh, J.W., Shimizu, S., "Heat Transfer Measurement from a Surface With Uniform Heat flux and an Impinging Jet," Transaction of ASME, Journal of Heat Transfer, Vol. 111, pp. 1096-1098, 1989.

10. San, J.Y., Huang, C.H., Shu, M.H., "Impingement Cooling of a Confined Circular Air Jet," Int. J. Heat Mass Transfer, Vol. 40, No. 6, pp. 1355-1364, 1997

11. El-Genk, M.S., Huang, L., Guo, Z., "Heat Transfer Between a Square Flat Plate

and a Perpendicularly Impinging Circular Air Jet," HTD-Vol. 202, Enhanced Heat Transfer, ASME 1992, pp. 33-38.

12. Lee, S.J., Lee, J.H., Lee, D.H., "Local Heat Transfer Measurements from an Elliptic Jet Impinging on a Flat Plate Using Liquid Crystal," Int. J. Heat Mass Transfer, Vol. 37, No. 6, pp. 967-976, 1994.

13. Goldstein, R.J., Franchett, M.E., "Heat Transfer from a Flat Surface to an Oblique Impinging Jet," Transaction of ASME, Journal of Heat Transfer, Vol. 110, pp. 84-90, 1988.

14. Schroeder, V.P., Garimella, S.V., "Heat Transfer in the Confined Impingement of Multiple Air Jets," HTD-Vol. 361-1, Proceeding of the ASME Heat Transfer Division, Vol. 1, 1998.

15. Huber, A. M., Viskanta, R., "Effect of Jet-Jet Spacing on Convective Heat Transfer to Confined, Impinging Arrays of Axisymmetric Air Jets," Int. J. Heat Mass Transfer, Vol. 37, No. 18, pp. 2859-2869, 1994

16. Fergason, J.L., "Liquid Crystal," Scientific American, Vol. 211, No. 2, Aug. 1964, pp. 76-85.

17. Parsley, M., "The Use of Thermochromic Crystal in Heat Transfer and Flow Visualization Research," 2nd International Symposium on Fluid Visualization, 1998.

18. Hallcrest, Inc., "The Use of Thermochromic Liquid Crystals and their Products and Research Tools," Paper, Jan. 1996.

19. Hippensteele, S. A., Russell, L. M., Stepka, F. S., "Evaluation of a Method for Heat Transfer Measurements and Thermal Visualization Using a Composite of Heater Element and Liquid Crystals," Transaction of ASME, Vol. 105, Feb. 1983, pp. 184-189.

20. Hippensteele, S. A., Russell, L. M., Torres, F. J., "Local Heat Transfer Measurement on a Large-Scale Model Turbine Blade Airfoil Using a Composite of a Heater Element and Liquid Crystal," Journal for Engineering for Gas Turbines and Power, Vol. 107, Oct. 85, pp. 953-60.

21. Simonich, J.C., Moffat, R.J., "New Technique for Mapping Heat Transfer Coefficient Contours," NASA Contractor Report, 1994.

22. Camci, C., Kim, K., Hippensteele, S. A., "A New Hue Capturing Technique for the Quantitative Interpretation of Liquid Crystal Images Used in Convective

Heat Transfer Studies," Journal of Turbomachinery, Vol.114, October 1992, pp. 765-775.

23. Hippensteele, S. A., Russell, L. M., Stepka, F. S., "Evaluation of a Method for Heat Transfer Measurements and Thermal Visualization Using a Composite of a Heater Element and Liquid Crystal," Transaction of the ASME, Vol. 105, February 1983, pp. 184-189.

24. Wang, Z., Ireland, P.T., Jones, T.V., "An Advanced Method of Processing Liquid Crystal Video Signals from Transient Heat Transfer Experiments," ASME Paper No. 93-GT-282, 1993.

25. Wang, Z., Ireland, P.T., Jones, T.V., Davenport, R., "A Colour Image Processing System for Transient Liquid Crystal Heat Transfer Experiments," ASME Paper No. 94-GT-290, 1994.

26. Florschuetz, L.W., Truman, C.R., Metzger, D.E., "Streamwise Flow and Heat Transfer Distribution for Jet Array of Impinging Jets," Journal of Turbomachinery, Vol. 103, July 1981, pp. 337-342.

27. Owens, R., "Effect of Jet Array Nozzle Geometry on Impingement Heat Transfer," Thesis, Clemson University, May 1995.

28. Venkatachalapathi, S., "Effect of Surface Ribs on Impingement Heat Transfer," Thesis, Clemson University, August 1998.

28. Arjocu, S.C., Liburdy, J.A., Ferland, M.M., "Effects of Orifice Geometry on the Heat Transfer Distribution for Impinging Jet Array," Proceedings of the ASME Heat Transfer Division, Vol. 3, 1997, pp. 47-54.

29. Van Treuren, K.W., Wang, Z., Ireland, P.T., Jones, T.V., "Detailed Measurements of Local Heat Transfer Coefficient and Adiabatic Wall Temperature Beneath an Array of Impinging Jets," Transaction of ASME, Journal of Turbomachinery, July 1994, Vol. 116, pp. 369-374.

31. Moffat, R.M., "Using Uncertainty Analysis in the Planning of an Experiment," Journal of Fluid Engineering, Vol. 107, June 1985, pp. 173-178.

32. Moffat, R.M., "Describing the Uncertainties in Experimental Results," Experimental Thermal and Fluid Science, 1988, pp. 3-17.

APPENDICES

APPENDIX A

UNCERTAINTY ANALYSIS

This appendix is presented to determine the uncertainties of the dependent and independent variables. The uncertainties of mass flow rate, Reynolds number, heat flux, temperature measurements such as thermocouples and liquid crystals, heat transfer coefficient, and Nusselt number are discussed here.

Volume Flow Rate

According to the correction formula of the readout flow rate from the manufacturer of the flow meter used in this experimentation, the actual flow rate is, therefore, a product of the readout flow rate and the pressure correction factor:

$$Q_{actual} = Q_{Readout} \times CF \tag{A.1}$$

Where CF is the correction factor, which is equal to $\sqrt{\frac{14.7+P}{14.7}}$, psi

However, the value of pressure can be read from the data logger in mV, and calculated in psi according to the manufacturer of the pressure transducer as follows

$$P = \frac{mV}{3.032} \tag{A.2}$$

Therefore, the correction factor becomes

$$CF = \sqrt{1+\frac{mV}{44.5704}} \tag{A.3}$$

The uncertainty for the volume flow rate, thus, is estimated from the Kline-McClintock relation as follows

$$u_{Q_{Actual}} = \sqrt{\left(\frac{\partial Q_{Actual}}{\partial Q_{Readout}} u_{Q_{Readout}}\right)^2 + \left(\frac{\partial Q_{Actual}}{\partial CF} u_{CF}\right)^2} \tag{A.4}$$

The uncertainty for the readout flow rate is obtained from the scale of the flow meter, which is ±0.5 cfm. The flow meter was calibrated by the manufacturer with an error of 4% of full scale. The uncertainty for the correction factor, which is related to the pressure read from the pressure transducer as indicating above, is ±0.005 mV. The uncertainty for the actual flow rate ranges from 5.38 to 7.43%.

Reynolds number

The uncertainty of the impingement Reynolds number is a function of

$$u_{\mathrm{Re}} = f(u_Q, u_{D_h}, u_\nu) \tag{A.5}$$

The uncertainty of the mass flow rate has already been determined in the previous section. The uncertainty of the jet diameter is ±0.0005 m. The uncertainty of the viscosity, which was taken as the fluctuation within the temperature range of 20 to 27°C, is ±0.000000335 m^2/s. The uncertainty of Re is, thus, found from

$$u_{\mathrm{Re}} = \sqrt{\left(\frac{\partial \mathrm{Re}}{\partial Q} u_Q\right)^2 + \left(\frac{\partial \mathrm{Re}}{\partial D_h} u_{D_h}\right)^2 + \left(\frac{\partial \mathrm{Re}}{\partial \nu} u_\nu\right)^2} \tag{A.6}$$

Finally, the uncertainties for the Reynolds number ranges from 7.05 to 8.72%.

Heat Flux

In the case of isothermal impingement surface, the heat flux is calculated from the voltage drop across the heater, the resistance of the packaged heater, and the area of the heater

$$u_{q",isothermal} = f(u_{Voltage}, u_{Resistance}, u_{Area}) \tag{A.7}$$

The uncertainty of the voltage is the resolution that the voltmeter can read, which is ±0.05 Volt. The uncertainty of the resistance that is read by the multimeter is ±0.05 ohm. And the uncertainty of the area is found form the following relation:

$$u_{Area} = \sqrt{\left(\frac{\partial Area}{\partial Length} u_{Length}\right)^2 + \left(\frac{\partial Area}{\partial Width} u_{Width}\right)^2} \tag{A.8}$$

The uncertainty of the length and width is ±0.0005 m, and the uncertainty of the area is then ±0.0000462 m^2 or 1.13%. Finally, the uncertainty of the heat flux in this case can be determined by

$$u_{q"} = \sqrt{\left(\frac{\partial q"}{\partial Voltage} u_{Voltage}\right)^2 + \left(\frac{\partial q"}{\partial R} u_R\right)^2 + \left(\frac{\partial q"}{\partial Area} u_{Area}\right)^2} \tag{A.9}$$

The uncertainties of the heat flux ranges from 0.5458 to 0.6132% for both geometries.

In the uniform heat flux surface case, the heat flux is calculated from the voltage across the foil, the current through the foil, and the area of the foil

$$u_{q",uniform} = f(u_{Voltage}, u_{Current}, u_{Area}) \tag{A.10}$$

The uncertainty for the voltage is ±0.005 Volt. The uncertainty for the surface area is ±0.000000396 m^2. The uncertainty of the current can be determined by the

resolution of the ampmeter that reads out the current, which is ±0.0005 amp. Eventually, the uncertainty of the heat flux can be found from the following equation:

$$u_{q''} = \sqrt{\left(\frac{\partial q''}{\partial Voltage} u_{Voltage}\right)^2 + \left(\frac{\partial q''}{\partial Current} u_{Current}\right)^2 + \left(\frac{\partial q''}{\partial Area} u_{Area}\right)^2} \qquad \text{(A.11)}$$

The uncertainties of the heat fluxes are 1.17 to 1.34% at the lowest and highest extremes.

Temperature Measurements (Thermocouples)

Thermocouples used here were J type. In the calibration of the thermocouples, the temperature was measured by using a glass thermometer, and the Fluke data logger. The uncertainty for thermocouples is, thus, a function of the uncertainties from the glass thermometer and the data logger.

$$u_{T_{TC}} = f(u_{T_{gl}}, u_{T_{DL}}) \qquad \text{(A.12)}$$

The uncertainty of the temperature from the glass thermometer is obtained from the resolution of the thermometer itself, which is ±0.1°C. Similarly, the uncertainty due to resolution from the data logger is ±0.05°C. The uncertainty to find the uncertainty of these temperature measurements is

$$u_{T_{TC}} = \sqrt{\left(\frac{\partial T_{TC}}{\partial T_{TM}} u_{T_{TM}}\right)^2 + \left(\frac{\partial T_{TC}}{\partial T_{DL}} u_{T_{DL}}\right)^2} \qquad \text{(A.13)}$$

The uncertainty in the thermocouples is ±0.11°C.

Temperature Measurements (Liquid Crystals)

To measure temperature of the heating surface in the case if the uniform heat flux impingement surface by using liquid crystals, the value of temperature measured by thermocouples and the hue values are taken into account. Therefore, the uncertainty for these temperatures depend on the uncertainties from temperatures measured by thermocouples, and the hue value

$$u_{T_{LC}} = f(u_{T_{TC}}, u_{Hue}) \tag{A.14}$$

The uncertainty of temperature measured by thermocouples is the pooled standard deviation of the values of those temperatures. The uncertainty of the average hue value is taken from the standard deviation of the average hue values for each calibration temperature.

$$u_{T_{LC}} = \sqrt{\left(\frac{\partial T_{LC}}{\partial T_{TC}} u_{T_{TC}}\right)^2 + \left(\frac{\partial T_{LC}}{\partial Hue} u_{Hue}\right)^2} \tag{A.15}$$

The uncertainty in liquid crystals used to measure the surface temperature is ±0.031°C.

Heat Transfer Coefficient

The uncertainty in the heat transfer coefficient for the isothermal impingement surface boundary condition is a function of the uncertainties in the heat flux, the surface temperature, and the jet temperature.

$$u_{\bar{h}} = f(u_{q''}, u_{T_s}, u_{T_j}) \tag{A.16}$$

The uncertainty in the heat transfer coefficient can be determined by the following equation:

$$u_{\bar{h}} = \sqrt{\left(\frac{\partial \bar{h}}{\partial q''} u_{q''}\right)^2 + \left(\frac{\partial \bar{h}}{\partial T_s} u_{T_s}\right)^2 + \left(\frac{\partial \bar{h}}{\partial T_j} u_{T_j}\right)^2} \qquad \text{(A.17)}$$

The uncertainty of the heat flux can be determined from the previous section. Both surface and jet temperatures were read out from the Fluke Data Logger, which has the resolution of 0.05°C. Thus, the uncertainty for the temperature from the previos section is ±0.11°C. Finally, the uncertainty for the heat transfer coefficient is found to be from 2.08 to 2.64% for the circular jet array, and from 2.07 to 2.55% for the cusped ellipse jet array.

For the uniform heat flux boundary condition, the heat transfer coefficient is a function of heat flux, which is obtained from the previous section, the surface temperature measured from the liquid crystal, and the jet temperature measured from thermocouple.

$$u_{\bar{h}} = f(u_{q''}, u_{T_{LC}}, u_{T_j}) \qquad \text{(A.18)}$$

The uncertainty is determined from the following equation

$$u_{\bar{h}} = \sqrt{\left(\frac{\partial \bar{h}}{\partial q''} u_{q''}\right)^2 + \left(\frac{\partial \bar{h}}{\partial T_s} u_{T_{LC}}\right)^2 + \left(\frac{\partial \bar{h}}{\partial T_j} u_{T_j}\right)^2} \qquad \text{(A.19)}$$

The uncertainty for the heat transfer coefficient for the uniform heat flux surface is found 1.78 to 4.05 % for the circular jet array, and 2.17 to 3.22 % for the cusped ellipse jet array.

Nusselt Number

The uncertainty in Nusselt number is a function of the heat transfer coefficient, the jet hydraulic diameter, and the thermal conductivity of air. Therefore, the uncertainty in Nusselt number is determined by the following equation

$$u_{Nu} = \sqrt{\left(\frac{\partial Nu}{\partial h} u_h\right)^2 + \left(\frac{\partial Nu}{\partial D_h} u_{D_h}\right)^2 + \left(\frac{\partial Nu}{\partial k} u_k\right)^2} \qquad \text{(A.20)}$$

In the case of the isothermal impingement surface, the uncertainty ranges from 1.74 to 3.10 or about 7.01%. In the case of the uniform heat flux impingement surface, the uncertainty of Nusselt number is in the range of 2.07 to 3.57 % for the circular jet array, and 2.41 to 3.39 % for the cusped ellipse jet array. The largest contributor to the uncertainty in both surface boundary conditions was the heat transfer coefficient.

APPENDIX B

RAW DATA TABLE

Table B-1. Raw Data and Corresponding Results of Isothermal Jet Impingement Surface, Circular Jet Array, $H/D_h = 1$

Voltage(V)	18.8	20.2	21.0	21.5	22.1
Resistance (Ohm)	16.4	16.4	16.4	16.4	16.4
Power (W)	21.55122	24.880488	26.890244	28.185976	29.781098

Jet Temp (inlet)	25.3	25.2	25.7	25.0	24.9
Jet Temp (plenum)	25.9	25.8	25.9	25.9	25.8
Copper Block Temp					
LF	41.4	40.8	41.4	41.2	40.8
RF	34.7	33.5	33.8	33.7	33.4
Center	35.3	34.2	34.5	34.3	34.0
LB	36.3	35.3	35.8	35.6	35.2
RB	39.8	38.8	39.3	39.5	38.6
Ave Surface Temp	37.5	36.5	37.0	36.9	36.4
Temp Difference	11.6	10.7	11.1	11.0	10.6

Plenum pressure (psi)	3.3839	6.3611	7.2117	8.2332	9.6395
Readout Flow Rate	8	10	11	12	14
Correction Factor	1.1091426	1.1969661	1.220898	1.2490323	1.2867588
Actual Flow Rate (acfm)	8.8731407	11.969661	13.429878	14.988387	18.014624
Volume Flow Rate (m^3/s)	0.0041877	0.0056491	0.0063382	0.0070738	0.0085020

Reynolds number	5909	7971	8943	9981	11996
h(ave)	592.43104	740.09599	775.28889	817.07953	900.6536
Nu	28.937978	36.150843	37.86988	39.911193	43.993464

METZGER					
Nusselt number	27.029444	33.561654	36.474661	39.488509	45.105026
Percent difference	6.5952582	7.1621815	3.684246	1.0590609	2.526652

OBOT					
Nusselt number	33.396836	42.433507	46.526575	50.798088	58.84961
Percent difference	15.408328	17.379025	22.859048	27.277799	33.768984

Table B-2. Raw Data and Corresponding Results of Isothermal Jet Impingement Surface, Circular Jet Array, $H/D_h = 2$

Voltage(V)	18.8	20.2	21.0	21.5	22.1
Resistance (Ohm)	16.4	16.4	16.4	16.4	16.4
Power (W)	21.55122	24.880488	26.890244	28.185976	29.781098

Jet Temp (inlet)	24.5	24.6	24.5	24.5	24.9
Jet Temp (plenum)	24.9	25	25	25	25.0
Copper Block Temp					
LF	41.8	41.3	41.3	41.2	40.8
RF	34.5	33.5	33.2	32.8	32.2
Center	35.3	34.5	34.2	33.9	33.3
LB	36.3	35.5	35.3	35.1	34.7
RB	39.0	38.7	38.6	38.3	37.7
Ave Surface Temp	37.4	36.7	36.5	36.3	35.7
Temp Difference	12.5	11.7	11.5	11.3	10.7

Plenum pressure (psi)	2.0914	3.7002	4.8786	5.8565	8.1807
Readout Flow Rate	8	10	11	12	14
Correction Factor	1.0687713	1.1188004	1.15407	1.1825402	1.2476018
Actual Flow Rate (acfm)	8.5502	11.188	12.6948	14.1905	17.4664
Volume Flow Rate (m^3/s)	0.0040353	0.0052802	0.0059913	0.0066972	0.0082433

Reynolds number	5694	7451	8454	9450	11632
h(ave)	550.65706	678.10504	744.33117	798.21269	884.22006
Nu	26.897479	33.122823	36.357715	38.98962	43.190749

METZGER					
Nusselt number	25.110103	30.40837	33.270782	36.016687	41.757089
Percent difference	6.6451431	8.1951137	8.4904482	7.6249352	3.3193681

OBOT					
Nusselt number	26.609898	32.996218	36.505886	39.908036	47.122131
Percent difference	1.0691744	0.3822298	0.4075356	2.3555407	9.1023695

Table B-3. Raw Data and Corresponding Results of Isothermal Jet Impingement Surface, Circular Jet Array, $H/D_h = 3$

Voltage(V)	18.8	20.2	21.0	21.5	22.1
Resistance (Ohm)	16.4	16.4	16.4	16.4	16.4
Power (W)	21.55122	24.880488	26.890244	28.185976	29.781098

Jet Temp (inlet)	25.2	25.0	25.0	24.9	25.0
Jet Temp (plenum)	25.7	25.6	25.5	25.4	25.5
Copper Block Temp					
LF	42.0	41.3	41.3	41.2	40.8
RF	36.1	34.8	34.5	34.2	33.5
Center	36.8	35.5	35.2	35.0	34.4
LB	37.7	36.4	36.2	36.0	35.5
RB	41.4	40.8	41.0	40.9	40.3
Ave Surface Temp	38.8	37.8	37.6	37.5	36.9
Temp Difference	13.1	12.2	12.1	12.1	11.4

Plenum pressure (psi)	1.7988	3.4565	4.41	5.2553	7.5904
Readout Flow Rate	8	10	11	12	14
Correction Factor	1.0594184	1.1113668	1.1401754	1.1651195	1.2314032
Actual Flow Rate (acfm)	8.4754	11.1137	12.5419	13.9814	17.2396
Volume Flow Rate (m^3/s)	0.004	0.0052451	0.0059191	0.0065985	0.0081362

Reynolds number	5644	7401	8352	9311	11481
h(ave)	524.59543	652.45304	706.31756	745.26326	833.02837
Nu	25.624469	31.869822	34.500896	36.403244	40.690232

METZGER					
Nusselt number	25.243534	30.564812	33.287373	35.940519	41.667321
Percent difference	1.4866052	4.094812	3.5173654	1.2711086	2.4012851

OBOT					
Nusselt number	23.539886	29.239041	32.20823	35.13312	41.543008
Percent difference	8.135127	8.2547707	6.6452365	3.4890401	2.0957751

Table B-4. Raw Data and Corresponding Results of Isothermal Jet Impingement Surface, Circular Jet Array, $H/D_h = 4$

Voltage(V)	18.8	20.2	21.0	21.5	22.1
Resistance (Ohm)	16.4	16.4	16.4	16.4	16.4
Power (W)	21.55122	24.880488	26.890244	28.185976	29.781098

Jet Temp (inlet)	25.2	25.2	25.1	25.1	25.0
Jet Temp (plenum)	25.6	25.5	25.4	25.3	25.2
Copper Block Temp					
LF	42.1	41.2	41.1	41.0	40.4
RF	36.0	34.5	34.1	33.8	32.9
Center	36.6	35.2	34.9	34.6	33.8
LB	37.7	36.4	36.1	35.9	35.1
RB	42.5	42.1	42.2	42.2	41.7
Ave Surface Temp	39.0	37.9	37.7	37.5	36.8
Temp Difference	13.4	12.4	12.3	12.2	11.6

Plenum pressure (psi)	1.7744	3.4377	4.5076	5.4284	7.5307
Readout Flow Rate	8	10	11	12	14
Correction Factor	1.0586347	1.1107912	1.1430833	1.1701619	1.229753
Actual Flow Rate (acfm)	8.4691	11.1079	12.5739	14.042	17.2165
Volume Flow Rate (m^3/s)	0.003997	0.0052424	0.0059343	0.0066271	0.0081253

Reynolds number	5640	7397	8374	9351	11465
h(ave)	513.61735	640.85856	698.26508	736.71106	820.07975
Nu	25.088232	31.303476	34.107563	35.985502	40.057741

METZGER					
Nusselt number	23.184103	28.041736	30.588902	33.052143	38.131133
Percent difference	7.5897304	10.419737	10.316367	8.1515017	4.8095773

OBOT					
Nusselt number	21.67397	26.926147	29.733405	32.479686	38.231782
Percent difference	13.60902	13.983522	12.824598	9.7422995	4.558318

Table B-5. Raw Data and Corresponding Results of Isothermal Jet Impingement Surface, Cusped Ellipse Jet Array, $H/D_h = 1$

Voltage(V)	18.8	20.2	21.0	21.5	22.1
Resistance (Ohm)	16.4	16.4	16.4	16.4	16.4
Power (W)	21.55122	24.880488	26.890244	28.185976	29.781098

Jet Temp (inlet)	24.9	24.7	24.7	24.7	24.8
Jet Temp (plenum)	24.8	24.9	24.9	24.9	25.0
Copper Block Temp					
LF	41.0	40.7	40.8	40.7	40.5
RF	33.9	33.0	33.1	32.9	32.5
Center	34.5	33.7	33.9	33.9	33.5
LB	35.4	34.8	35.1	34.9	34.3
RB	40.1	39.0	39.0	38.8	38.4
Ave Surface Temp	37.0	36.2	36.4	36.2	35.8
Temp Difference	12.2	11.3	11.5	11.3	10.8
Plenum pressure (psi)	3.3555	6.1036	7.6573	8.9426	10.0785
Readout Flow Rate	8	10	11	12	14
Correction Factor	1.1082713	1.1896264	1.2332497	1.2682035	1.2983113
Actual Flow Rate (acfm)	8.8662	11.8963	13.5658	15.2184	18.1764
Volume Flow Rate (m^3/s)	0.0041844	0.0056144	0.0064023	0.0071823	0.0085783

Reynolds number	5290	7098	8094	9080	10845
h(ave)	564.22004	699.63219	746.92466	792.4392	875.8136
Nu	27.559979	34.174342	36.484397	38.707607	42.780126

Table B-6. Raw Data and Corresponding Results of Isothermal Jet Impingement Surface, Cusped Ellipse Jet Array, $H/D_h = 2$

Voltage(V)	18.8	20.2	21.0	21.5	22.1
Resistance (Ohm)	16.4	16.4	16.4	16.4	16.4
Power (W)	21.55122	24.880488	26.890244	28.185976	29.781098

Jet Temp (inlet)	24.7	24.2	24.2	24.3	24.3
Jet Temp (plenum)	24.7	24.5	24.7	24.8	24.8
Copper Block Temp					
LF	41.7	41.0	41.6	41.6	41.2
RF	35.0	33.6	33.8	33.6	32.9
Center	35.5	34.2	34.5	34.3	33.6
LB	36.5	35.2	35.7	35.5	34.9
RB	41.1	40.0	40.5	40.4	39.8
Ave Surface Temp	38.0	36.8	37.2	37.1	36.5
Temp Difference	13.3	12.3	12.5	12.3	11.7

Plenum pressure (psi)	1.5956	3.0475	3.6896	4.3071	5.7836
Readout Flow Rate	8	10	11	12	14
Correction factor	1.0528743	1.0987779	1.1184781	1.1371016	1.1804415
Actual Flow Rate (acfm)	8.4229941	10.987779	12.303259	13.645219	16.526181
Volume Flow Rate (m^3/s)	0.0039752	0.0051857	0.0058065	0.0064399	0.0077995

Reynolds number	5025	6556	7341	8141	9860
h(ave)	518.26547	645.02675	685.42727	731.91163	813.05852
Nu	25.315275	31.507076	33.480486	35.751068	39.714781

Table B-7. Raw Data and Corresponding Results of Isothermal Jet Impingement Surface, Cusped Ellipse Jet Array, $H/D_h = 3$

Voltage(V)	18.8	20.2	21.0	21.5	22.1
Resistance (Ohm)	16.4	16.4	16.4	16.4	16.4
Power (W)	21.55122	24.880488	26.890244	28.185976	29.781098

Jet Temp (inlet)	24.3	24.0	24.1	24.0	24.0
Jet Temp (plenum)	24.4	24.1	24.1	24.1	24.2
Copper Block Temp					
LF	42.4	42.1	42.3	42.3	42.0
RF	34.8	33.6	33.5	33.2	32.6
Center	35.3	34.2	34.1	33.9	33.3
LB	36.3	35.4	35.3	35.2	34.7
RB	41.4	40.7	40.7	40.4	39.7
Ave Surface Temp	38.0	37.2	37.2	37.0	36.5
Temp Difference	13.6	13.1	13.1	12.9	12.3

Plenum pressure (psi)	1.5145	2.6873	3.3644	4.0851	5.4449
Readout Flow Rate	8	10	11	12	14
Correction factor	1.050251	1.0875705	1.1085444	1.1304415	1.1706414
Actual Flow Rate (acfm)	8.4020082	10.875705	12.193989	13.565298	16.38898
Volume Flow Rate (m^3/s)	0.0039653	0.0051328	0.005755	0.0064021	0.0077348

Reynolds number	5013	6489	7275	8094	9778
h(ave)	503.82699	605.6358	655.55773	696.73449	774.59408
Nu	24.610011	29.58298	32.021474	34.0328	37.835942

Table B-8. Raw Data and Corresponding Results of Isothermal Jet Impingement Surface, Cusped Ellipse Jet Array, $H/D_h = 4$

Voltage(V)	18.8	20.2	21.0	21.5	22.1
Resistance (Ohm)	16.4	16.4	16.4	16.4	16.4
Power (W)	21.55122	24.880488	26.890244	28.185976	29.781098

Jet Temp (inlet)	23.6	23.6	23.6	23.5	23.5
Jet Temp (plenum)	23.7	23.7	23.8	23.8	23.8
Copper Block Temp					
LF	40.4	40.6	40.7	40.7	40.4
RF	34.3	33.9	33.6	33.4	32.7
Center	34.9	34.5	34.3	34.0	33.4
LB	35.9	35.7	35.6	35.4	34.8
RB	41.5	41.8	41.9	41.9	41.3
Ave Surface Temp	37.4	37.3	37.2	37.1	36.5
Temp Difference	13.7	13.6	13.4	13.3	12.7

Plenum pressure (psi)	1.501	2.4789	3.2127	3.9251	5.4261
Readout Flow Rate	8	10	11	12	14
Correction Factor	1.0498137	1.0810331	1.10388	1.125617	1.1700951
Actual Flow Rate (acfm)	8.3985097	10.810331	12.14268	13.507404	16.381331
Volume Flow Rate (m^3/s)	0.0039637	0.0051019	0.0057307	0.0063748	0.0077312

Reynolds number	5011	6450	7245	8059	9774
h(ave)	501.62045	583.36978	638.94897	676.79781	746.58203
Nu	24.502229	28.49537	31.210199	33.05897	36.467661

Table B-9. Raw Data and Corresponding Results of Uniform Heat Flux Jet Impingement Surface, Circular Jet Array, $H/D_h = 1$

Voltage (V)	1.10	1.10	1.15	1.32	1.5
Current (A)	13.329	13.359	14.07	15.38	16.705
Power (W)	14.6619	14.6949	16.1805	20.3016	25.0575

Temperature (°C)					
Plenum	23.7	23.7	23.8	23.8	23.9
Upstream	23.0	23.1	23.3	23.4	23.4
Ambient	22.9	23.0	23.1	23.2	23.3

Plenum Pressure (mV)	3.31	4.80	5.90	6.72	9.00
Plenum Pressure (psi)	1.09168865	1.58311346	1.94591029	2.2163588	2.9683377
Readout Flow Rate	8	10	11	12	14
Correction Factor	1.03646733	1.0524708	1.06413103	1.0727407	1.0963246
Actual Flow Rate (acfm)	8.29173867	10.524708	11.7054413	12.872889	15.348545
Actual Flow Rate (m^3/s)	0.00391329	0.00496714	0.00552438	0.0060754	0.0072437

Reynolds number	5522	7009	7795	8572	10221
h(ave)	889.6569	1006.9	1135.3	1307.4	1395.4
Nu(ave)	43.321	49.0283	55.2831	63.6637	67.9489

VISKANTA					
Nusselt Number	30.6068385	36.2534409	39.096279	41.82636	47.390121
Percent Difference	29.3487257	26.0560923	29.2798722	34.301086	30.256236

SCHROEDER					
Nusselt Number	43.4303478	51.2346144	55.1524288	58.908422	66.545161
Percent Difference	0.25241292	4.50008339	0.23636736	7.4693717	2.0658741

Table B-10. Raw Data and Corresponding Results of Uniform Heat Flux Jet Impingement Surface, Circular Jet Array, $H/D_h = 2$

Voltage (V)	1.42	1.45	1.5	1.52	1.65
Current (A)	16.370	16.890	17.180	17.370	18.380
Power (W)	23.2454	24.4905	25.77	26.4024	30.327

Temperature (°C)					
Plenum	21.3	21.7	21.9	22.1	22.2
Upstream	20.9	21.2	21.4	21.5	21.7
Ambient	21.2	21.4	21.6	21.8	21.9

Plenum Pressure (mV)	3.31	4.75	5.74	6.70	8.73
Plenum Pressure (psi)	1.09168865	1.56662269	1.89313984	2.2097625	2.8792876
Readout Flow Rate	8	10	11	12	14
Correction Factor	1.03646733	1.05193772	1.06244295	1.0725316	1.0935584
Actual Flow Rate (acfm)	8.29173867	10.5193772	11.6868725	12.870379	15.309817
Actual Flow Rate (m^3/s)	0.00391329	0.00496462	0.00551562	0.0060742	0.0072255

Reynolds number	5522	7005	7783	8571	10195
h(ave)	881.3292	1030.7	1148.5	1256.1	1349.5
Nu(ave)	42.9154	50.1888	55.9231	61.1647	65.7125

VISKANTA					
Nusselt Number	28.1062373	33.279535	35.8616382	38.403798	43.440322
Percent Difference	34.5078053	33.6913116	35.8733006	37.212481	33.893366

SCHROEDER					
Nusselt Number	40.3827437	47.6226445	51.2258699	54.767285	61.767302
Percent Difference	5.90150926	5.11300439	8.39944506	10.459326	6.0037256

Table B-11. Raw Data and Corresponding Results of Uniform Heat Flux Jet Impingement Surface, Circular Jet Array, $H/D_h = 3$

Voltage (V)	0.80	1.04	1.10	1.16	1.29
Current (A)	12.400	13.890	14.370	14.870	15.870
Power (W)	9.92	14.4456	15.807	17.2492	20.4723

Temperature (°C)					
Plenum	23.1	23.1	23.2	23.3	23.3
Upstream	22.2	22.3	22.6	22.8	22.9
Ambient	22.6	22.7	22.9	23	23.1

Plenum Pressure (mV)	3.25	4.10	5.37	6.62	8.39
Plenum Pressure (psi)	1.0718997	1.3522427	1.7711082	2.1833773	2.7671504
Readout Flow Rate	8	10	11	12	14
Correction Factor	1.0358177	1.0449829	1.0585290	1.0716945	1.0900649
Actual Flow Rate (acfm)	8.2865418	10.4498292	11.6438185	12.8603338	15.2609088
Actual Flow Rate (m^3/s)	0.0039108	0.0049318	0.0054953	0.0060694	0.0072024

Reynolds number	5518	6959	7754	8564	10163
h(ave)	770.1043	889.4904	998.553	1079.6	1241
Nu(ave)	37.4995	43.3128	48.6235	52.5710	60.4282

VISKANTA					
Nusselt Number	26.7263245	31.510965	34.0268645	36.514324	41.232177
Percent Difference	28.728851	27.2479151	30.0197138	30.542838	31.766664

SCHROEDER					
Nusselt Number	38.6818186	45.4272912	48.9641593	52.454889	59.060264
Percent Difference	3.15289157	4.88190827	0.70060621	0.2208647	2.2637372

Table B-12. Raw Data and Corresponding Results of Uniform Heat Flux Jet Impingement Surface, Circular Jet Array, $H/D_h = 4$

Voltage (V)	0.70	0.85	0.90	0.97	1.05
Current (A)	11.290	12.370	12.370	13.169	13.780
Power (W)	7.903	10.5145	11.133	12.77393	14.469

Temperature (°C)					
Plenum	23.6	23.6	23.6	23.7	23.8
Upstream	22.7	22.9	23.0	23.2	23.3
Ambient	23.2	23.2	23.3	23.4	23.5

Plenum Pressure (mV)	3.21	4.45	5.24	6.27	8.29
Plenum Pressure (psi)	1.05870712	1.4676781	1.72823219	2.067942	2.7341689
Readout Flow Rate	8	10	11	12	14
Correction Factor	1.03538442	1.04873354	1.05715033	1.0680245	1.0890353
Actual Flow Rate (acfm)	8.28307534	10.4873354	11.6286536	12.816294	15.246494
Actual Flow Rate (m^3/s)	0.0039092	0.0049495	0.00548814	0.0060486	0.0071956

Reynolds number	5516	6984	7744	8535	10153
h(ave)	750.0824	880.0403	936.8245	1057	1176.3
Nu(ave)	36.5245	42.8527	45.6177	51.4703	57.2791

VISKANTA					
Nusselt Number	25.7894902	30.4929173	32.8135042	35.159125	39.771998
Percent Difference					

SCHROEDER					
Nusselt Number	37.519962	44.1851729	47.464346	50.773253	57.265414
Percent Difference	2.72546379	3.10942577	4.04809092	1.3542707	0.0238928

Table B-13. Raw Data and Corresponding Results of Uniform Heat Flux Jet Impingement Surface, Cusped Ellipse Jet Array, $H/D_h = 1$

Voltage (V)	1.28	1.33	1.49	1.59	1.74
Current (A)	14.760	15.300	16.511	17.220	18.330
Power (W)	18.8928	20.349	24.60139	27.3798	31.8942

Temperature (°C)					
Plenum	22.5	22.5	22.6	22.7	22.7
Upstream	21.6	21.6	21.8	22.0	22.0
Ambient	22.2	22.3	22.5	22.6	22.7

Plenum Pressure (mV)	3.03	4.08	4.85	5.68	7.7
Plenum Pressure (psi)	0.9993404	1.3456464	1.5996042	1.8733509	2.5395778
Readout Flow Rate	8	10	11	12	14
Correction Factor	1.0334323	1.0447682	1.0530036	1.0618092	1.0829406
Actual Flow Rate (acfm)	8.2674585	10.447682	11.58304	12.741711	15.161169
Actual Flow Rate (m^3/s)	0.0039018	0.0049308	0.0054666	0.0060135	0.0071553

Reynolds number	4933	6233	6911	7602	9046
h(ave)	875.4708	987.0456	1169.3	1320.8	1550.4
Nu(ave)	42.6302	48.0632	56.9376	64.3147	79.4536

Table B-14. Raw Data and Corresponding Results of Uniform Heat Flux Jet Impingement Surface, Cusped Ellipse Jet Array, $H/D_h = 2$

Voltage (V)	1.19	1.28	1.33	1.50	1.59
Current (A)	14.260	14.990	15.400	16.700	17.400
Power (W)	16.9694	19.1872	20.482	25.05	27.666

Temperature (°C)					
Plenum	22.3	22.4	22.5	22.6	22.6
Upstream	21.5	21.6	21.7	21.8	21.9
Ambient	22.3	22.5	22.6	22.7	22.8

Plenum Pressure (mV)	2.98	4.10	4.53	5.38	6.95
Plenum Pressure (psi)	0.9828496	1.3522427	1.4940633	1.7744063	2.2922164
Readout Flow Rate	8	10	11	12	14
Correction Factor	1.0328894	1.0449829	1.0495889	1.0586349	1.0751433
Actual Flow Rate (acfm)	8.2631152	10.449829	11.545478	12.703619	15.052006
Actual Flow Rate (m^3/s)	0.0038998	0.0049318	0.0054489	0.0059955	0.0071038

Reynolds number	4930	6235	6888	7579	8981
h(ave)	810.9993	975.3012	1061.2	1259.4	1419.3
Nu(ave)	39.4908	47.4913	51.6737	61.3232	69.109

Table B-15. Raw Data and Corresponding Results of Uniform Heat Flux Jet Impingement Surface, Cusped Ellipse Jet Array, $H/D_h = 3$

Voltage (V)	0.80	1.08	1.13	1.17	1.29
Current (A)	12.250	13.820	14.140	14.460	15.360
Power (W)	9.8	14.9256	15.9782	16.9182	19.8144

Temperature (°C)					
Plenum	23.0	23.2	23.3	23.5	23.5
Upstream	22.2	22.4	22.7	22.9	23.0
Ambient	22.9	23.0	23.1	23.2	23.3

Plenum Pressure (mV)	2.80	3.88	4.59	5.30	6.90
Plenum Pressure (psi)	0.9234828	1.2796834	1.5138522	1.7480211	2.2757256
Readout Flow Rate	8	10	11	12	14
Correction Factor	1.0309326	1.0426185	1.05023	1.0577868	1.0746215
Actual Flow Rate (acfm)	8.2474606	10.426185	11.55253	12.693442	15.0447
Actual Flow Rate (m^3/s)	0.0038924	0.0049206	0.0054522	0.0059907	0.0071003

Reynolds number	4921	6221	6893	7573	8976
h(ave)	761.545	884.3621	976.6387	1082.8	1263.3
Nu(ave)	37.0827	43.0631	47.5564	52.7243	61.514

Table B-16. Raw Data and Corresponding Results of Uniform Heat Flux Jet Impingement Surface, Cusped Ellipse Jet Array, $H/D_h = 4$

Voltage (V)	0.90	1.11	1.17	1.27	1.43
Current (A)	12.230	13.830	14.270	15.130	16.320
Power (W)	11.007	15.3513	16.6959	19.2151	23.3376

Temperature (°C)					
Plenum	22.7	22.7	22.6	22.7	22.8
Upstream	21.9	21.9	21.9	22.2	22.4
Ambient	22.7	22.7	22.8	22.9	22.9

Plenum Pressure (mV)	2.86	3.94	4.63	5.43	6.90
Plenum Pressure (psi)	0.9432718	1.2994723	1.5270449	1.7908971	2.2757256
Readout Flow Rate	8	10	11	12	14
Correction Factor	1.0315853	1.0432639	1.0506572	1.0591646	1.0746215
Actual Flow Rate (acfm)	8.2526821	10.432639	11.557229	12.709976	15.0447
Actual Flow Rate (m^3/s)	0.0038949	0.0049237	0.0054544	0.0059985	0.0071003

Reynolds number	4924	6225	6895	7583	8976
h(ave)	746.8088	835.5895	896.7092	1039.9	1249.3
Nu(ave)	26.3651	40.6882	43.6644	48.9496	60.8322

APPENDIX C

SLICE PLOTS

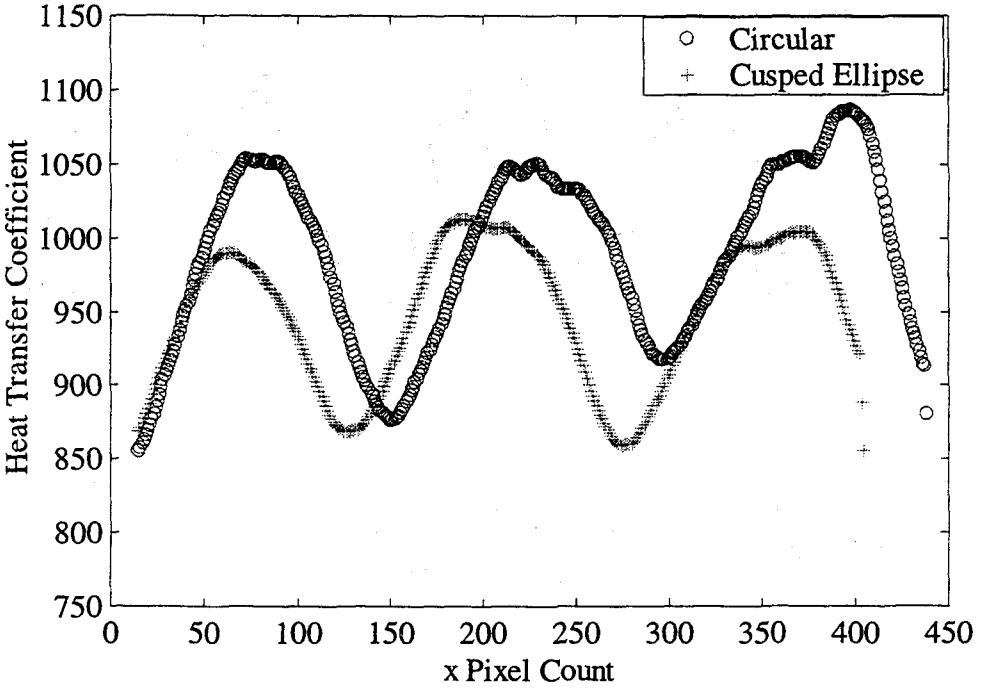

Figure C-1. Center Cross Section (x slice), Flow Rate 0.0039 m^3/s, $H/D_h = 1$

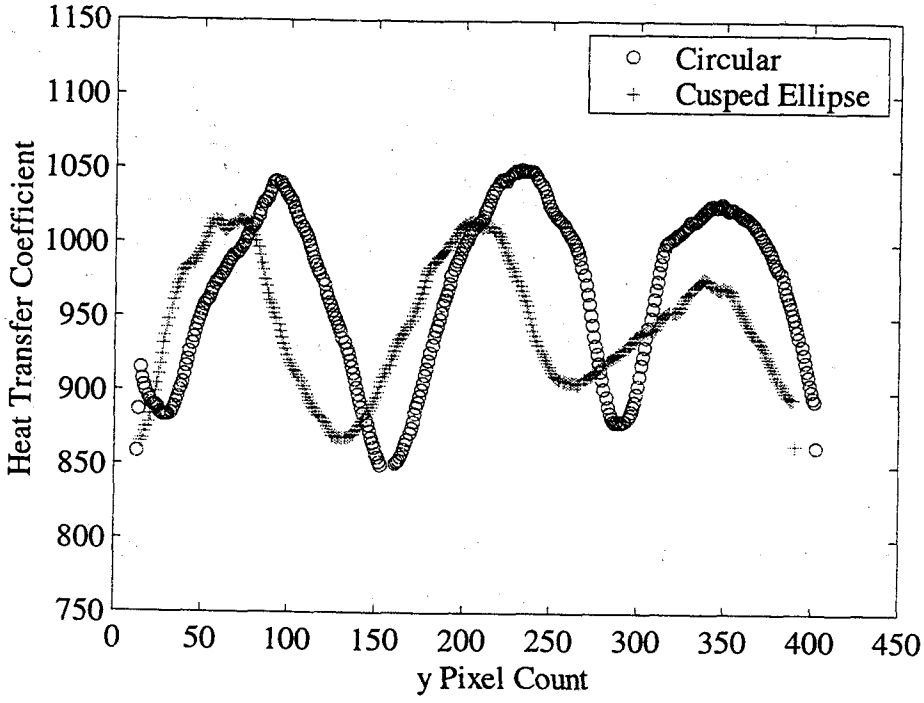

Figure C-2. Center Cross Section (y slice), Flow Rate 0.0039 m^3/s, $H/D_h = 1$

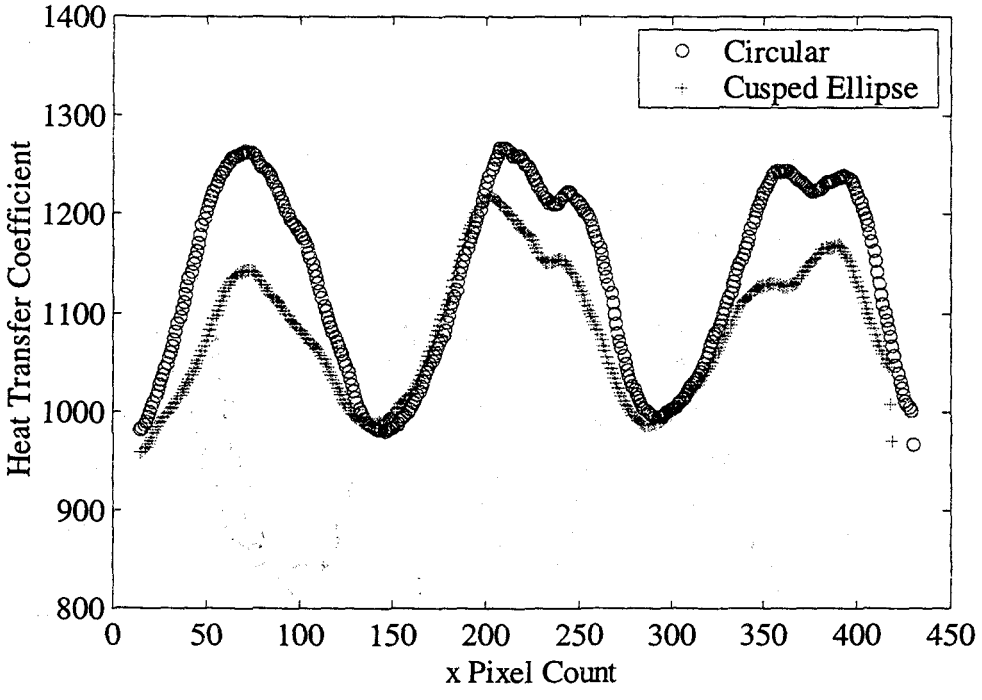

Figure C-3. Center Cross Section (x slice), Flow Rate 0.0049 m^3/s, $H/D_h = 1$

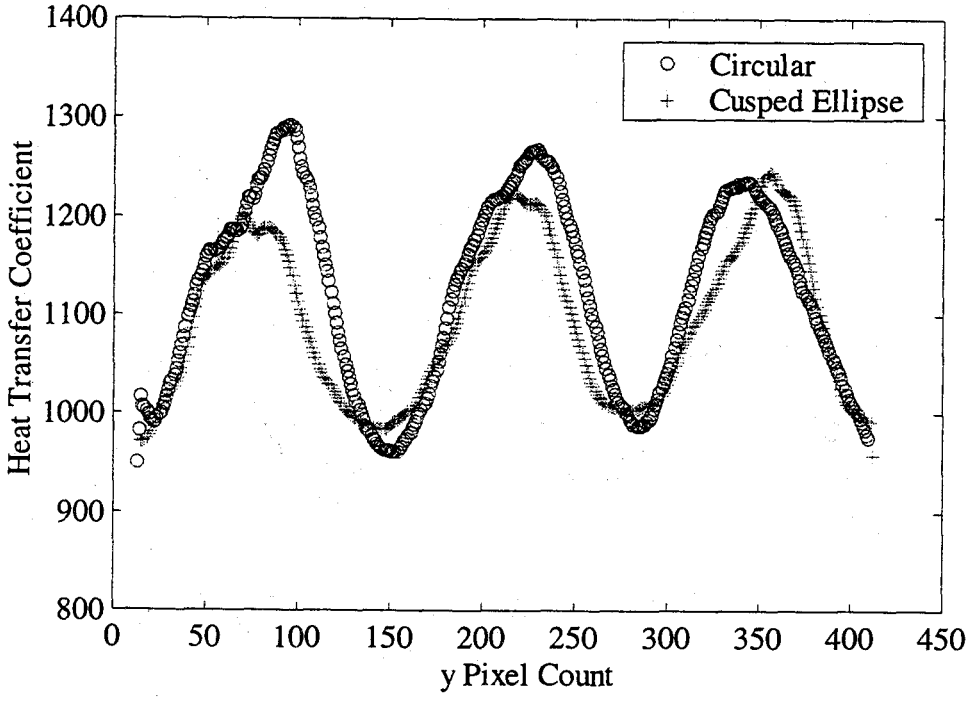

Figure C-4. Center Cross Section (y slice), Flow Rate 0.0049 m^3/s, $H/D_h = 1$

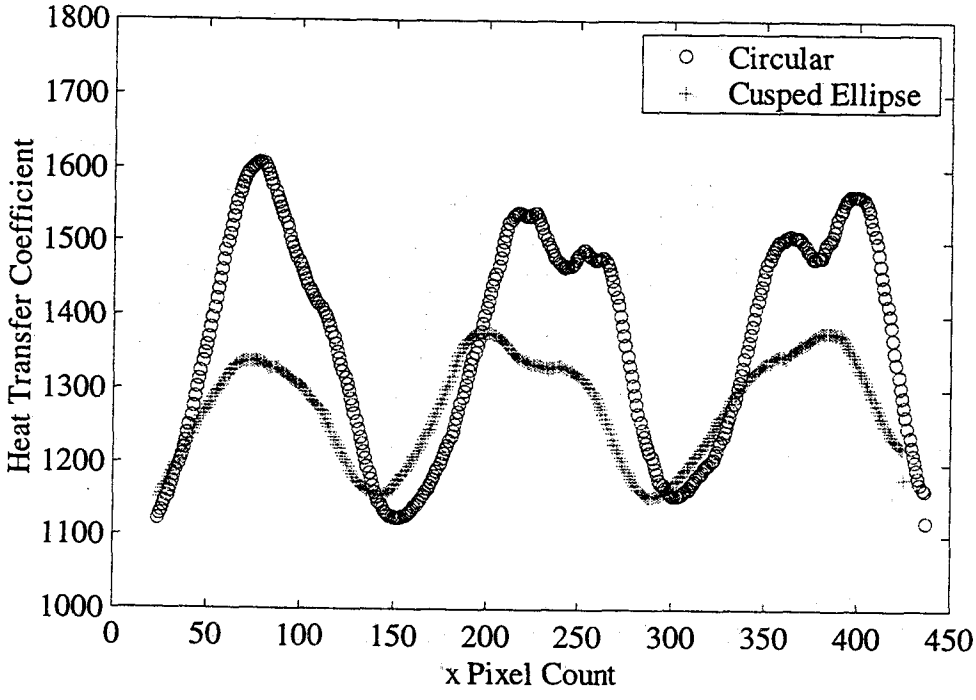

Figure C-5. Center Cross Section (x slice), Flow Rate 0.0055 m^3/s, $H/D_h = 1$

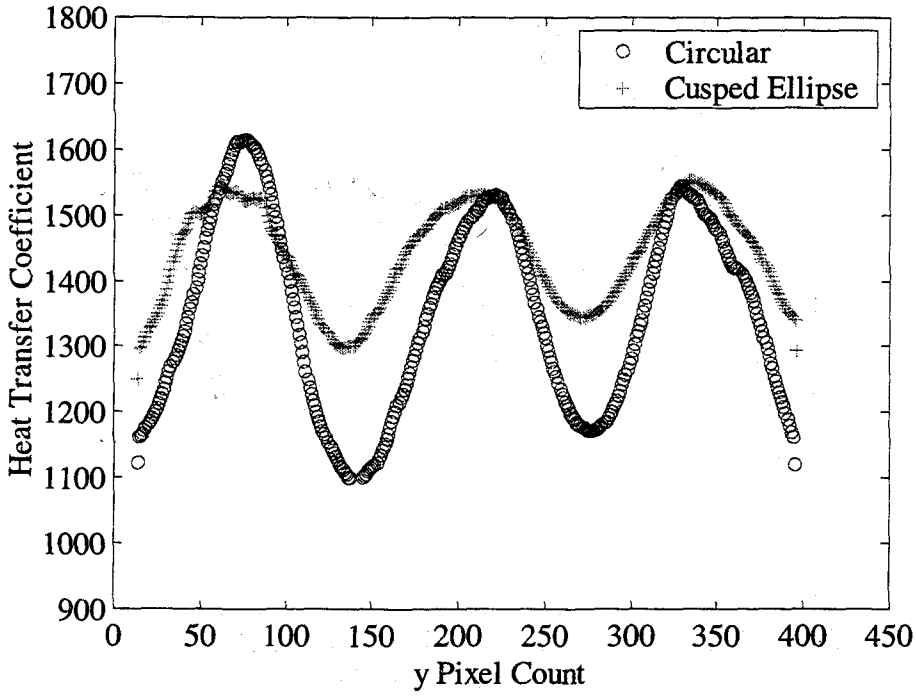

Figure C-6. Center Cross Section (y slice), Flow Rate 0.0055 m^3/s, $H/D_h = 1$

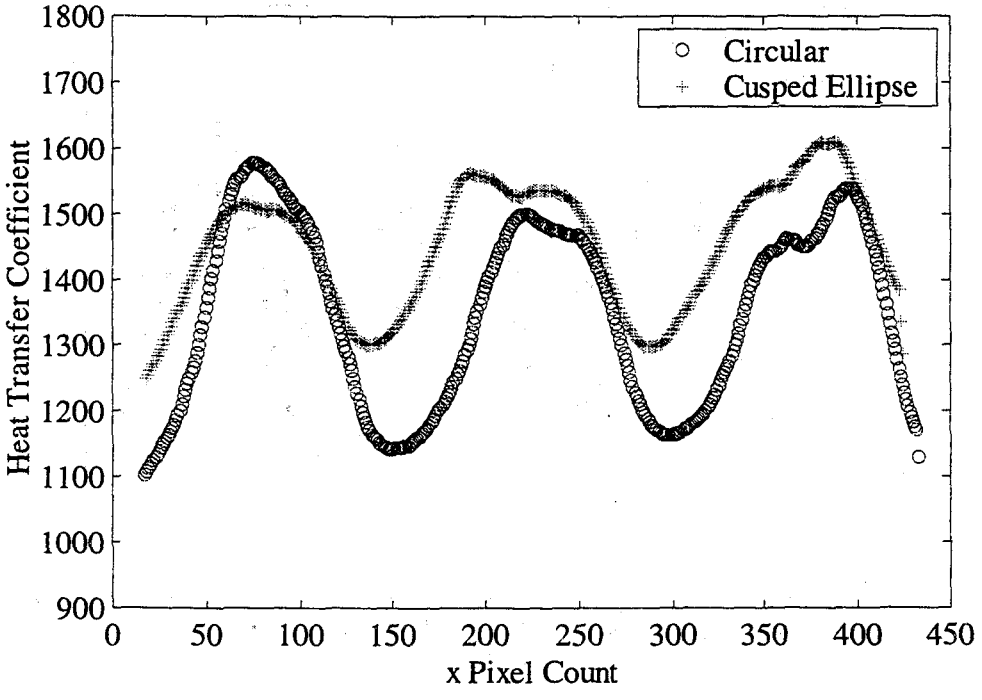

Figure C-7. Center Cross Section (x slice), Flow Rate 0.006 m^3/s, $H/D_h = 1$

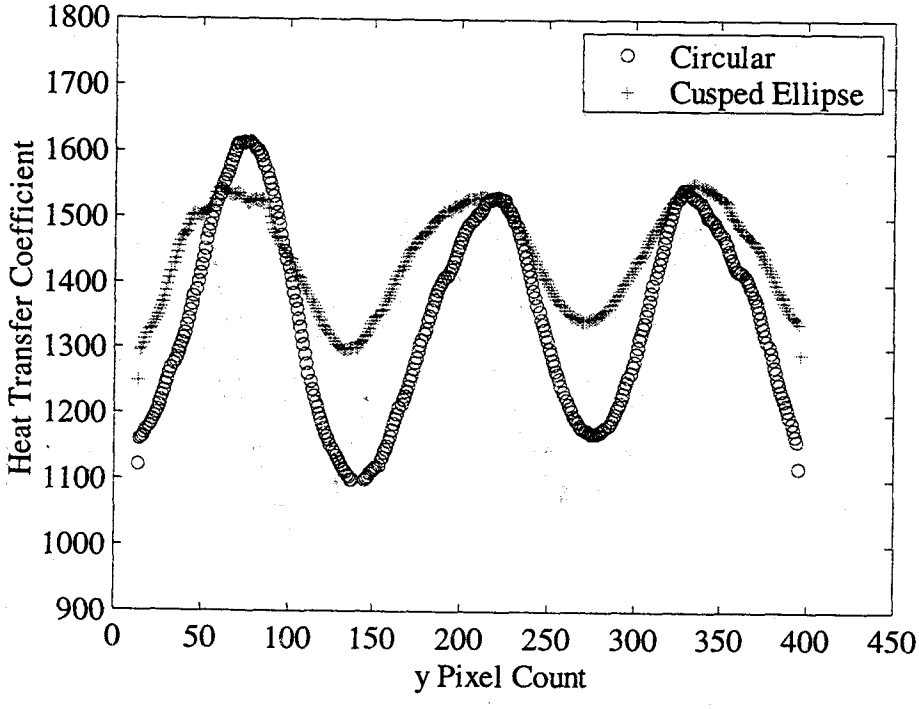

Figure C-8. Center Cross Section (y slice), Flow Rate 0.006 m^3/s, $H/D_h = 1$

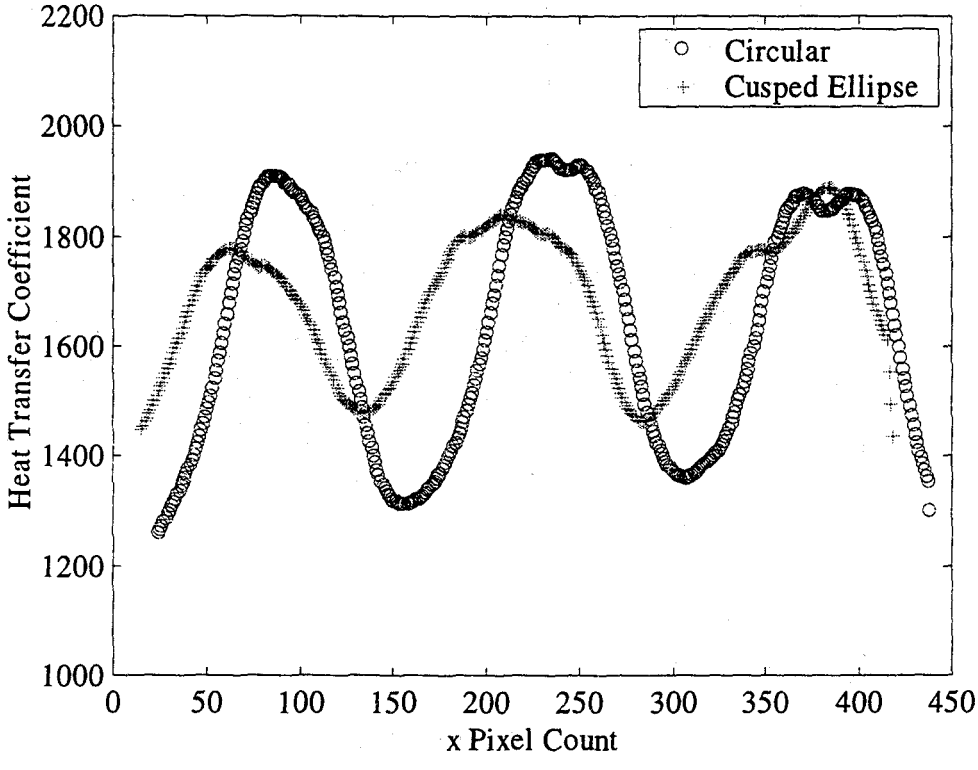

Figure C-9. Center Cross Section (x slice), Flow Rate 0.0072 m^3/s, $H/D_h = 1$

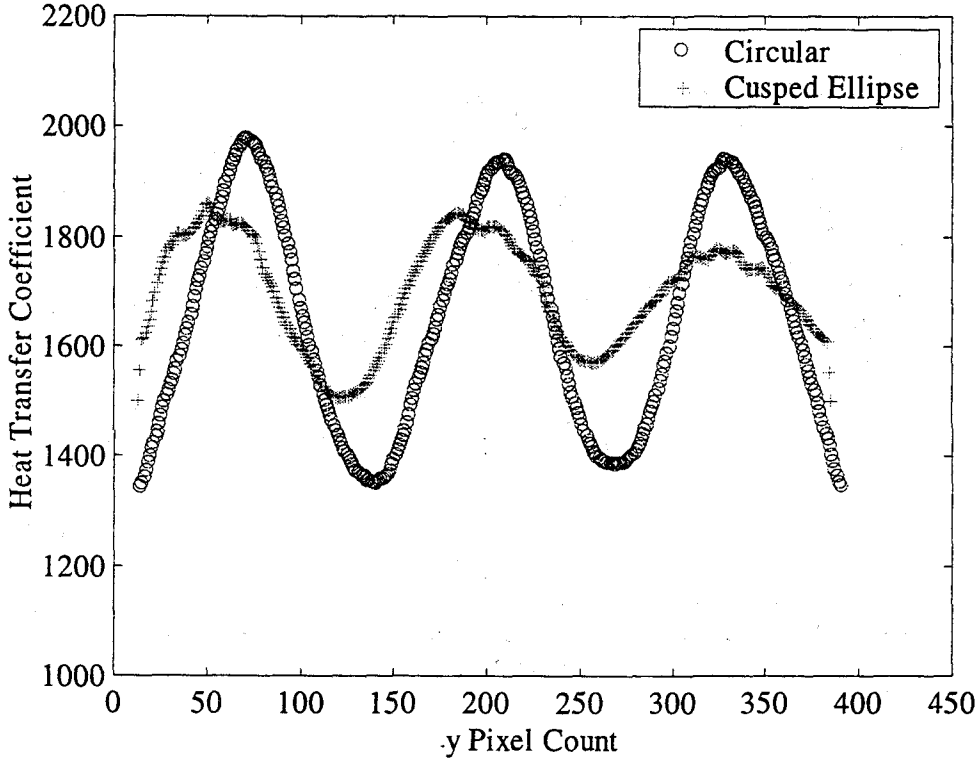

Figure C-10. Center Cross Section (y slice), Flow Rate 0.0072 m^3/s, $H/D_h = 1$

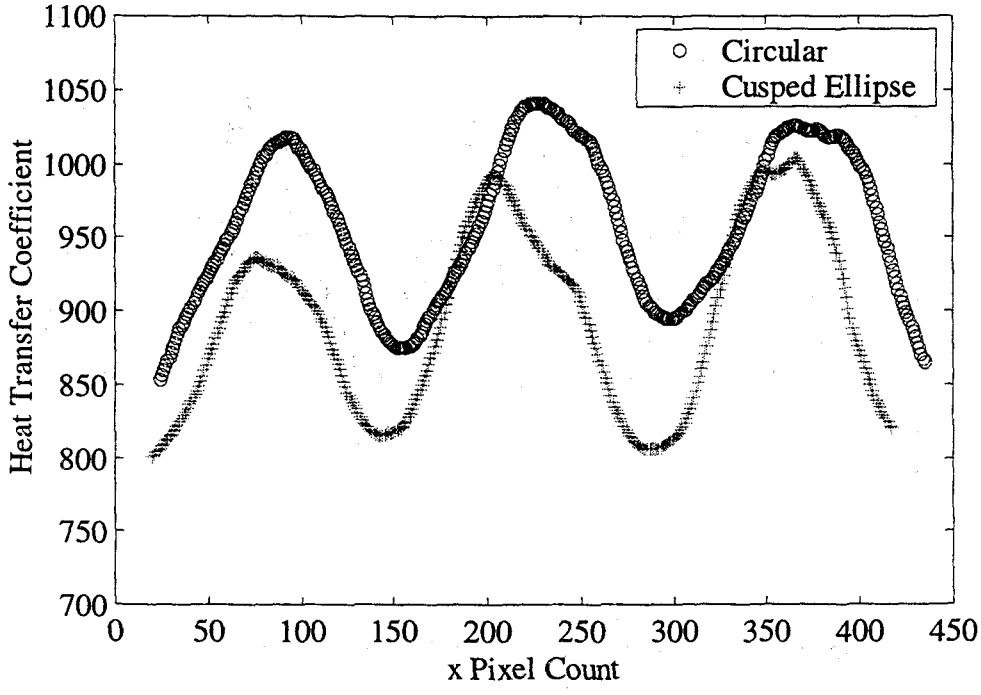

Figure C-11. Center Cross Section (x slice), Flow Rate 0.0039 m^3/s, $H/D_h = 2$

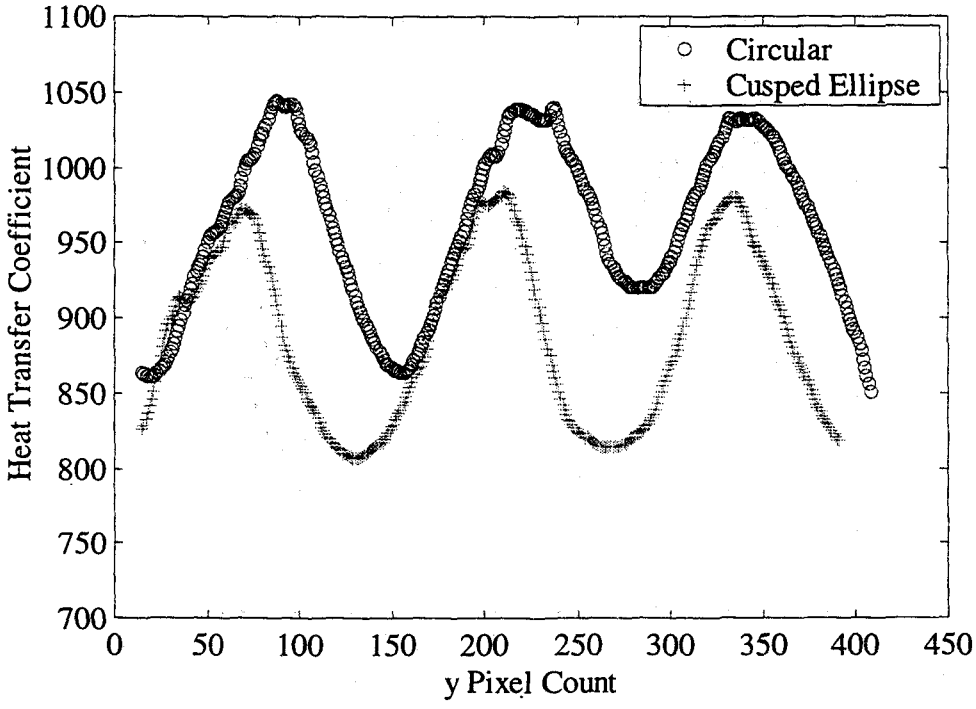

Figure C-12. Center Cross Section (y slice), Flow Rate 0.0039 m^3/s, $H/D_h = 2$

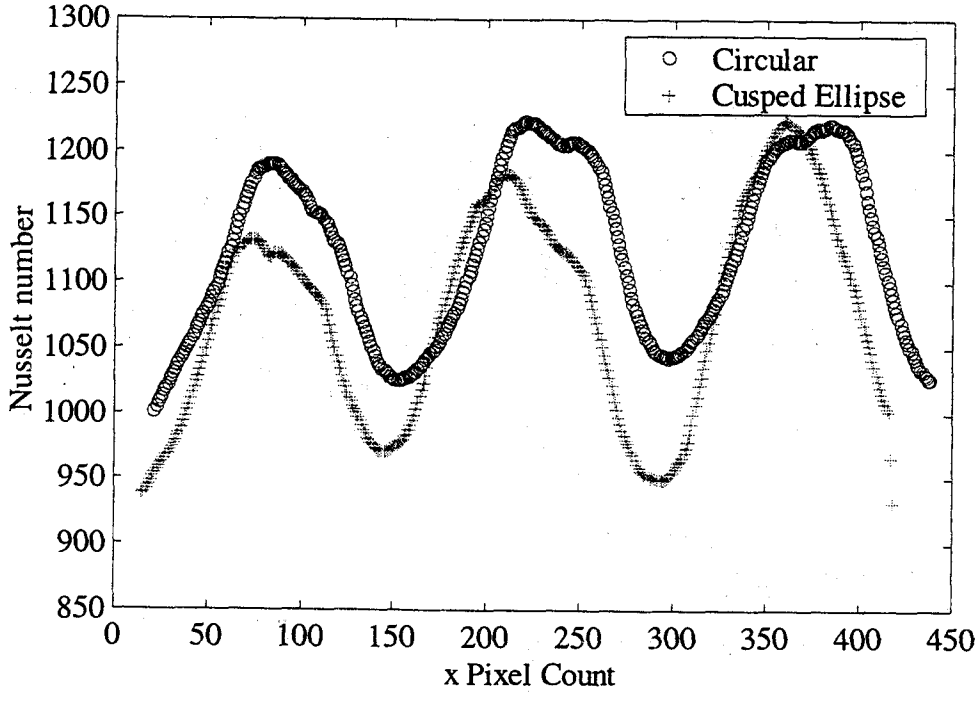

Figure C-13. Center Cross Section (x slice), Flow Rate 0.0049 m^3/s, $H/D_h = 2$

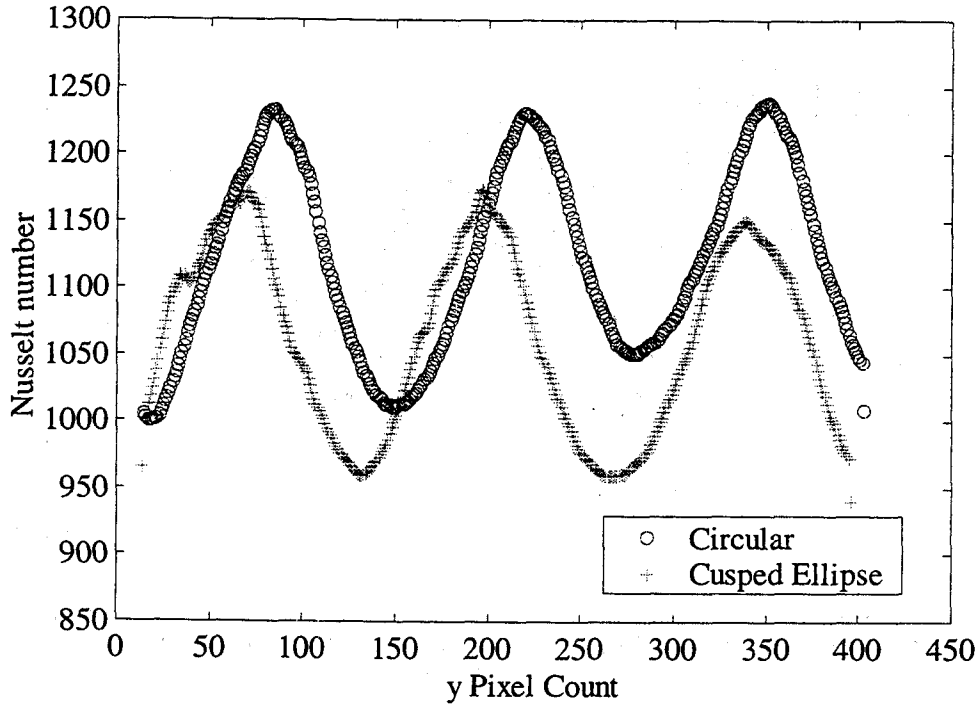

Figure C-14. Center Cross Section (y slice), Flow Rate 0.0049 m^3/s, $H/D_h = 2$

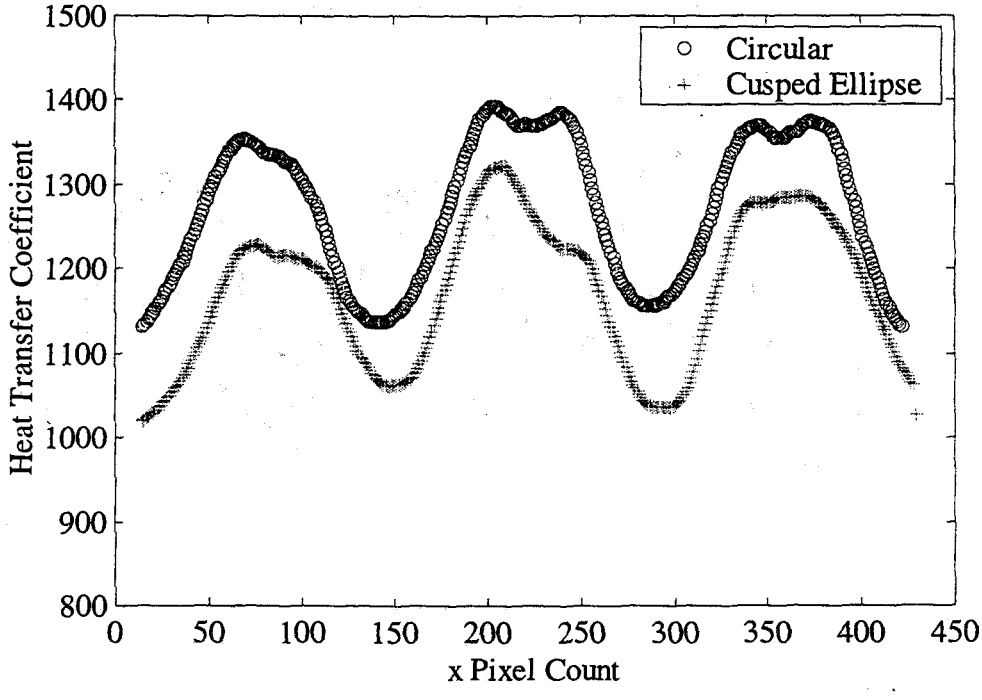

Figure C-15. Center Cross Section (x slice), Flow Rate 0.0055 m^3/s, $H/D_h = 2$

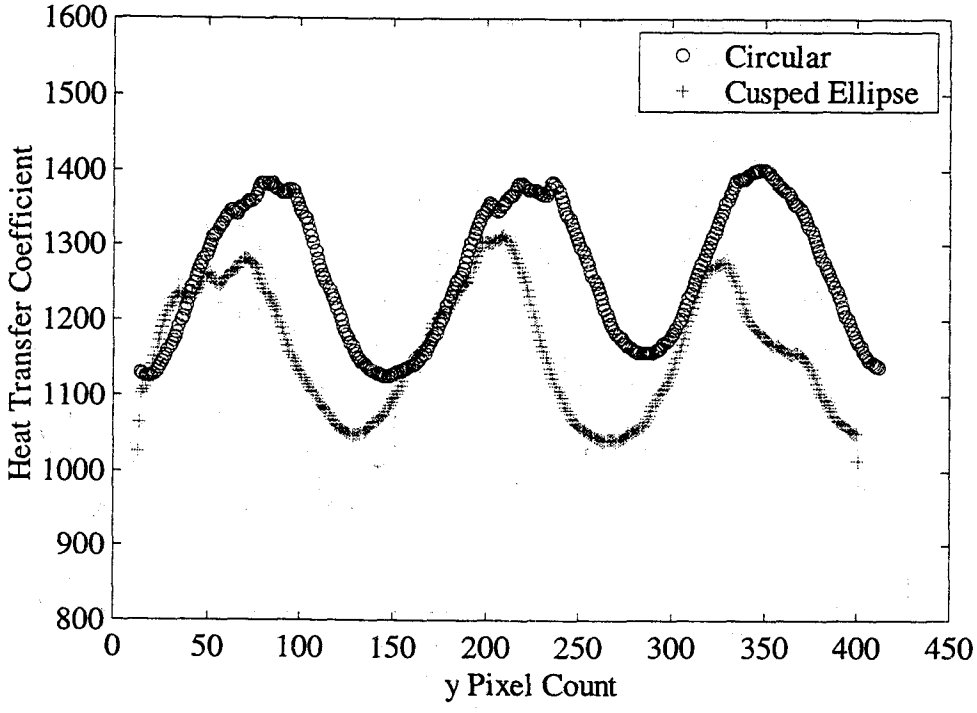

Figure C-16. Center Cross Section (y slice), Flow Rate 0.0055 m^3/s, $H/D_h = 2$

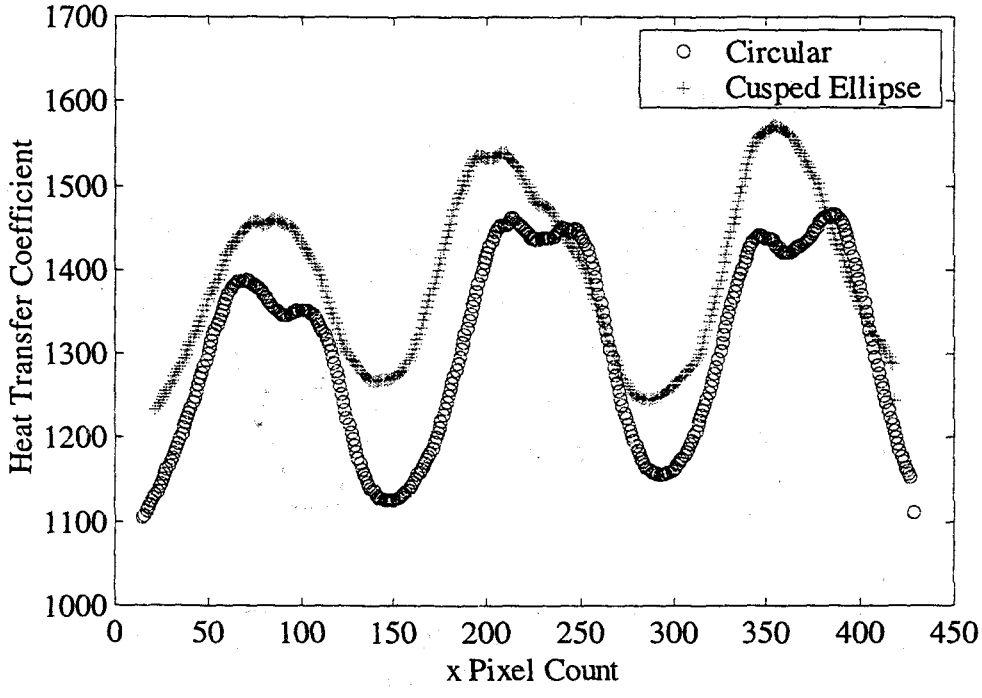

Figure C-17. Center Cross Section (x slice), Flow Rate 0.006 m^3/s, $H/D_h = 2$

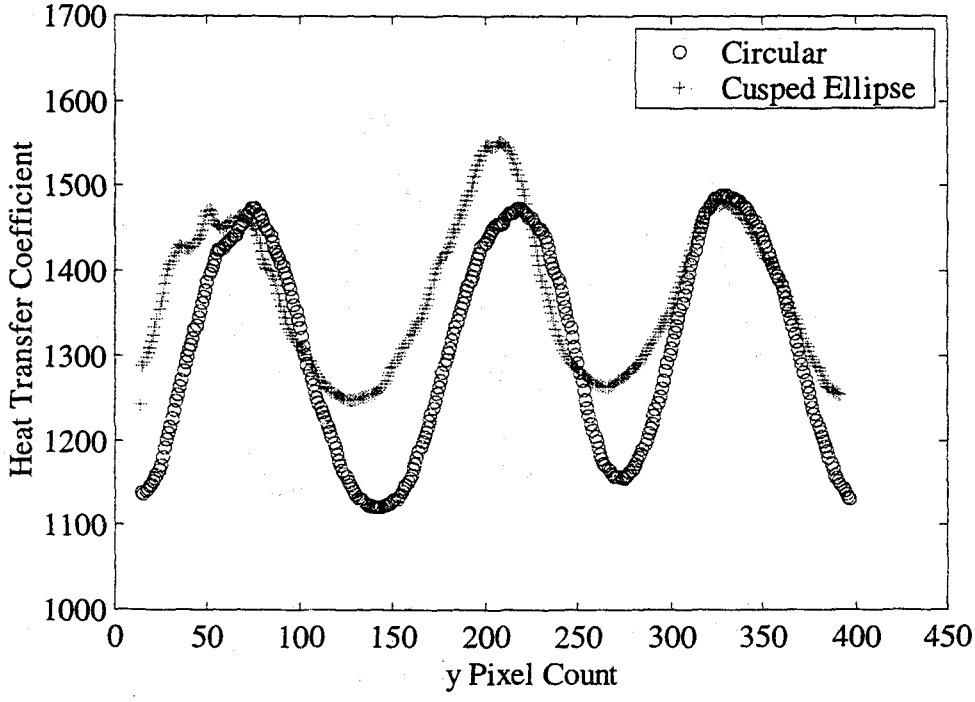

Figure C-18. Center Cross Section (y slice), Flow Rate 0.006 m^3/s, $H/D_h = 2$

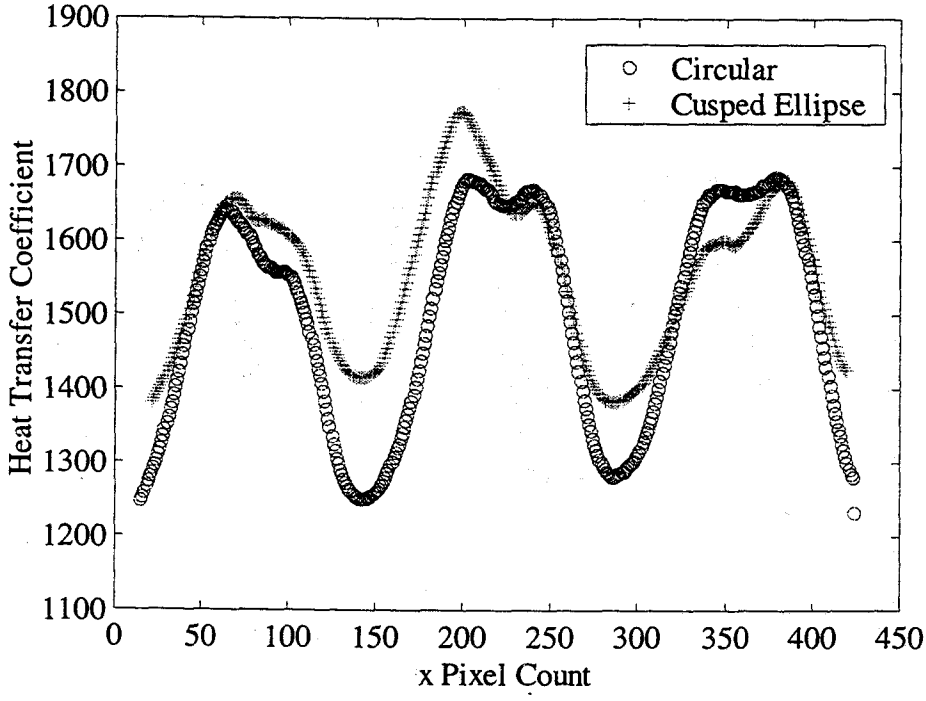

Figure C-19. Center Cross Section (x slice), Flow Rate 0.007 m^3/s, $H/D_h = 2$

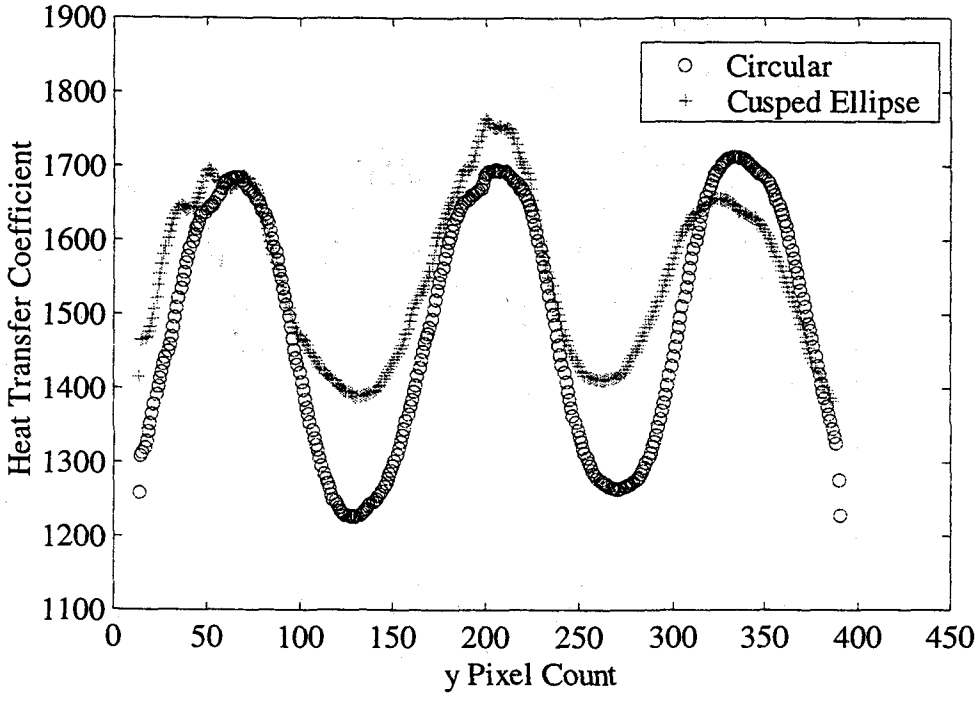

Figure C-20. Center Cross Section (y slice), Flow Rate 0.007 m^3/s, $H/D_h = 2$

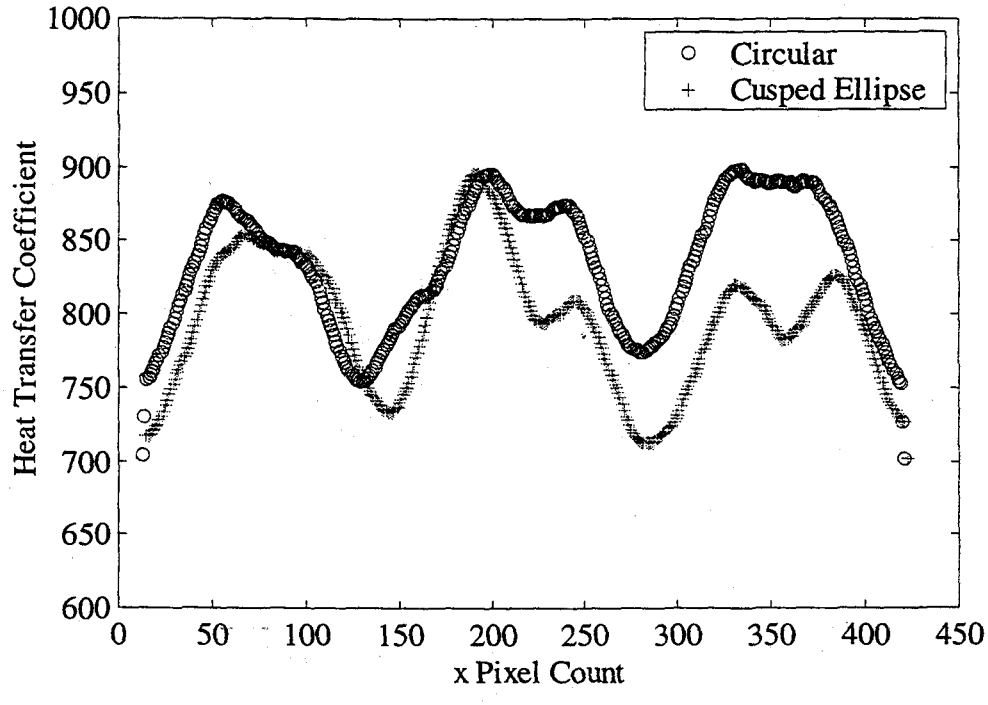

Figure C-21. Center Cross Section (x slice), Flow Rate 0.0039 m^3/s, $H/D_h = 3$

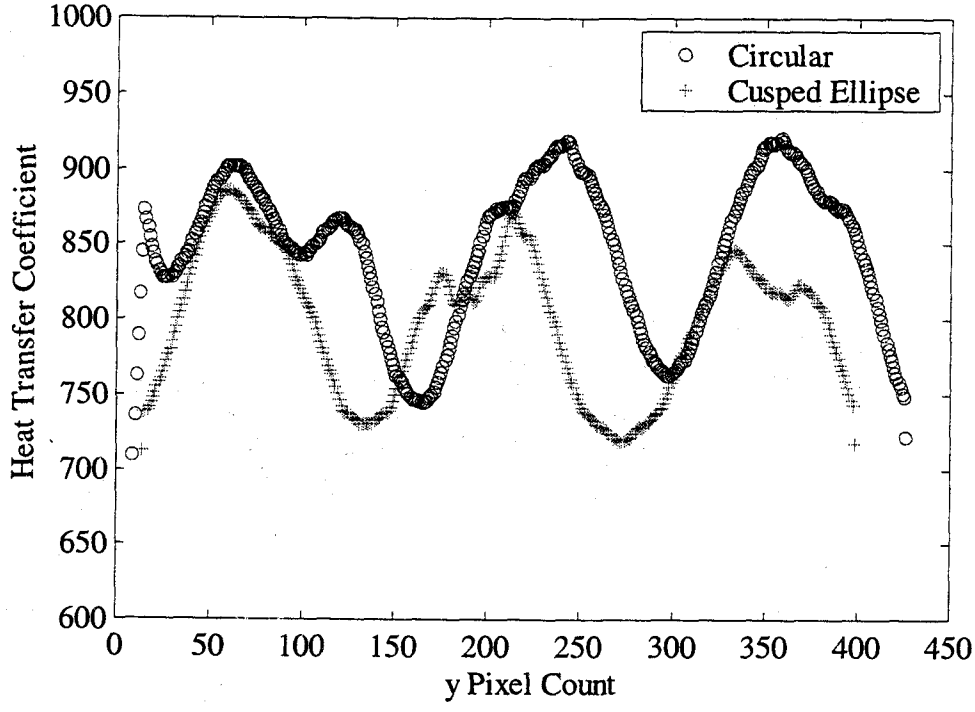

Figure C-22. Center Cross Section (y slice), Flow Rate 0.0039 m^3/s, $H/D_h = 3$

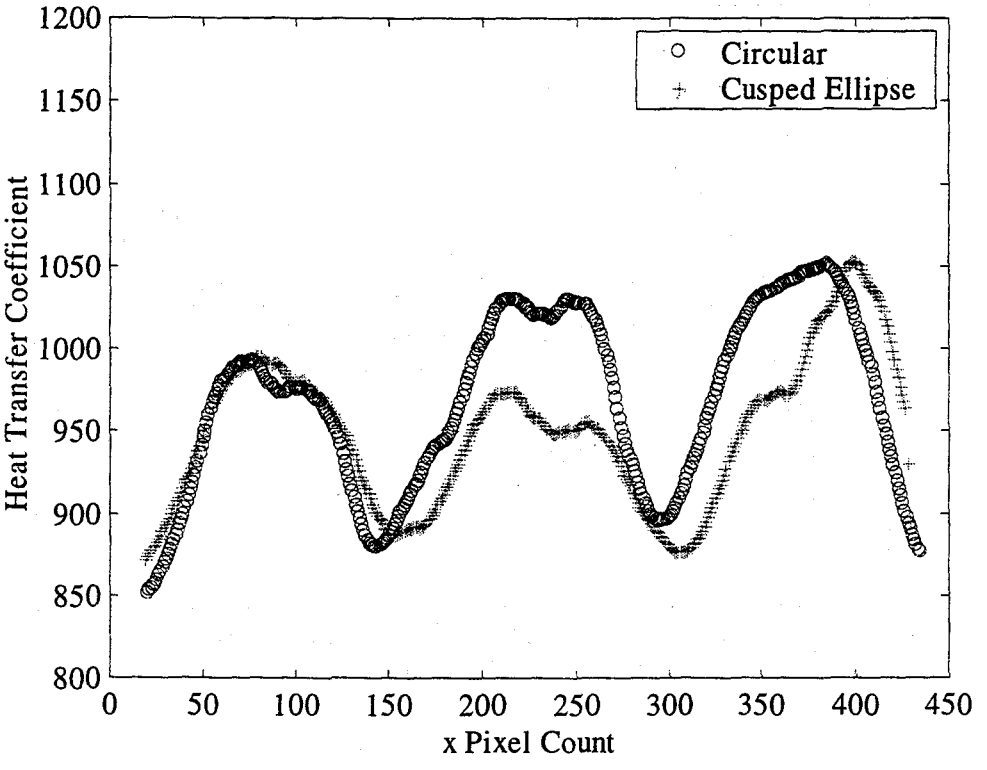

Figure C-23. Center Cross Section (x slice), Flow Rate 0.0049 m^3/s, $H/D_h = 3$

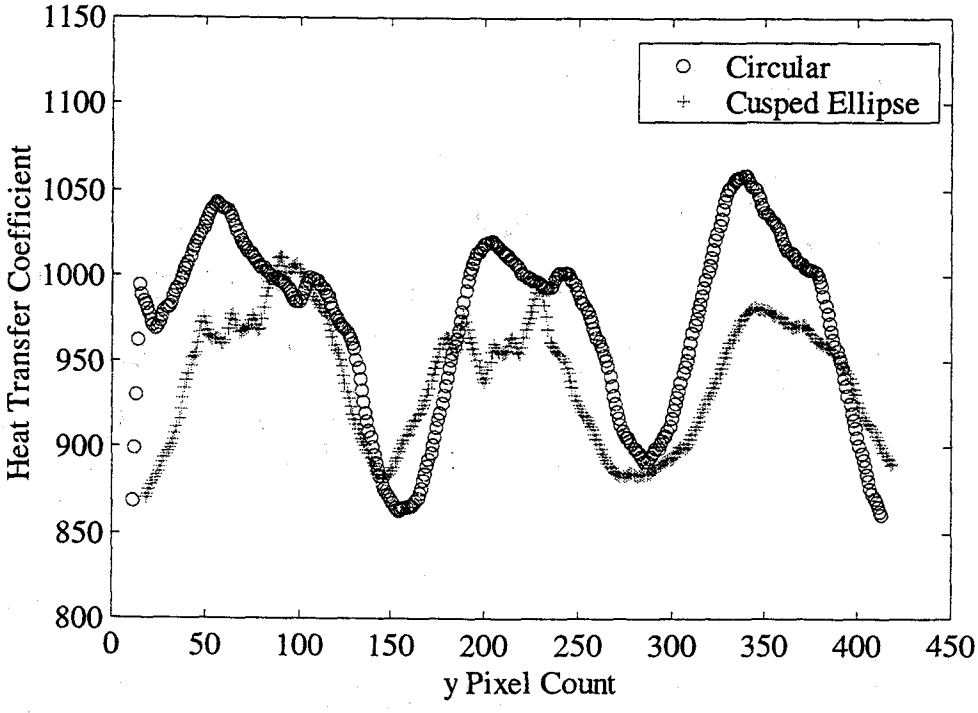

Figure C-24. Center Cross Section (y slice), Flow Rate 0.0049 m^3/s, $H/D_h = 3$

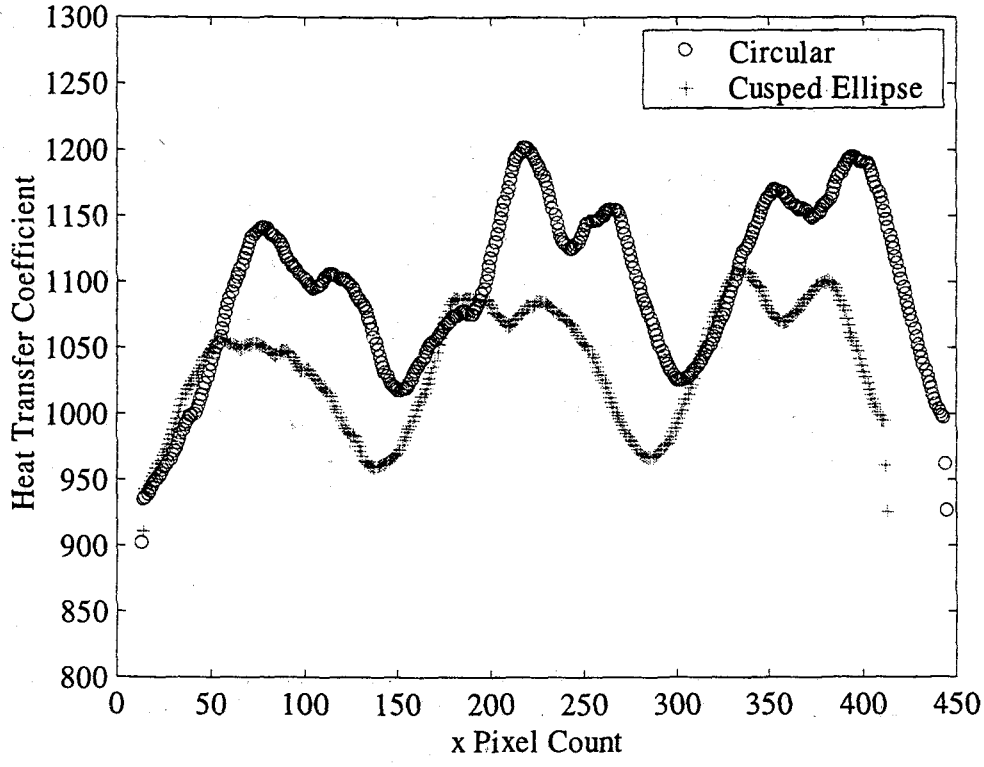

Figure C-25. Center Cross Section (x slice), Flow Rate 0.0055 m^3/s, $H/D_h = 3$

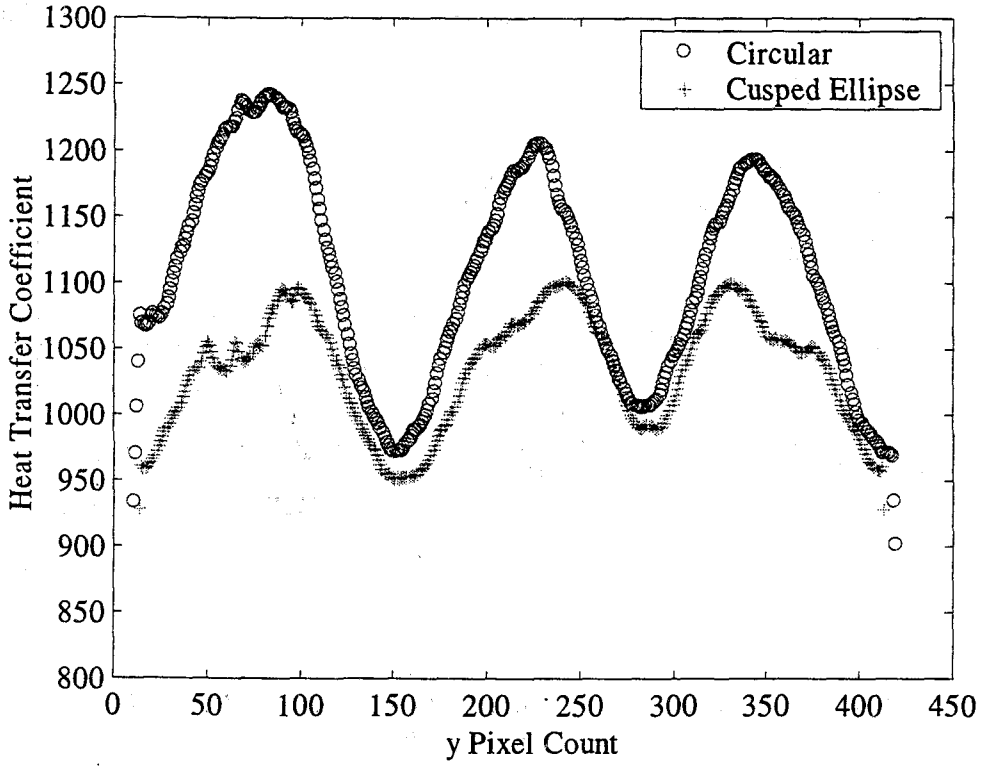

Figure C-26. Center Cross Section (y slice), Flow Rate 0.0055 m^3/s, $H/D_h = 3$

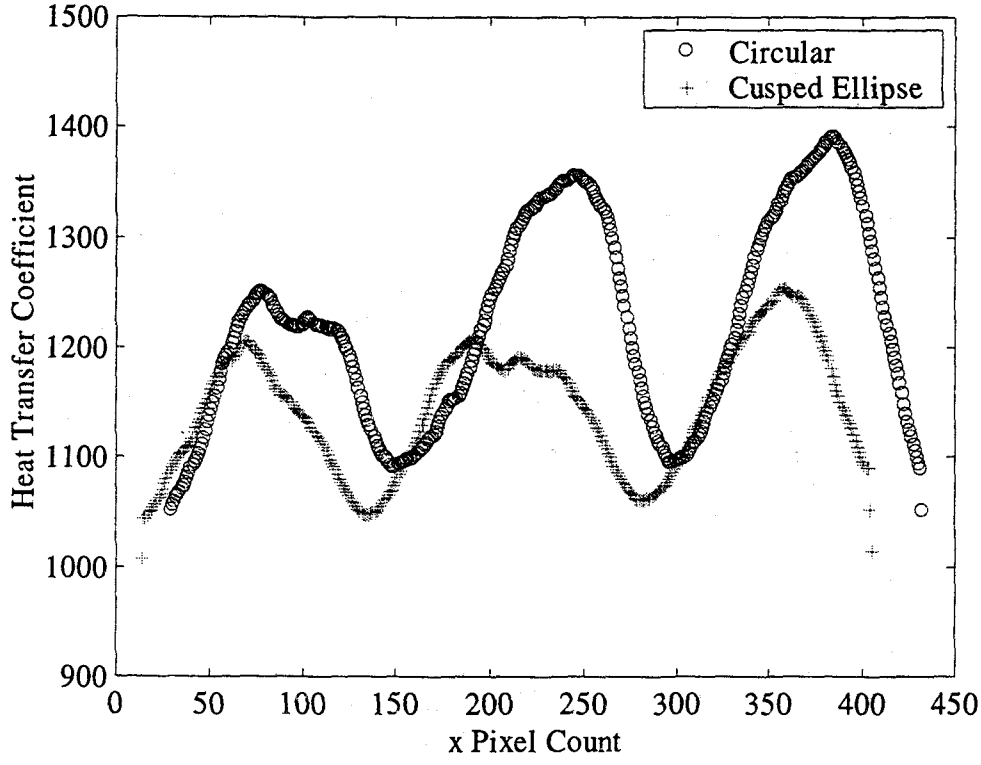

Figure C-27. Center Cross Section (x slice), Flow Rate 0.0060 m^3/s, $H/D_h = 3$

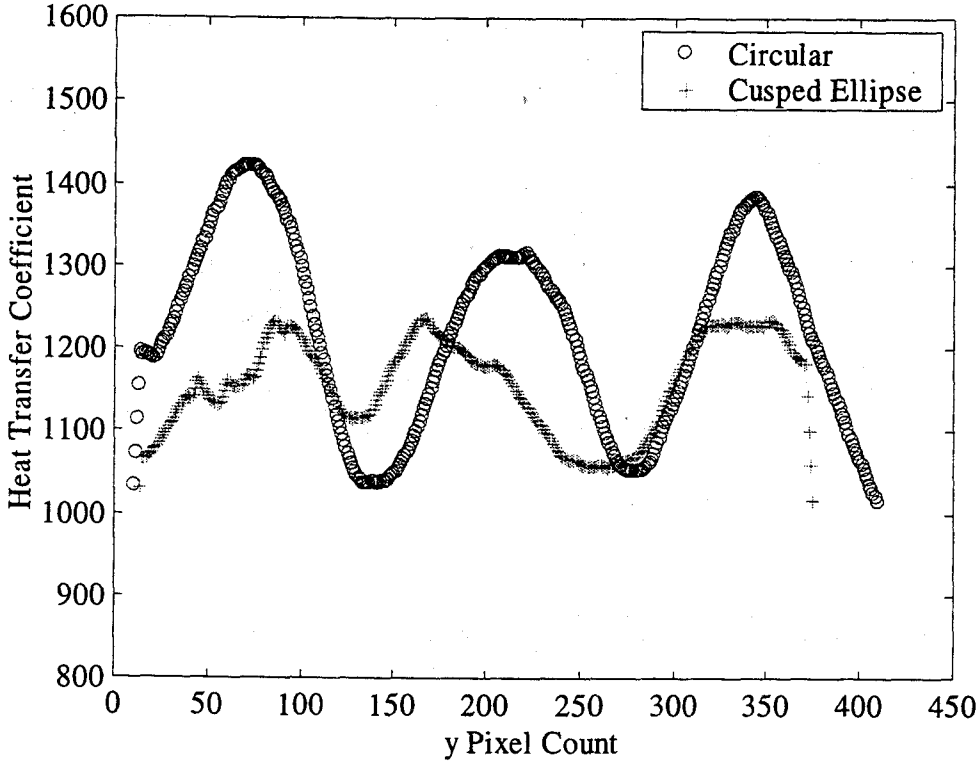

Figure C-28. Center Cross Section (y slice), Flow Rate 0.0060 m^3/s, $H/D_h = 3$

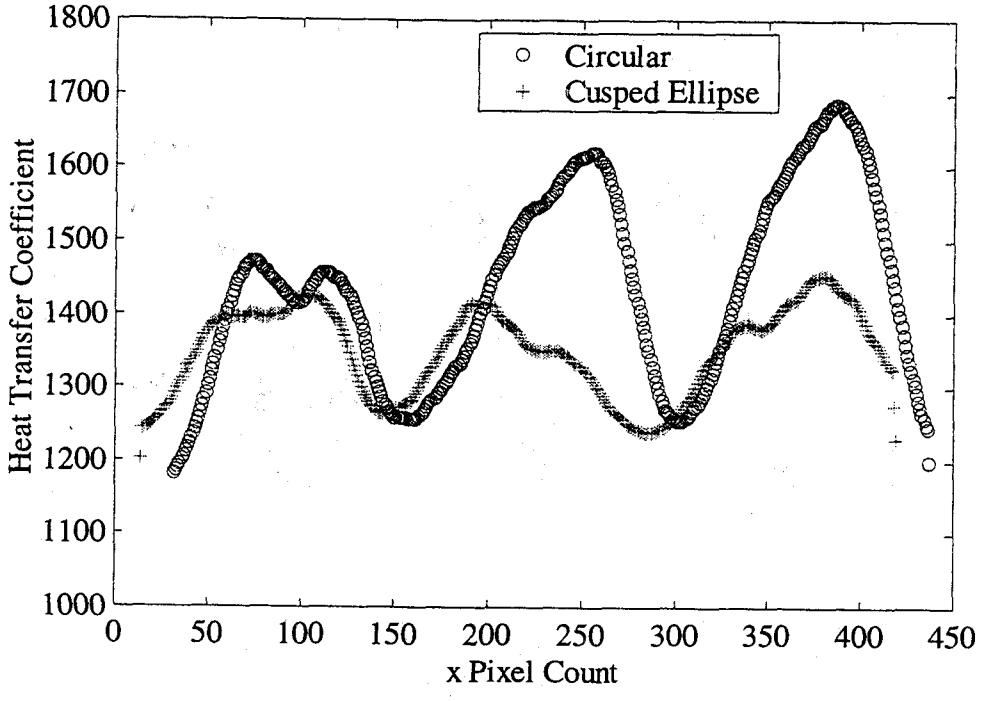

Figure C-29. Center Cross Section (x slice), Flow Rate 0.0072 m^3/s, $H/D_h = 3$

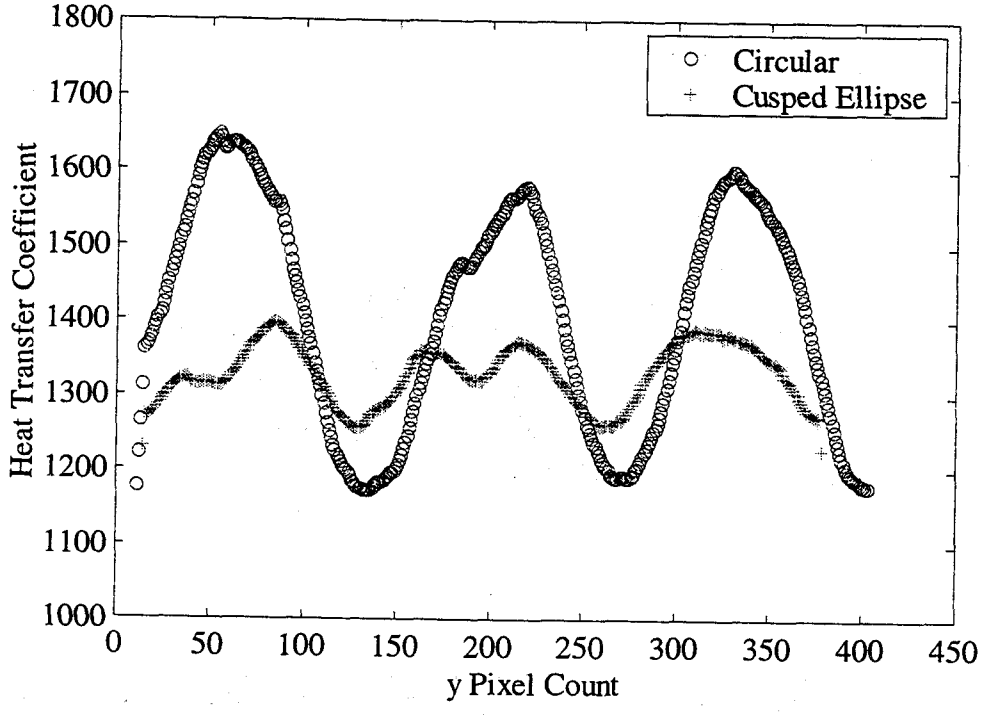

Figure C-30. Center Cross Section (y slice), Flow Rate 0.0072 m^3/s, $H/D_h = 3$

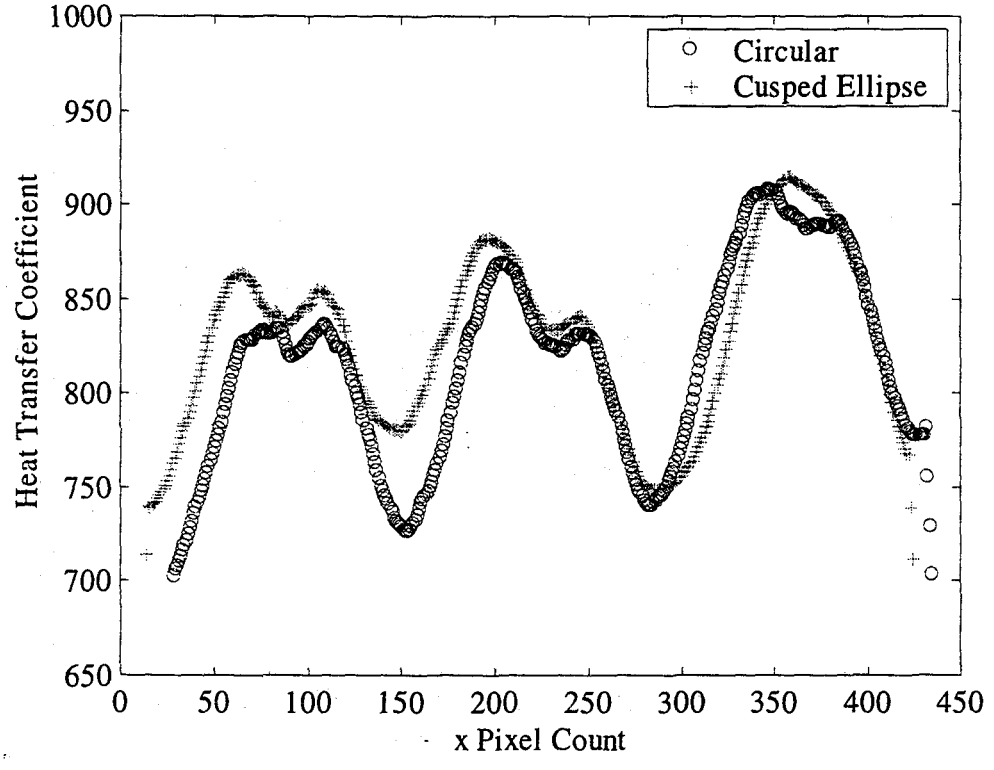

Figure C-31. Center Cross Section (x slice), Flow Rate 0.0039 m^3/s, $H/D_h = 4$

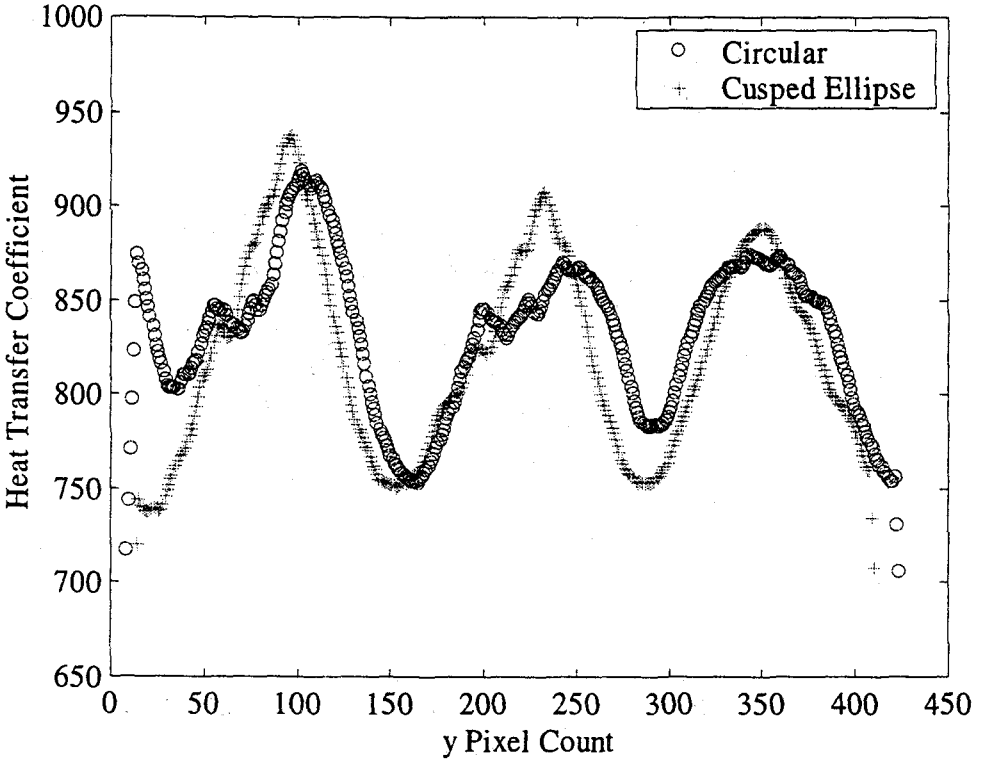

Figure C-32. Center Cross Section (y slice), Flow Rate 0.0039 m^3/s, $H/D_h = 4$

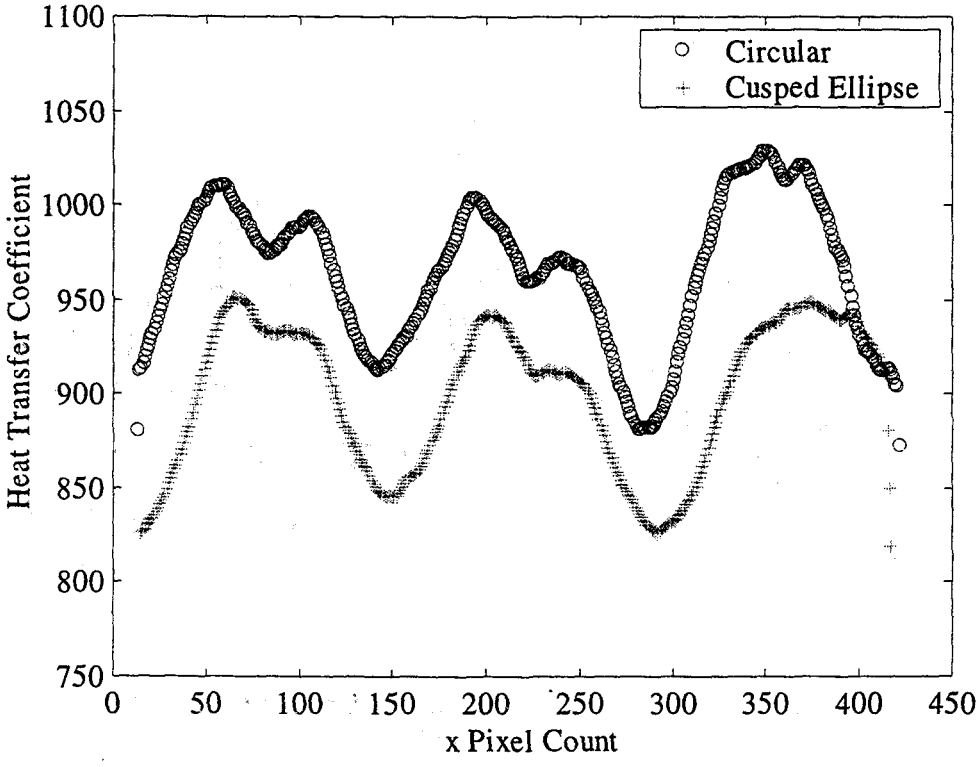

Figure C-33. Center Cross Section (x slice), Flow Rate 0.0049 m^3/s, $H/D_h = 4$

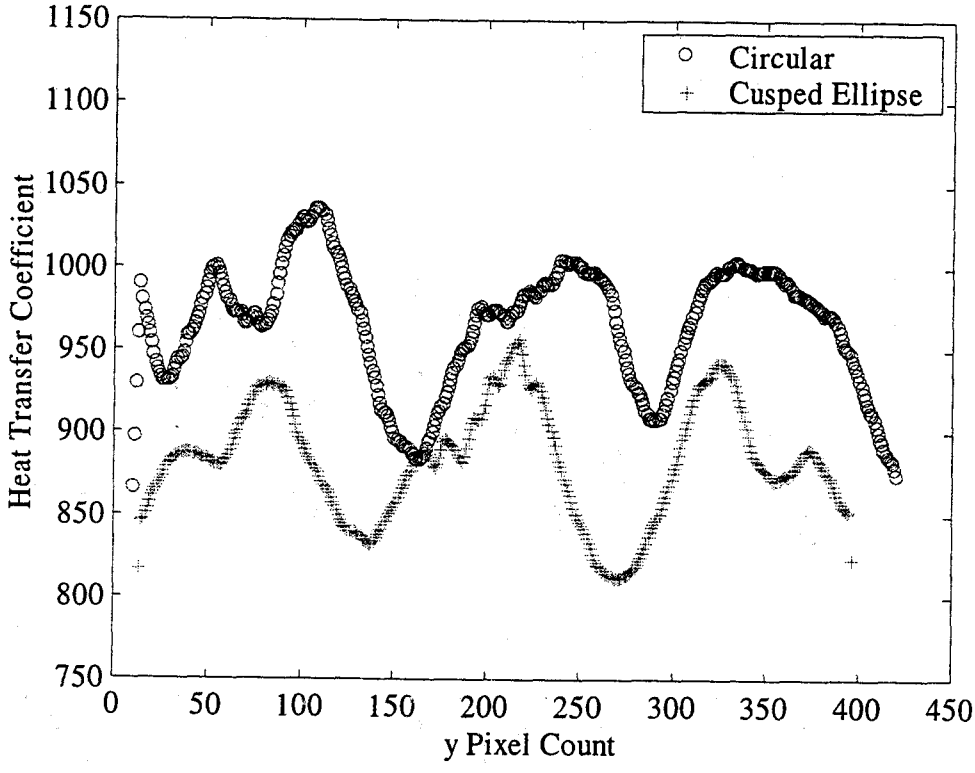

Figure C-34. Center Cross Section (y slice), Flow Rate 0.0049 m^3/s, $H/D_h = 4$

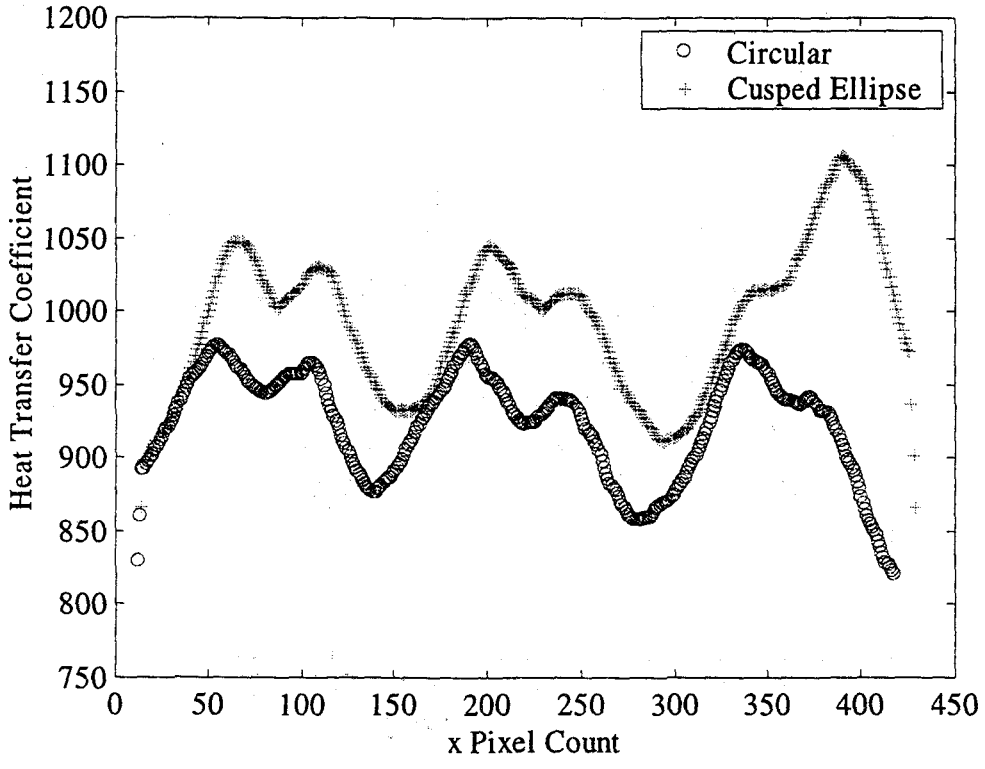

Figure C-35. Center Cross Section (x slice), Flow Rate 0.0055 m^3/s, $H/D_h = 4$

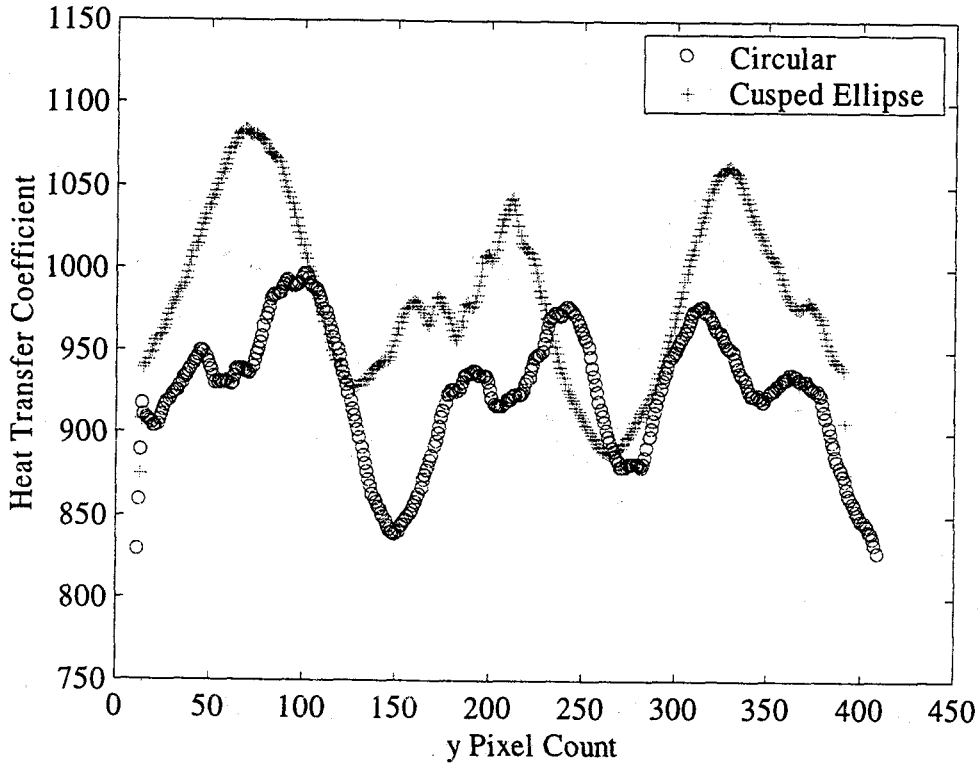

Figure C-36. Center Cross Section (y slice), Flow Rate 0.0055 m^3/s, $H/D_h = 4$

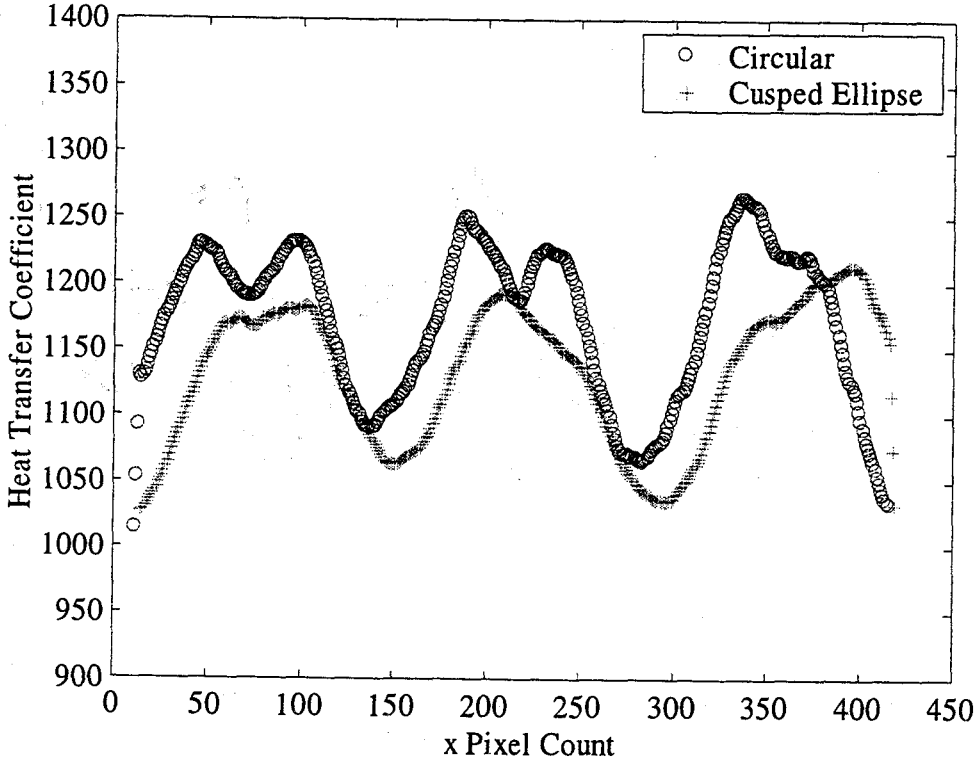

Figure C-37. Center Cross Section (x slice), Flow Rate 0.0060 m^3/s, $H/D_h = 4$

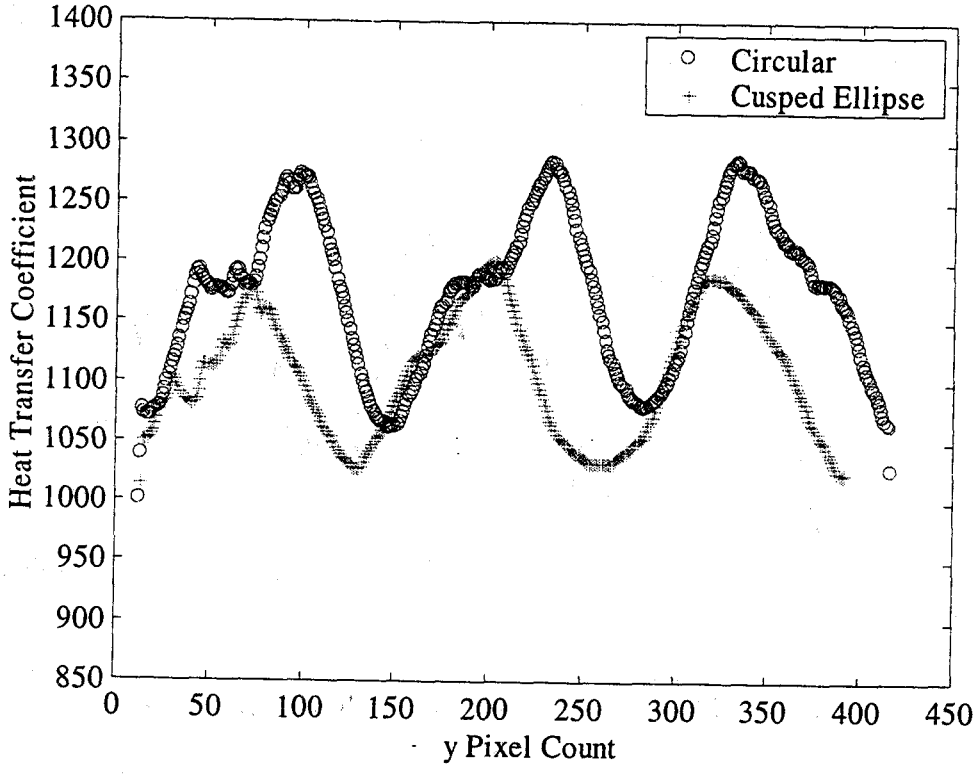

Figure C-38. Center Cross Section (y slice), Flow Rate 0.0060 m^3/s, $H/D_h = 4$

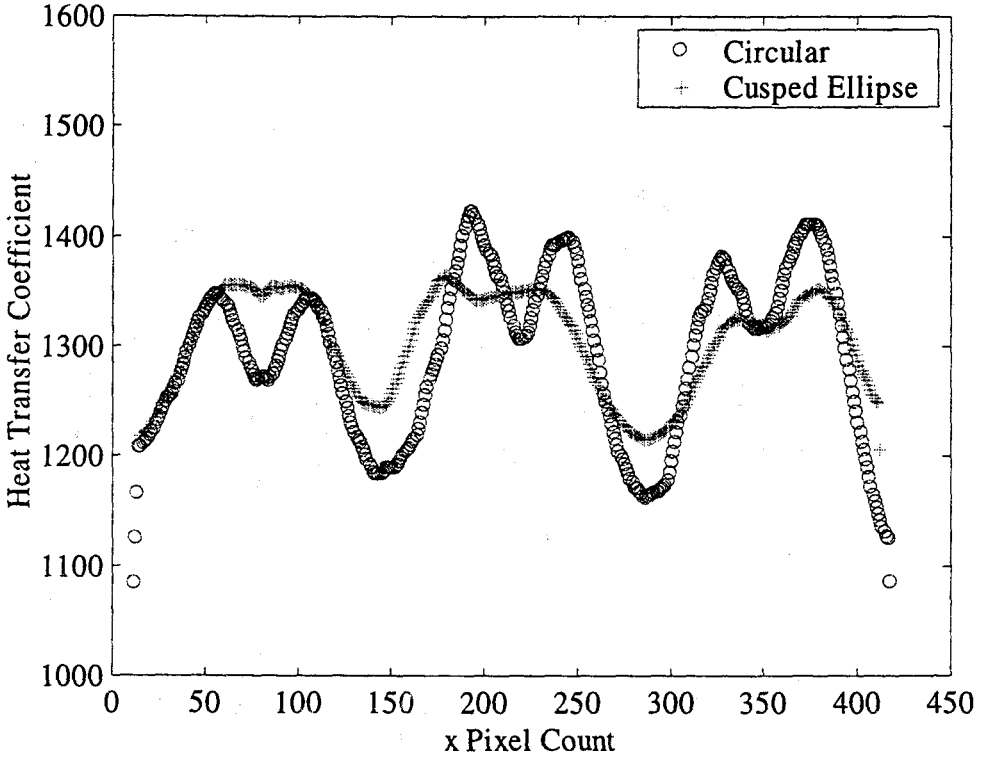

Figure C-39. Center Cross Section (x slice), Flow Rate 0.0072 m^3/s, $H/D_h = 4$

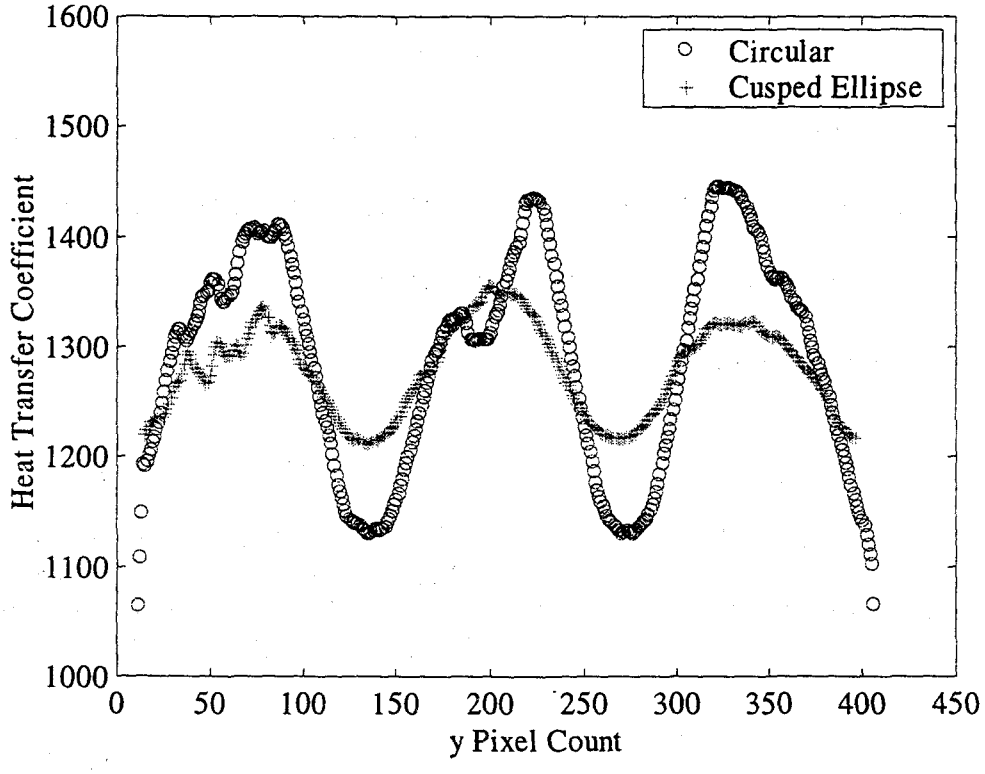

Figure C-40. Center Cross Section (y slice), Flow Rate 0.0072 m^3/s, $H/D_h = 4$

APPENDIX D

MATLAB PROGRAMS

This appendix comprises of the computer code for MATLAB used for the data reduction in the uniform heat flux surface boundary condition.

Program I

This program picks the hue value from the HSV values, then converts the hue values into the temperature based on the liquid crystal calibration. Later in the program, the average heat transfer coefficient and average Nusselt number are calculated from the matrix of temperatures. Finally, the surface plot is conducted.

```
%Based on the liquid crystal calibration

hue = [0.2831 0.3185 0.3651 0.3890 0.4060 0.4228 0.4707 0.4965 0.5275 0.5360
       0.5467  0.5575 0.5713 0.5802 0.5936];
thue = [26.010 26.227 26.477 26.770 27.013 27.240 27.503 27.740 28.123 28.190
        28.277 28.483 28.763 29.007 29.223];

A=4.0803e-3; % Area of the foil
q=10.161; %varies
Tjet=23.6; %varies

rgb=imread('circular_1_8.tif');
hsv=rgb2hsv(rgb);
h=hsv(:,:,1); %pick hue value from HSV

%Filter the hue values

for n=500
  hew=medfilt2(h,[3 3]);
end

[r,c]=size(hew); %hew is a matrix of hue values from the image
```

```
%interpolate temperature from the image using cubic spline
T=interp1(hue,thue,hew(:),'spline');
%hew(:) means all the elements of hew, reguarded as a single column
T=reshape(T,r,c);

for i=1:1:r
 for j=1:1:c
   if T(i,j)<26.010;
     T(i,j)=26.010;
   elseif T(i,j)>29.223;
     T(i,j)=29.223;
   end
   end
  end

%Find average heat transfer coefficient from each pixel

  H= q./(A*(T-Tjet));
  [row,col]=size(H);


  %Find the average heat transfer coefficient by
  %averaging local h

  COUNT=0;
  SUM=0;
  for e=1:row
    for f=1:col
        SUM=SUM+H(e,f);
        COUNT=COUNT+1;

    end
  end
  S=SUM;
  C=COUNT;
  Ave=SUM/COUNT %The average heat transfer coefficient

  %Find the Nusselt number from the summation of each pixel

  Nu=H*0.048694; %Local Nu

  count = 0;
  sum = 0;
  for p = 1:row
```

```
    for q = 1:col
      sum = sum + Nu(p,q);
      count = count + 1;
    end
  end

  Nusselt = sum/count %average Nusselt number

%Find the average surface temperature
  %And average Nusselt number from Ts(ave)

  [ro,co]=size(T);
  number = 0;
  Ttot = 0;
  for c = 1:ro
    for d = 1:co
      Ttot=Ttot+T(c,d);
      number = number+1;
    end
  end

  Tstot = Ttot;
  N = number;
  Ts = Tstot/N
  Havg=q/(A*(Ts-Tjet));
  Nuavg = Havg*0.048694;

%Filter to help smooth out abnormal peaks in the data

    J = Nu;
    for num=50
      h = fspecial('average',20);
      I = filter2(h,J);
    end

%Find average Nusselt number after filtering

    number = 0;
    summation = 0;
    [rw,cl]=size(I);
    for i = 1:rw
      for j = 1:cl
        summation = summation+I(i,j);
        number = number + 1;
```

```
  end
end

Nuave = summation/number %Nusselt number after filtering

%Surface plot

[horiz,ver]=size(I)
x=1:horiz;
y=1:ver;

[X,Y]=meshgrid(x,y);
mesh(I);
xlabel('x pixel count');
ylabel('y pixel count');
zlabel('Nusselt number');
title('Re = 7005, Circular,H/D = 1');
```

Program II

This program determines and compares the local values of heat transfer coefficients for both geometries by taking a slice through the center of the jets. The program can be set up to take a slice either streamwise direction or spanwise direction.

```
hue = [0.2831 0.3185 0.3651 0.3890 0.4060 0.4228 0.4707 0.4965 0.5275 0.5360
       0.5467 0.5575 0.5713 0.5802 0.5936];
thue = [26.010 26.227 26.477 26.770 27.013 27.240 27.503 27.740 28.123 28.190
        28.277 28.483 28.763 29.007 29.223];

Subscript 1 is for circular jets
%Subscript 2 is for cusped ellipse jets

%A=4.0803e-3; %Area of the foil
q1 = 16.357;
q2 = 16.9182;
Tjet1 = 23.3;
Tjet2 = 23.5;

rgb1 = imread('circular_3_12.tif');
rgb2 = imread('peanut_3_12.tif');
hsv1 = rgb2hsv(rgb1);
hsv2 = rgb2hsv(rgb2);
h1 = hsv1(:,:,1);%Pick hue value from HSV
h2 = hsv2(:,:,1);

%Filter the hue values

for n1 = 500
  hew1 = medfilt2(h1,[3 3]);
end

for n2 = 500
  hew2 = medfilt2(h2,[3 3]);
end

[r1,c1] = size(hew1);
[r2,c2] = size(hew2);
```

```
T1 = interp1(hue,thue,hew1(:),'spline');
T2 = interp1(hue,thue,hew2(:),'spline');
T1 = reshape(T1,r1,c1);
T2 = reshape(T2,r2,c2);

for i1 = 1:1:r1
  for j1 = 1:1:c1
    if T1(i1,j1)<26.010;
      T1(i1,j1)=26.010;
    elseif T1(i1,j1)>29.223;
      T1(i1,j1)=29.223;
    end
  end
end

for i2 = 1:1:r2
  for j2 = 1:1:c2
    if T2(i2,j2)<26.010;
      T2(i2,j2)=26.010;
    elseif T2(i2,j2)>29.223;
      T2(i2,j2)=29.223;
    end
  end
end

%Find local heat transfer coefficient of each pixel

H1 = q1./(A*(T1-Tjet1));
[row1,col1] = size(H1);
H2 = q2./(A*(T2-Tjet2));
[row2,col2] = size(H2);

%Filter to help smooth out abnormal peaks

J1 = H1;
for num1 = 500
  U1 = fspecial('average',30);
  V1 = filter2(U1,J1);
end
[rw1,col1] = size(V1);
for a1 = 1:rw1
  for b1 = 1:col1
    if V1(a1,b1)<1000;
```

```
      V1(a1,b1)=0;
    end
  end
end


J2 = H2;
for num2 = 500
  U2 = fspecial('average',30);
  V2 = filter2(U2,J2);
end
[rw2,col2] = size(V2);
for a2 = 1:rw2
  for b2 = 1:col2
    if U2(a2,b2)<1000;
      V2(a2,b2)=0;
    end
  end
end


%Slice program for X and Y cross sections for both geometries

[horiz1,ver1] = size(V1);
[horiz2,ver2] = size(V2);

x1 = 1:horiz1;
y1 = 1:ver1;
x2 = 1:horiz2;
y2 = 1:ver2;
K1 = V1(:,75,:);
K2 = V2(:,75,:);
axis off;
%axes('XLim',[0,500],'YLim',[0,150]);

plot(x1,K1,'bo',x2,K2,'r+');
legend('Circular','Cusped Ellipse');
set(gca,'Box','on');
ylabel('Heat Transfer Coefficient');
xlabel('y Pixel Count');
title('Flow rate 0.0072 m^3/sec, Re(circular) = 10195, Re(Peanut) = 8981, H/Dh =
2');
```

Program III

This program determines the normalized root square value, which is the relative intensity of the fluctuation of local values from the average for each test. The RMS is used to make a judgement on the uniformity of the heat transfer for each geometry.

```
hue = [0.2831 0.3185 0.3651 0.3890 0.4060 0.4228 0.4707 0.4965 0.5275 0.5360
       0.5467 0.5575 0.5713 0.5802 0.5936];
thue = [26.010 26.227 26.477 26.770 27.013 27.240 27.503 27.740 28.123 28.190
        28.277 28.483 28.763 29.007 29.223];

A=3.136e-3;
q = 23.3376;
Tjet = 22.8;

rgb = imread('peanut_4_14.tif');
hsv = rgb2hsv(rgb);
h = hsv(:,:,1);

%Filter the hue values

for n = 50
  hew = medfilt2(h,[3 3]);
end

[r,c] = size(hew);

T = interp1(hue,thue,hew(:),'spline');
T = reshape(T,r,c);

for i = 1:1:r
  for j = 1:1:c
    if T(i,j)<26.010;
      T(i,j)=26.010;
    elseif T(i,j)>29.223;
      T(i,j)=29.223;
    end
  end
end
```

```
%Find local heat transfer coefficient of each pixel

H = q./(A*(T-Tjet));
[row,col] = size(H)

I = H;
for no = 50
  a = fspecial('average',20);
  b = filter2(a,I);
end

%Loop to find average heat transfer coefficient

count = 0;
total = 0;
for m = 1:row
  for n = 1:col
    if K(m,n)~=0
      total = total+K(m,n);
      count = count+1;
    end
  end
end

average = total/count %Average Heat Transfer Coefficient

%Loop to calculate rms value

num = 0;
sum = 0;
for m = 1:row
  for n = 1:col
    if K(m,n)~=0
      sum = sum + (K(m,n)-average)^2;
      num = num + 1;
    end
  end
end
avesqr = sum/num;
rms = sqrt(avesqr)/average %Normalized Root Mean Square
```